

Augmented Topological Level-Set for Large-Scale Thermo-Elastic Topology Optimization

By

Shiguang Deng

A dissertation submitted in partial fulfillment of
the requirements for the degree of

Doctor of Philosophy
(Mechanical Engineering)

at the

UNIVERSITY OF WISCONSIN - MADISON

2016

Date of final oral examination: 5/18/2016

The dissertation is approved by the following members of the final oral committee:

Krishnan Suresh, Professor, Mechanical engineering
Gregory F. Nellis, Professor, Mechanical Engineering
Xiaoping Qian, Associate professor, Mechanical engineering
Matthew S. Allen, Associate professor, Engineering physics
Eftychios Sifakis, Assistant professor, Computer science

ABSTRACT

This thesis focuses on thermo-elastic topology optimization of structures subject to both mechanical and thermal loads. Such problems are of significant importance, for example, in aircraft industry where aerodynamic forces and thermal-gradients are common.

A popular topology optimization method for solving such problems is Solid Isotropic Material with Penalization (SIMP) where pseudo-densities are assigned to each finite element. With values varying between 0 and 1, the pseudo-densities serve as independent variables in the optimization process. Although popular and easy to implement, SIMP exhibits the deficiency of zero-slope at zero-density when solving thermo-elastic problems. This deficiency leads to convergence issues. To overcome such defects, another method, called Rational Approximation of Material Properties (RAMP), was proposed based on SIMP. However, since both methods fundamentally rely on parameterization of material properties as functions of pseudo-densities, they both suffer from ill-conditioned stiffness matrices, poorly defined boundary conditions and stress singularities.

A topological sensitivity based level-set method, called Pareto, is studied instead in this thesis. Pareto does not suffer from the above deficiencies, i.e., the stiffness matrices are well-conditioned, the boundary is well-defined and stress singularities do not arise. However, Pareto has only been demonstrated for pure elasticity, and constraints have not been addressed in a systematic way.

Therefore, the achievement of this research is extending Pareto from pure elasticity to thermo-elasticity, and addressing a variety of constraints that may arise in such problems.

Unlike in pure elasticity, for thermo-elastic problems, the displacements and stresses are computed after taking into account the additional thermal loads. The fundamental notion of topological sensitivity (exploited in Pareto) must therefore be extended to consider both elastic and thermal scenarios. The derivations of topological sensitivities with respect to a variety of mechanical properties, for example, compliance, stress, modal and buckling, are one of the key theoretical accomplishments in this thesis.

To address constraints, an augmented Lagrangian topological level-set method is proposed. By employing classic augmented Lagrangian algorithm, the proposed method is capable of solving topological optimization problems with multiple constraints. Specifically, the augmented Lagrangian algorithm and the concept of topological sensitivity are combined with level-set approach to absorb various constraints into a single objective. The augmented objective is then iteratively minimized by the classic Pareto method. In the process, questions of numerical efficiency and robustness are addressed.

Finally, the thermo-elastic topology optimization formulation is integrated with the proposed augmented Lagrangian level-set method to solve multi-constrained thermo-elastic design problems in an efficient and correct way. While most of topology optimization algorithms are tested on simple 2D benchmark examples, the developed method is tested and applied on a series of 3D large-scale industrial models, rendering the proposed algorithm efficient and robust for a variety of real world applications.

ACKNOWLEDGEMENTS

Finally, after 4 years of intensive research, finishing this thesis is the final touch on my graduate study. Writing this document has a significant impact on me. It gives me not only a feedback on how much knowledge and research experience I have gained, but also a precious opportunity to pause and reflect on the people who have encouraged and supported me throughout the years.

I owe my deepest gratitude to my advisor Prof. Krishnan Suresh. I was extremely fortunate to be selected by Prof. Suresh to join ERSL 4 years ago. It was impossible for me to come a long way from the beginning to the final defense today without his persistent guidance and endless support. His extensive advising experience mentored me to approach and solve a research problem in a systematic way. His industry management experience taught me the importance of efficient communication in the form of both presentation and publication. His entrepreneurship showed me the necessity of always doing meaningful researches that push forward industry development. His broad knowledge in solid mechanics, finite element analysis, topology optimization, cloud computing, high-performance computing and additive manufacturing gave me a great example to appreciate self-learning and continuous study. Prof. Suresh himself unconsciously set me a high standard model that I will always follow in my future career.

I would also like to thank Prof. Gregory Nellis and Prof. Natalie Rudolph. In the Oak Ridge National Laboratory funded project, their expertise in fluid mechanics, energy system and additive manufacturing expanded my knowledge and let me appreciate the significant impact of topology optimization for mechanical designs in real industry applications. Besides, I also appreciate the trust and freedom they gave during the project.

I would like to thank Prof. Xiaoping Qian on his constructive suggestions for not only my research topics but also my future career path. Easy-going, patient, hard-working and knowledgeable, Prof. Qian is always the example I hope to follow as a Chinese international student. I extend my thanks to my other two committee members, Prof. Matt Allen and Prof. Eftychios Sifakis for their valuable suggestions and comments over the course of this program.

Also, I want to express appreciations to my M.S. program advisor Prof. Mark Garnich, Prof. Sukky Jun and Prof. Paul Dellenback in University of Wyoming. Without their guidance and support, I would not have the opportunity to continue the graduate study here in UW-Madison.

I would like to thank my colleagues in ERSI (Praveen Yadav, Amir Mirzhendehtdel, Chaman Verma, Alireza Taheri, Anirudh Krishnakumar, Victor Cavalcanti, Anirban Niyogi, Xiang Bian, Alex Buehler, Tej Kumar and Aaditya Cs), in CDML (Jing Li, Songtao Xia, Xilu Wang and Cunfu wang), in SAL (Xingchen Liu, Goldy Kumar, Randi Wang, Yaqi Zhang and Vaidyanathan Thiagarajan) and all my other friends in Chinese Crazy Legs soccer team. Without the enjoyable discussions and activities with them, my graduate school life would definitely be more stressful.

Last but not the least, I want to thank my girlfriend Sining Lian. Without her continuous support, encouragement and belief, I would not feel so much happiness and confidence. The most importantly, I want to thank the unconditional trust and support from my mother Shufang Wang and my father Mingjie Deng. Their unwavering love is the power that helped me walk through every difficulty in my life.

Table of Contents

ABSTRACT	ii
ACKNOWLEDGEMENTS	iv
LIST OF FIGURES	xi
LIST OF TABLES	xvi
1. INTRODUCTION TO THERMO-ELASTIC STRUCTURAL DESIGN PROBLEMS ...	1
1.1 Structure Design in Thermal Environment	1
1.2 Literature Review of Topology Optimization.....	2
1.2.1 Review of thermo-elastic topology optimization	4
1.2.2 Review of multi-load multi-constrained topology optimization	6
1.3 Thesis Overview.....	10
2. INTRODUCTION TO TOPOLOGY OPTIMIZATION	14
2.1 A Pure Elastic Unconstrained Topology Optimization.....	14
2.2 A Popular Topology Optimization Method: SIMP.....	16
2.2.1 SIMP Formulation	16
2.2.2 Limitations and Disadvantages.....	17
3. INTRODUCTION TO TOPOLOGICAL SENSITIVITY BASED LEVEL-SET METHOD	19
3.1 Topological Sensitivity	19
3.2 Topological Level-set.....	21

3.3 PareTO Method.....	23
4. THERMO-ELASTIC TOPOLOGICAL LEVEL-SET METHOD	25
4.1 Formulation of Thermal Elastic FEA.....	25
4.2 Formulation of Thermal Elastic Topology Optimization.....	28
4.2.1 Compliance Minimization	28
4.2.2 Stress-Minimization.....	29
4.2.3 Analytical Topological Sensitivity Fields	30
4.3 Algorithm of Thermo-Elastic Topological Level-Set	31
4.4 Numerical Experiments.....	32
4.4.1 Bi-clamped beam with a point load.....	33
4.4.2 Bi-clamped beam with distributed loads	34
4.4.3 Clamped beam with tip load.....	36
5. AUGMENTED TOPOLOGICAL LEVEL-SET METHOD	38
5.1 Multi-Constrained Topology Optimization.....	38
5.2 Augmented Lagrangian Method	40
5.3 Augmented Topological Level-Set	42
5.4 Illustrative Examples.....	44
5.5 Algorithm of Augmented Topological Level-Set	47
5.6 Numerical Experiments.....	49
5.6.1 Cantilever Beam: Displacement Constraints	50

5.6.2 Cantilever Beam: Multi-load	51
5.6.3 L-bracket: Displacement & Stress Constraints.....	52
5.6.4 L-bracket: Multi-load, Multi-Constraint.....	53
5.6.5 Mitchell Bridge: Multi-load, Multi-Constraint.....	55
6. LARGE-SCALE CONSTRAINED TOPOLOGY OPTIMIZATION	58
6.1 Literature Review of Large-scale Topology Optimization	58
6.2 Formulation of Large-Scale Topology Optimization.....	60
6.2.2 Assembly-Free FEA	60
6.2.2 Element Congruency and Mesh Voxelization	61
6.2.3 Deflated Method.....	62
6.2.4 PareTo in 3D.....	63
6.3 Formulation of Constraints.....	63
6.3.1 Hard and Soft Constraints.....	63
6.3.2 Casting Constraints.....	64
6.4 Algorithm of Large-Scale Constrained Topology Optimization.....	65
6.5 Numerical Examples	67
6.5.1 L-bracket with Tip Load.....	68
6.5.2 Plate with Pressure Load	70
6.5.3 Case Study: Flange	73
6.5.4 Case Study: Bicycle Frame.....	76

6.5.5 Case Study: Bicycle crank	79
7. LARGE-SCALE THERMO-ELASTIC MULTI-CONSTRAINED TOPOLOGY OPTIMIZATION.....	83
7.1 Approximate Thermo-Elastic Topological Sensitivity	85
7.1.1 Spatially Uniform Increase in Temperature	85
7.1.2 Non-Uniform Change in Temperature	89
7.1.3 Sensitivity of Stiffness Matrices.....	92
7.2 Algorithm of Large-Scale Thermo-Elastic Constrained Topology Optimization.....	92
7.3 Numerical Experiments.....	94
7.3.1 Benchmark: Bi-clamped beam with a point load	95
7.3.2 Benchmark: Distributed load Bi-clamped beam	100
7.3.3 Case study: Flange.....	104
7.3.4 Case study: Exhaust system.....	106
8 APPLICATION: BUCKLING TOPOLOGY OPTIMIZATION	110
8.1 Introduction to Thermo-Elastic Buckling	110
8.2 Literature Review of Buckling Constrained Topology Optimization.....	111
8.2 Buckling Sensitivity Analysis	114
8.3.1 Direct method	116
8.3.2 Adjoint method.....	119
8.3.3 Discrete element sensitivity approximation	121

8.4 Algorithm of Constrained Thermo-Elastic Buckling Topology Optimization	122
8.5 Numerical Experiments.....	123
8.5.1 Benchmark example	124
8.5.2 Industrial application: airplane wing rib structure.....	130
9. CONCLUSION AND FUTURE WORK	138
9.1 Conclusion.....	138
9.2 Future Work	139
9.2.1 Micro-Scale Topology Optimization.....	139
9.2.2 Nonlinear Topology Optimization.....	140
9.2.3 Non-Deterministic Topology Optimization.....	141
9.2.4 Topology Optimization in Additive Manufacturing.....	141
REFERENCE.....	143

LIST OF FIGURES

Figure 1: Conceptual engine exhaust-washed structure [1].....	2
Figure 2: A single-load structural problem.....	14
Figure 3: Optimal topology for a specific instance of Equation (2) over the structure in Figure 2.	15
Figure 4: Finite element mesh and progression in SIMP.....	17
Figure 5: A topological change.....	19
Figure 6: Topological sensitivity field.....	21
Figure 7: Topological sensitivity field as a level-set.....	23
Figure 8: Fixed point iteration involving three quantities	23
Figure 9: Pareto-optimal topologies.....	24
Figure 10: A thermo-elastic problem.....	25
Figure 11: An overview of the algorithm.....	32
Figure 12: The bi-clamped structure with point-load.....	33
Figure 13: The bi-clamped structure with a distributed load.....	35
Figure 14: The cantilever beam problem.....	36
Figure 15: A single-load structural problem.....	39
Figure 16: A multi-load structural problem.....	40
Figure 17: A single-load problem with displacement constraint.....	45
Figure 18: A multi-load problem with displacement constraint.....	47
Figure 19: Proposed algorithm.....	49
Figure 20: A single load cantilever beam problem with a displacement constraint	50
Figure 21: A multi-load cantilever beam problem.....	52

Figure 22: A single-load L-bracket problem with global stress constraint.....	53
Figure 23: A multi-load L-bracket problem.....	54
Figure 24: A multi-load Mitchell bridge problem.	55
Figure 25: Bearing support CAD model and its voxelization mesh.	62
Figure 26: The Pareto-optimal curve and optimal topologies for a 3D structural problem.....	63
Figure 27: A multi-load Mitchell bridge problem.	67
Figure 28: L-bracket cross-section.....	68
Figure 29: Final topologies which are subject to dominant constraints of compliance (left) and Von Mises stress (right).....	69
Figure 30: Computational cost for scenario-1 in Table 10.	70
Figure 31: Thick plate dimensions with pressure loading.	70
Figure 32: Final topologies for compliance dominated (top) stress dominated (left) and buckling-dominated (right).	71
Figure 33: Iteration history of volume decrement for scenario-2 in Table 15.....	72
Figure 34: Constraint iteration history for scenario-2 in Table 15.	73
Figure 35: Flange structure and dimensions.	74
Figure 36: Final topologies for compliance dominated (top-left) stress dominated (top-right), and stress and Eigen-value dominated (bottom).....	75
Figure 37: Volume decrement history for scenario-3 in Table 16.....	75
Figure 38: Iteration history of constraints for scenario-3 in Table 16.	76
Figure 39: Design space of bike frame: front view (1st), top view (2nd) and side view (3rd).....	77
Figure 40: The bike frame subject to multiple loads.	78
Figure 41: Proposed design for a bike frame.	78

Figure 42: Dimensions of the crank arm.....	79
Figure 43: The crank arm subject to multi-load during a pedaling cycle [139].	80
Figure 44: Final design of crank arm.....	80
Figure 45: Final design of crank arm with casting constraint.....	81
Figure 46: The structurally loaded flange (left) is also subject to a thermal load; the resulting stress plot (right).	84
Figure 47: Restrained exhaust duct subject to temperature gradient (left) and resulting stress (right).	84
Figure 48: An overview of the algorithm.	94
Figure 49: The bi-clamped structure with a central point load.	96
Figure 50: Optimized topology for compliance-constrained topology optimization.....	97
Figure 51: Iteration history of compliance for problem in Equation (123).	97
Figure 52: The final topologies for different temperature variations for problem in Equation (123).....	98
Figure 53: The optimized topology for stress-constrained topology optimization.....	99
Figure 54: The final topologies for different temperature variations.	100
Figure 55: The bi-clamped structure with a distributed load.....	101
Figure 56: Final topology and stress distribution when the structure in Figure 13 is subject to uniform temperature rise.....	101
Figure 57: Final topology and stress distribution when the structure is subject to spatially temperature gradient.	102
Figure 58: Iteration history of compliance and stress for problem in Equation (125).....	102

Figure 59: Final topology and stress distribution of stress-constrained topology optimization subject to spatially temperature gradient.	103
Figure 60: Iteration history of stress constrained topology optimization for problem in Equation (126).	104
Figure 61: Flange structure and dimensions (unit: m).	105
Figure 62: Top view and bottom view of final topology for the pure elastic flange problem.	105
Figure 63: Top view and bottom view of final topology of the flange subject to a uniform temperature rise.	106
Figure 64: Conceptual exhaust system.	107
Figure 65: Dimensions of the exhaust system (unit: m).	107
Figure 66: Side view (left) and front view (right) of the optimized exhaust.	108
Figure 67: (a) aircraft operating in high temperature; (b) wing rib structures; (c) design space of rib structure; (d) optimized rib structure.	111
Figure 68: An overview of the algorithm.	123
Figure 69: (a) A thin column, (b) CAD model, and (c) buckling mode.	125
Figure 70: Comparison of computational time between direct and adjoint method.	126
Figure 71: (a) compliance constrained elastic topology optimization; (b) buckling-compliance constrained elastic topology optimization; (c) buckling-compliance constrained thermal topology optimization from the adjoint method.	127
Figure 72: Iteration history of the adjoint approach.	128
Figure 73: Iteration history of compliance for different temperature rises.	129
Figure 74: Iteration history of buckling load factor for different temperature rises.	130
Figure 75: Wing rib structures with lower skin uninstalled [153].	131

Figure 76: Wing rib construction [153].	132
Figure 77: Leading-edge with a thickness of 0.1m, and applied boundary conditions (units are in meters).	133
Figure 78: Optimal designs for the rib leading-edge portion: (a) With buckling constraint but no thermal load; (b) With buckling constraint and thermal load.	134
Figure 79: Rib wing-box portion with a thickness of 0.1 m, and applied FEA boundary conditions.	135
Figure 80: Optimal designs for the wing box portion: (a) With buckling constraint but no thermal load; (b) With buckling constraint and thermal load.	136
Figure 81: An optimal micro-structural design [158].	140
Figure 82: An example of non-linear buckling analysis	141
Figure 83: An example of 3D printed structures designed by topology optimization	142

LIST OF TABLES

Table 1: Thermo-elastic topology optimization methods	11
Table 2: Constrained topology optimization methods.....	12
Table 3: Final topologies and results for compliance minimization of the bi-clamped structure.	34
Table 4: Final topologies and results for stress minimization of the bi-clamped structure.	34
Table 5: Final topology and results for compliance minimization of the bi-clamped structure with distributed load.....	35
Table 6: Final topologies and results for stress-minimization of the bi-clamped structure with distributed loads.....	35
Table 7: Final topologies and results for compliance minimization of cantilever beam.....	36
Table 8: Final topologies and results for stress minimization of cantilever beam.....	37
Table 9: Constraints and results for problem in Figure 20	51
Table 10: Constraints and results for problem in Figure 21	52
Table 11: Constraints and results for problem in Figure 22.....	53
Table 12: Constraints & results for problem in Figure 23.....	54
Table 13: Constraints & results for problem in Figure 24.....	55
Table 14: Constraints and results for problem in Figure 28.....	69
Table 15: Constraints and results for problem in Figure 31.....	71
Table 16: Constraints and results for problem in Figure 35.....	74
Table 17: Constraints and results for problem in Figure 40.....	78
Table 18: Constraints and results for problem in Figure 42.....	80
Table 19: Constraints and results for problem in Figure 42.....	81
Table 20: Sensitivity expressions.....	91

Table 21: Load ratios for different temperature variations	98
Table 22: Constraints and results for problem in Figure 62.	105
Table 23: Constraints and results for problem in Equation (127).....	106
Table 24: Constraints and results for problem in Equation (128).....	108
Table 25: Constraints and results for problem in Figure 71	127
Table 26: Constraints and results for problem in Figure 78	134
Table 27: Constraints and results for problem in Figure 80	136

1. INTRODUCTION TO THERMO-ELASTIC STRUCTURAL DESIGN

PROBLEMS

1.1 Structure Design in Thermal Environment

Structural optimization of elastic structures in thermal environment has become an important research area in recent years. Generally speaking, this research is concerned with optimization of structural components which are subject to both thermal gradients and mechanical restraints. If not properly accounted for, thermal expansions can lead to thermal stresses and structural failure. Traditionally, in order to reduce or eliminate thermal stresses, most efforts were devoted to designing thermal structures that allow thermal expansions to be accommodated in some or all necessary directions. Examples of this design approach include expansion joints in concrete structures and gas turbine engine components.

Nonetheless, several new design concepts, including engine exhaust-washed structure (EEWS) on a low observable aircraft, have resulted in new design scenarios in which mechanical constraints have to be considered. A concept of EEWS located aft of embedded engine is shown in Figure 1. High temperature exhaust gases are generated from the embedded engine and sprayed out through exhaust nozzle. During the process, not only the spray nozzle, aircraft engine, supporting substructures but also surrounding airplane skins are subject to high temperature gradients and aerodynamic forces.

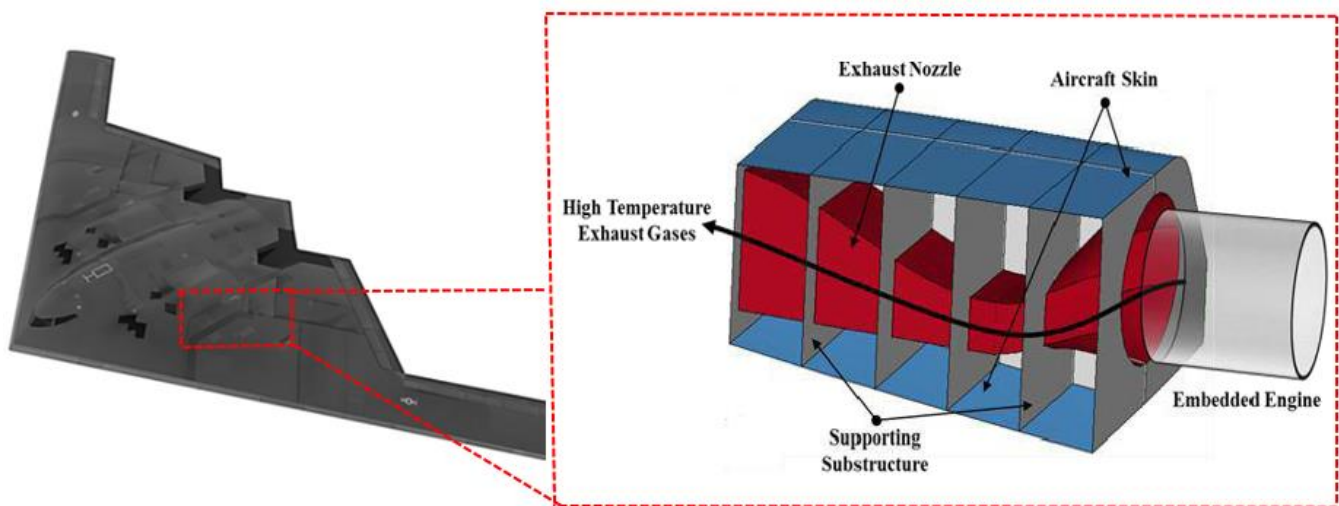


Figure 1: Conceptual engine exhaust-washed structure [1]

For this new design scenario, finding optimal designs for the nozzle structure by properly accommodating thermal expansions is not practical. Therefore, new optimization techniques are required. Topology optimization, as one of the most advanced design techniques, is an ideal candidate.

1.2 Literature Review of Topology Optimization

One of the earliest topology optimization works appear in [2] where K. Cheng and N. Olhoff demonstrated a shape and size optimization method for thickness distribution of elastic plates. A continuation study is followed in which M. Bendsoe introduced the material distribution method for topology designs [3]. This material distribution method was later adopted and modified by a number of researchers [4]. In the following years, various topology optimization methods were developed including ground structure methods [5], homogenization method [6], Solid Isotropic Material with Penalization (SIMP) [7], evolutionary structural optimization (ESO) [8] and level-set method [9], [10].

Ground structure approach is the classic method for optimizing the topology of truss systems. In this approach, a network of potential truss members is first prescribed in a design domain. A size

optimization is carried out on each truss member until the cross-section areas of non-optimal trusses approach zero and can therefore be removed [5].

SIMP is the most popular topology optimization formulation due to its simplicity, generality and success in several applications [7]. Based on the finite element method (FEM), SIMP assigns each element with a pseudo-density, and the pseudo-densities are then optimized to meet the desired objective. Due to its simplicity and generality [7], SIMP has been applied to a variety of problems, including fluids, structural mechanics, and thermo-elasticity.

In evolutionary structural optimization (ESO) [8], elements are gradually removed from the domain based on their relative significance order. BESO [11] addresses some of the limitations of ESO by permitting the insertion of elements.

The level-set method was developed by [12] and introduced to structural optimization by [13]. Level-set formulation is gaining popularity in topology optimization since it permits an unambiguous description of the boundary, and therefore permits imposition of constraints on the boundary. The level-set formulation relies on an evolving level-set which is typically controlled via Hamilton-Jacobi equations [14]. Readers are referred to [14] for a recent review of the success of level-set based methods in structural topology optimization.

In spite of recent advances in pure mechanical problems, topology optimization still faces numerous challenges in thermo-elastic designs: (1) In elastic problems external loads are independent of design variables, while the calculation of thermal loads is directly based on design variables. Due to the inherent design-dependent property, numerical challenges may arise, making traditional optimization algorithm no longer available. (2) Compared with compliance, stress constraints in thermal topology optimization needs more careful treatment [15] and is arguably more important [16]. (3) A variety of constraints may have to be considered. Previous efforts adopted a series of heuristic approaches, like a

worst case method or a weighted method [17]. Although these methods are practically easy to implement, they are theoretically incorrect. Therefore, a new correct methods are needed. (4) Structures are often subject to more than one load in optimization. Multi-load design scenarios are so numerically challenging that a majority of current topology optimization algorithms are incapable. (5) When a thermal structure is restrained at boundaries, excessive thermal stress may result in various failures, for example buckling. A systematic approach is required to consider such failures in design process.

A brief literature review of topology optimization with respect to the above challenges is summarized in the following sections.

1.2.1 Review of thermo-elastic topology optimization

Homogenization

In a pioneering work of solving thermo-elastic topology optimization problems, the authors of [18] adopted homogenization approach where they combined asymptotic homogenization on periodic microstructures with thermo-elastic finite element formulations. It was found structures can be underutilized due to presence of thermal strains, and final topology is considered as a strong function of thermal gradients. From a computational perspective, the increase in check-board patterns was also observed; methods to overcome these issues were also proposed.

SIMP

In [19], the strain energy was minimized considering thermo-mechanical coupling where the sensitivity was calculated by adjoint method. In [1], a restrained thermal expansion problem was studied to minimize compliance in a homogeneous thermal environment. In [20], a pre-buckling problem was studied where a time-harmonic load was imposed on structures with prescribed excitation frequency. In [21], thermal dynamic compliance at resonance frequencies was minimized where final topologies were

strongly affected by excited modes and load locations. In [22], thermal stress was minimized within a functionally graded structure by using an iso-geometrical approach. In [23], thermal gradient was considered for a compliance minimization problem which was solved by a guide-weight method. In [24], compliance and elastic strain energy were compared when they were used as thermal topology optimization objects.

RAMP

One of the challenges with the SIMP model is that the material interpolation exhibits zero slope at zero density, leading to parasitic effects in thermo-elastic problems [25], [26]. To overcome this deficiency, the Rational Approximation of Material Properties (RAMP) was developed by Stolpe and Svanberg [25]; its superior performance over SIMP was demonstrated in [26]. In [27], a new stress-relaxation method was proposed to include stress constraints, and a group-wise p-norm stress aggregation was adapted for better stress control.

ESO

For thermo-elastic problems, ESO was applied in [28] where a thermal source was placed inside the design domain and the temperature of the domain was minimized by removing elements with low sensitivities.

Level-set

For thermo-elastic problems, the level-set method was first reported in [29] where the mean compliance was minimized. In [30], a level-set based method was developed to study the effects of including material interface properties to thermo-elastic multi-phase structures. In [31], topological sensitivity was exploited within the Pareto framework to solve 2D stress-constrained topology optimization problems subject to uniformly elevated temperature.

All the relevant literatures are summarized in Table 1 in a chronological order.

1.2.2 Review of multi-load multi-constrained topology optimization

Multi-load topology optimization

For multi-load problems, one can either adopt a worst-case approach or a weighted approach; these are not necessarily equivalent [17]. In the former, one arrives at a feasible but non-optimal solution. In the latter, the weights are subjective and difficult to establish a priori; the final topology will depend on the weights [7], [32], [33]. Additionally, due to convergence issues, application-specific methods have also been developed [34], [35]. For truss structures, an alternate approach based on the “envelope strain energy” was proposed in [36], but its advantages for continuum structures is not known.

In [35], [37], [38], for multi-load problems, the authors propose an alternate discrete variable approach for mass minimization while satisfying various performance constraints, such as deflections, stress, etc. This has the advantage of synthesizing a minimum-mass solution that can satisfy many performance requirements. However, as stated by the authors [45], the underlying formulation is based on a heuristic measure.

Multi-load problems are fairly common in compliant-mechanism design [6], [39]–[42]. Specifically, one must solve (at least) two problems: (1) the primary problem involving the external load, and (2) an auxiliary problem with a unit load at the ‘output’ location. Further, multiple objectives must be met in the design of compliant mechanisms. These objectives are usually combined into a single weighted objective involving quantities such as the internal strain energy and mutual strain energy [39], [43]. Displacements constraints were included using a heuristic weighting approach [41], [44]. In [45], the topological level-set was exploited to solve multi-load problems, but the weights were once again determined in an ad hoc fashion.

Constrained topology optimization

To solve a constrained topology optimization problem, a constrained optimization algorithm must be chosen.

Various optimization algorithms have been developed, including method of moving asymptotes (MMA) [46], optimality criteria (OC) [47], simplex method [48], interior point method [49], Lagrangian multiplier method [49], augmented Lagrangian method [49] and so on. We review below various combinations of topology optimization formulations and optimization algorithms that have been proposed. A chronological summary of relevant literature is provided in Table 2 where the abbreviations of letter ‘M’, ‘D’, ‘C’, ‘S’, ‘E’ and ‘B’ stand for the constraint types of manufacturing, displacement, compliance, stress, eigen-value and buckling, respectively. The table and the review that follows are representative but not exhaustive; for example, constrained ground structures methods [50], [51], [52] are not reviewed here.

SIMP

Initially, SIMP was employed to solve compliance minimization problems [53]; it then evolved to include constraints. For example, one of the earliest SIMP-based stress-constrained topology optimization implementation was reported in [54] where authors coalesced local stress constraints into a global stress constraint, and addressed instability issues via a weighted combination of compliance and global stress constraints. Further research on compliance and stress-constrained SIMP-based topology optimization are discussed in [55], [56], [57], [58] and [59].

In [60], the authors proposed a SIMP-based trust-region method combined with augmented Lagrangian to solve a topology optimization problem of continuum structures subject to failure constraints. In [61], a Heaviside design parameterization was used in SIMP to consider manufacturing

constraints. The authors in [62] implemented SIMP with MMA to solve a topology optimization problem with compliance and manufacturing constraints. In [63], using SIMP, a manufacturing constraint and a unilateral contact constraint were absorbed into compliance minimization formulation through augmented Lagrangian method. In [64], the authors used a modified SIMP formulation coupled with quadratic programming technique to minimize structural weight subject to multiple displacement constraints. The authors in [65] used MMA to solve a topology optimization problem with a probability-based high-cycle fatigue constraint. In [66], an algorithm was proposed to address multi-scale topology optimization problems subject to multiple material design constraints. In [67], a multi-point approximation algorithm was used as optimizer in a continuum structure topology optimization problem subject to dynamic constraints. In [68], a global/regional stress measurement combined with an adaptive normalization scheme was proposed to address stress constraints. A salient feature in [68] is the proposed adaptive stress-scaling that ensures that the stress constraints are met precisely at termination; however, methods to include additional constraints (example, displacement constraints) were not addressed.

ESO/BESO

In [69], a principal-stress based ESO method was proposed to find the optimal design of cable-supported bridges subject to displacement and frequency constraints. During each optimization iteration, based on a threshold, elements were removed from the design domain. A similar method was used in [70] to solve contact design problems, where the authors proposed the interfacial gap between components be treated as optimization variables, while the contact stress be treated as an objective function. In [71], the Lagrangian multiplier method was used with BESO to combine the objective function of structural stiffness with a local displacement constraint. In [72], a modified BESO method

was combined with optimality criteria to solve a topology optimization problem with natural frequency constraints. The authors argued this method can successfully avoid artificial local modes.

Level-Set

In [73], X-FEM based level-set and OC method were combined to find optimal designs for continuum structures with geometric constraints. In [74], a topological level-set method was coupled with an adapted weight method for solving stress-constrained compliance minimization problem. In [75], the authors combined classic shape derivative and level set method for front propagation; the Lagrangian multiplier technique was used for perimeter-control. Since there was no implemented mechanism for creation of holes, the final design was dependent on initial material layout. In [76], the augmented Lagrangian technique was combined with the topological sensitivity based level-set method to handle displacement, stress and compliance constraints.

In [77], level-set/X-FEM combined with a shape equilibrium constraint strategy was proposed. Specifically, a topology optimization problem with stress constraint was formulated through Lagrangian multiplier method which was then iteratively solved. In [78], a level-set based method was derived to handle casting constraints; augmented Lagrangian method was applied for posing the constraints and calculating the shape derivative of objective function. In [79], a level-set based method was applied to the representative wing box of NASA Common Research Model to find the optimal 3-D aircraft wing structures. Compliance was minimized while balancing the aerodynamic lift and total weight. The level-set was shown to be robust and efficient by finding optimum solutions for multiple aerodynamic and body force load cases.

1.3 Thesis Overview

The thesis is organized as follows. In the second chapter, a typical single-load topology optimization problem is studied with SIMP. The disadvantages and limitations of SIMP are discussed. In the third chapter, a remedy to overcome these challenges is presented in the context of topology sensitivity based level-set method. It is followed by a necessary technical background and an application in Pareto. In the fourth chapter, a weakly-coupled thermo-elastic topology optimization problem is studied on simple 2D benchmark examples. In the fifth chapter, an augmented Lagrangian formulation is implemented with topology sensitivity based level-set method for multi-load multi-constrained design scenarios. The algorithm is tested on 2D benchmark examples. In the sixth chapter, the proposed augmented Lagrangian method is applied for 3D large-scale models whose underlying FEA are accelerated by congruent gradient deflated method, element voxelization and high performance computing (HPC). Also, topological sensitivities with respect to a variety of mechanical properties are derived. In the seventh chapter, the thermo-elastic topology optimization is combined with augmented Lagrangian topological sensitivity based level-set method for 3D large-scale models. An application of the proposed algorithm in multi-constrained thermal buckling problems is present in Chapter 8. In the ninth chapter, conclusion and future work are given.

Table 1: Thermo-elastic topology optimization methods

Time	Authors	TO method	TO objective	TO constraints	Thermal gradient?	Dimension
1995	H. Rodrigues[18]	Homogenization	Compliance	Volume	√	2
1999	Q. Li[35]	ESO	Displacement	Element thickness	-	2
2001	L. Yin[36]	SIMP	Output displacement	Volume, element density	-	2
2003	Y. Li[37]	SIMP	Compliant mechanism	Volume, element density	-	2
2004	Q. Li[28]	ESO	Temperature	Non-negative sensitivity	-	2
2005	S. Cho[38]	SIMP	Compliance	Volume, element density	-	2
2006	W. Kim[39]	ESO	Stress/ Eigen-value	Volume	-	2
2006	M.Prithiviraj[40]	ESO	Volume	Stress/ Eigen-value	-	3
2008	Q. Xia [29]	Level-set	Compliance	Volume	-	2
2008	J. Yan[41]	SIMP	Compliance	Volume, element density	-	2
2010	D. Li [19]	SIMP	Compliance	Volume, element density	-	2
2010	P. Pederson[42]	SIMP	Stress	Volume, element density	-	2
2010	T.Gao[43]	RAMP	Compliance	Volume, element density	-	2
2012	J. Deaton[1]	SIMP	Compliance	Volume, element density	-	2
2012	P. Pederson[44]	RAMP	Stress	Volume, element density	-	3
2012	J. Yang[45]	SIMP	Compliance	Volume, element density	-	2
2013	J. Deaton[46]	RAMP	Volume	Stress	-	2
2013	X. Yang[20]	SIMP	Compliance /Buckling	Volume, element density	-	2
2014	X. Yang[21]	SIMP	Eigen-value	Volume, element density	-	2
2014	A.H. Taheri[22]	SIMP	Stress	Volume, element density	-	2
2014	N.Vermaak[30]	Level-set	Compliance	Volume	-	2
2014	X. Liu[23]	SIMP	Compliance	Volume, element density	√	2,3
2014	W. Zhang[24]	SIMP	Compliance /strain energy	Volume, element density	-	2
2014	S. Deng[31]	Level-set	Stress	volume	-	2
2015	J. Deaton[80]	RAMP	Compliance	Stress, Volume element density	-	2

<i>Proposed</i> ¹²	<i>S. Deng, K. Suresh</i>	<i>Level-set</i>	<i>Volume</i>	<i>Compliance, Stress, buckling</i>	√	3
-------------------------------	---------------------------	------------------	---------------	-------------------------------------	---	---

Table 2: Constrained topology optimization methods.

Time	Authors	TO Method	OPT Method	Constraints						Dimension
				M	D	C	S	E	B	
1987	Svanberg [46]	Convex approximation	MMA		√		√	√		2
1992	Zhou, Rozvany [81]	SIMP	OC				√			2
1996	R. Haber [82]	Homogenization	Interior penalty method	√		√				2
1997	M. Kocvara [50]	Ground structure	Interior point method		√	√				2
1998	J. Petersson, O. Sigmund [83]	SIMP	Linear programming	√		√				2
2001	L. Yin, et. al. [84]	SIMP	OC		√		√	√		2
2002	H. Guan, Y. Chen[69]	ESO	Parameterized criteria		√		√	√		2
2003	W. Li, Q. Li [70]	ESO	Parameterized criteria	√						2
2004	J. Pereira, E. Fancello [60]	SIMP	Augmented Lagrangian				√			2
2004	G. Allaire, et.al. [85]	Level-set	Lagrangian multiplier	√		√				2,3
2006	K. Zuo, L. Chen [62]	SIMP	Modified MMA	√		√				3
2007	M. Stolpe, T. Stidsen [86]	Hierarchical optimization	Linear programming		√		√			2
2008	M. Werme [57]	SIMP	Linear programming			√	√			2
2008	M. Bruggi, P. Venini [58]	SIMP	MMA		√	√	√			2
2009	J. Paris, F. Casteleiro [87]	SIMP	Simplex method			√	√			2,3

¹ S. Deng, K. Suresh, “Thermo-elastic topology optimization via augmented topological level-set”, Computers and Structures, 2016, submitted.

² S. Deng, K. Suresh, “Topology optimization under thermos-elastic buckling”, Structures and Multidisciplinary Optimization, 2016, submitted.

2009	A. Ramani [38]	Heuristic	Substitution		√	√	√				2,3
2010	X. Huang, Y Xie [71]	BESO	Lagrangian multiplier		√	√					2
2010	X. Huang, et. al. [72]	BESO	OC					√			2,3
2010	N. Stromberg [63]	SIMP	Augmented Lagrangian	√		√					2,3
2010	S. Yamasaki, T. Nomura [88]	Level-set	Augmented Lagrangian	√		√					2,3
2010	J. Rong, J. Yi [64]	SIMP	Quadratic programming		√						2
2011	A. Gersborg [61]	SIMP	MMA	√							2
2012	M. Bruggi, P. Duysinx [59]	SIMP	MMA			√	√				2
2013	T. Liu, S. Wang [73]	Level-set	OC	√							2
2013	M. Wang, L. Li [77]	Level-set	Lagrangian multiplier				√				2
2013	G. Allaire [78]	Level-set	Augmented Lagrangian	√		√					2,3
2013	K. Suresh, et.al. [74]	Level-set	Adaptive weight			√	√				2,3
2014	S. Deng, K. Suresh [76]	Level-set	Augmented Lagrangian		√	√	√				2
2014	P. Dunning, B. Stanford [79]	Level-set	Lagrangian multiplier			√					3
2014	E. Holmberg [65]	SIMP	MMA				√				2
2015	P. Coelho, H. Rodrigues [66]	SIMP	MMA	√	√						2,3
2015	J. Li, et. al. [67]	SIMP	Multi-point Approximation					√			3
<i>Proposed³</i>	<i>S. Deng, K. Suresh</i>	<i>Level-set</i>	<i>Augmented Lagrangian</i>	√	√	√	√	√	√		3

³ S. Deng and K. Suresh, “Multi-constrained 3D topology optimization via augmented topological level-set,” *Comput. Struct.*, vol. 170, no. 1, pp. 1–12, 2016.

2. INTRODUCTION TO TOPOLOGY OPTIMIZATION

Over the last two decades, topology optimization [55], [90] has accelerated from an academic exercise into an exciting discipline with, potentially, numerous industrial applications. The focus of this chapter is specifically on introduction of topology optimization.

2.1 A Pure Elastic Unconstrained Topology Optimization

In structural mechanics, a constrained topology optimization problem may be posed as (see Figure 2):

$$\begin{aligned}
 & \underset{\Omega \subset D}{\text{Min}} \varphi(u, \Omega) \\
 & g_i(u, \Omega) \leq 0; i = 1, 2, \dots, m \\
 & \text{subject to} \\
 & Ku = f
 \end{aligned} \tag{1}$$

where:

D : Domain within which the topology must lie

f : External force vector

g_i : Constraints

K : Finite element stiffness matrix

m : Number of constraints

u : Finite element displacement field

φ : Objective to be minimized

Ω : Topology to be computed



Figure 2: A single-load structural problem.

For example, a special case of Equation (1) is the compliance-minimization topology optimization problem:

$$\begin{aligned}
 & \underset{\Omega \subset D}{\text{Min}}(J = f^T u) \\
 & \text{subject to} \\
 & Ku = f \\
 & v \leq v_D
 \end{aligned} \tag{2}$$

where:

J : Compliance
 v : Volume fraction
 v_D : Desired volume fraction

Figure 3 illustrates the solution to a specific instance of Equation (2) where the allowable final volume fraction is 0.5.

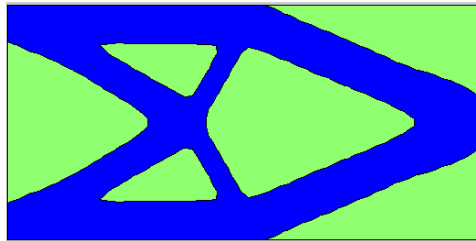


Figure 3: Optimal topology for a specific instance of Equation (2) over the structure in Figure 2.

While various methods have been proposed to solve the specific instance of the single-load topology optimization problem, Solid Isotropic Material with Penalization (SIMP) is the most popular one. A brief review of the basic SIMP scheme is discussed in the following sections.

2.2 A Popular Topology Optimization Method: SIMP

2.2.1 SIMP Formulation

Building upon finite element analysis (FEA), SIMP is a widely used material interpolation scheme. It is essentially a power law as shown in Equation (3) which interpolates material properties to the scalar field in each finite element.

$$\begin{aligned}
 E_e(\rho_e) &= \rho_e^p E_0 \\
 \text{with} \\
 0 < \rho_e &\leq 1
 \end{aligned}
 \tag{3}$$

Where

- e : Finite elements
- E_e : Penalized Young's modulus in elements
- E_0 : Young's modulus
- p : Penalization parameter
- ρ_e : Pseudo-density in elements

In this formulation, the elemental material Young's modulus E_e becomes a function of elemental pseudo-density ρ_e and penalization parameter p which is generally varied between 1.0 and 3.0. Therefore, SIMP can be seen as a procedure where different microstructures are placed at each point in design domain to optimize the structural global properties [91].

Topology optimization implies a discrete optimization at every point in design domain. In other words, an optimized point in the domain is supposed to be only material “full” or “void”. This is not only physically reasonable but also easy for manufacturing. However, implementation of such a discrete optimization scheme is not practical [91]. Therefore, a continuous optimization

strategy, whose design variable ρ_e can be continuously varied between 0.0 and 1.0, is adopted. It is noted the pseudo-density value is usually not taken as 0.0 to avoid numerical singularity.

A typical SIMP procedure is as follows. First, the design domain (for example, Figure 2) is discretized by finite elements (Figure 4). In this way, each finite element is assigned with a pseudo-density ρ_e , and each ρ_e value is initialized to the desired volume fraction, 50% for instance. Second, based on the finite element formulation and the power-law approach in Equation (3), the compliance-minimization topology optimization problem in Equation (2) can be re-stated by SIMP as:

$$\begin{aligned}
 & \text{Minimize: } J = u^T K u \\
 & \text{Subject to: } f = K u \\
 & \sum_{e=1}^N v_e \rho_e = 50\% \\
 & 0 < \rho_e \leq 1
 \end{aligned} \tag{4}$$

Third, the optimization problem stated in Equation (4) can be solved by several methods, including Optimality Criteria (OC), Method of Moving Asymptotes (MMA), etc. During the optimization, the updating scheme of design variables, calculation of sensitivity fields and stopping criteria are discussed in detail in [7].

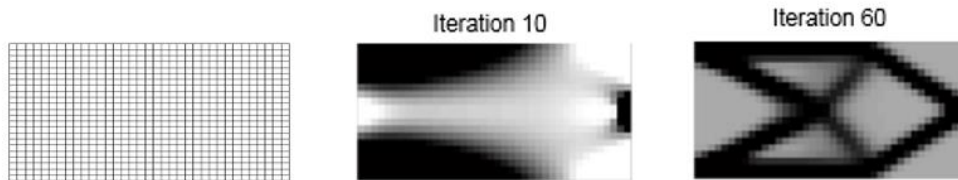


Figure 4: Finite element mesh and progression in SIMP.

2.2.2 Limitations and Disadvantages

Although SIMP is easy to implement and widely used, it suffers several disadvantages.

First, since the material density is penalized to be continuously changed from 0.0 to 1.0, the intermediate densities (i.e. between 0.0 and 1.0) have no real physical meaning in structures. Due to this inherent deficiency, several other challenges may include: (1) when the boundary elements have intermediate pseudo-densities, a boundary condition cannot be explicitly enforced; (2) the structures with “gray” elements of intermediate densities often have high condition numbers, leading to convergent problems; (3) using different penalization parameters may lead to distinct final designs; (4) the “gray” elements are physically nonsense and manufacturing infeasible; (5) “gray” elements can lead to other numerical challenges, like checker-board patterns.

Second, since SIMP is developed on a single-load strain energy minimization formulation, it is theoretically infeasible to handle problems with multiple loads. Third, when the design-dependent thermal loads are applied on design domain, SIMP suffers from a specific numerical deficiency, called “zero sensitivity at zero densities”. This defect may lead to more “gray” elements during optimization compared with pure elastic case [15].

Several other topology optimization methods are developed trying to remedy those shortcomings. Level-set, as one of the newly proposed methods, shows promising features. Topological sensitivity based level-set is therefore utilized in this research [76], [92]. In the following chapter, a brief review of its technical background is given.

3. INTRODUCTION TO TOPOLOGICAL SENSITIVITY BASED LEVEL-SET METHOD

In this chapter, the method of topological sensitivity based level-set method is introduced. The proposed method is based on the concept of topological sensitivity which is reviewed first.

3.1 Topological Sensitivity

Topological sensitivity captures the first order impact of inserting a small circular hole within a domain on various quantities of interest. This concept has its roots in the influential paper by Eschenauer [94], and has later been extended and explored by numerous authors [95]–[99], [100] including generalization to arbitrary features [101]–[103].

Consider again the problem illustrated earlier in Figure 2. Let the quantity of interest be Q (example: compliance) that is dependent on the field u . Suppose a tiny hole is introduced, i.e., modifying the topology, as illustrated in Figure 5. The solution u from the static equilibrium equation and the quantity Q will change. The topological sensitivity (aka topological derivative) is defined in 2-D as:

$$\mathcal{T}_Q(p) \equiv \lim_{r \rightarrow 0} \frac{Q(r) - Q}{\pi r^2} \quad (5)$$

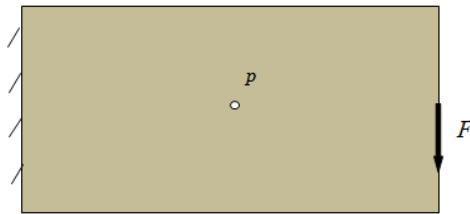


Figure 5: A topological change.

To find a closed-form expression for the topological sensitivity, often one relies on the concept of an adjoint. Recall that the adjoint field associated with a quantity of interest satisfies [104]–[106]:

$$K\lambda = -\nabla_u Q \quad (6)$$

Once the adjoint is computed, the topological derivative is given by [107], [106]:

$$\mathcal{T}_Q = -\frac{4}{1+\nu} \sigma(u) : \varepsilon(\lambda) + \frac{1-3\nu}{1-\nu^2} \text{tr}[\sigma(u)] \text{tr}[\varepsilon(\lambda)] \quad (7)$$

where

$\sigma(u)$: Stress tensor of primary field
 $\varepsilon(\lambda)$: Strain tensor of adjoint field

Thus, given the stress and strain field in the original domain (without the hole), one can compute the topological sensitivity over the entire domain.

Observe that, as a special case, when $Q = f^T u$, i.e., in the case of compliance, Equation (6) reduces to:

$$K\lambda = -f \quad (8)$$

In other words we arrive at $\lambda = -u$ as expected, and the topological sensitivity reduces to [107]:

$$\mathcal{T}_J(p) = \frac{4}{1+\nu} \sigma : \varepsilon - \frac{1-3\nu}{1-\nu^2} \text{tr}(\sigma) \text{tr}(\varepsilon) \quad (9)$$

If the domain is discretized into 2000 elements, and a unit is applied, the resulting field is illustrated in Figure 6; the magnitude of topological sensitivity field is normalized to 1.0 for convenience. In 3-D, the topological sensitivity field for compliance is given by [98]:

$$\mathcal{T}_J = -20\mu\sigma : \varepsilon + (2\mu - 3\lambda)tr(\sigma)tr(\varepsilon) \quad (10)$$

where μ and λ are the Lamé parameters.

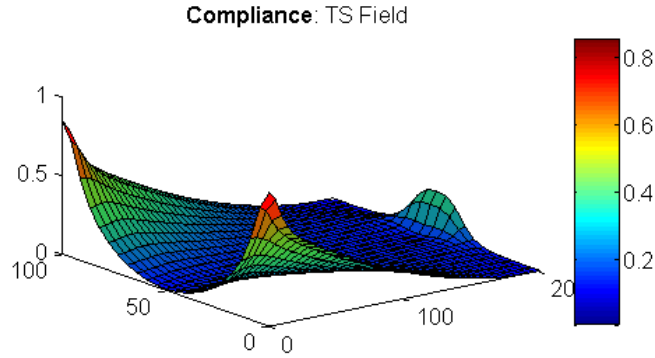


Figure 6: Topological sensitivity field.

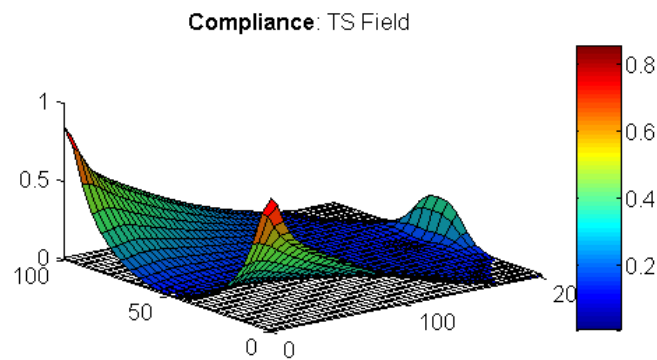
3.2 Topological Level-set

A simple approach to exploiting topological sensitivity in topology optimization is to ‘kill’ mesh-elements with low values. However, this leads to instability and checker-board patterns. Alternately, the topological sensitivity field can be used to introduce holes during the topology optimization process via an auxiliary level-set [75]. Here, we directly exploit the topological sensitivity field as a level-set, as described next (also see [108]).

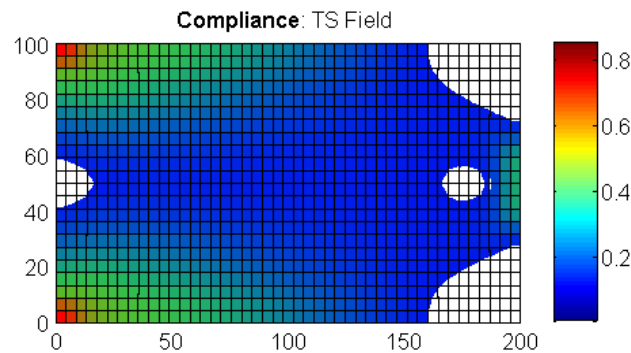
Consider again the compliance field illustrated in Figure 6; this is reproduced below in Figure 7a together with a cutting plane corresponding to an arbitrary cut-off value of $\tau = 0.03$. Given the field, and the cutting plane, one can define a domain Ω^τ per:

$$\Omega^\tau = \{p \mid \mathcal{T}_j(p) > \tau\} \quad (11)$$

In other words, the domain Ω^τ is the set of all points where the topological field exceeds τ ; the induced domain Ω^τ is illustrated in Figure 7b. Now, the τ value can be chosen such that, say, 10% of the volume is removed. It is observed that the elements at the left-corners, as well as where the force is applied have relatively high sensitivity values while the sensitivity values for the elements at right corners are relatively low. Since elements with lower topological sensitivity values are least critical for the stiffness of the structure, they are likely to be eliminated. In other words, a ‘pseudo-optimal’ domain has been constructed directly from the topological sensitivity field.



(a) Compliance topological sensitivity.



(b) Induced domain Ω^τ for a volume fraction of 0.95

Figure 7: Topological sensitivity field as a level-set.

However, the computed domain may not be ‘optimal’ [109], i.e., it may not be the stiffest structure for the given volume fraction. One must now repeat the following three steps: (1) solve the finite element problem over Ω^τ (2) re-compute the topological sensitivity, and (3) find a new value of τ for the desired volume fraction. In essence, a fixed-point iteration is carried out [99], [110], [111], involving three quantities (see Figure 8): (1) domain Ω^τ , (2) displacement fields u and v over Ω^τ , and (3) topological sensitivity field over Ω^τ .

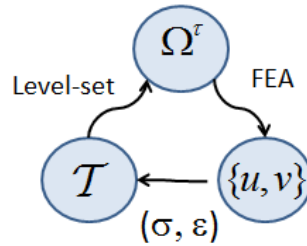


Figure 8: Fixed point iteration involving three quantities

Once convergence has been achieved (in typically 2~3 iterations), an optimal domain at 90% volume fraction will be obtained. An additional 10% volume can now be removed by repeating this process.

3.3 Pareto Method

Using the fixed point iteration algorithm in Figure 8, the compliance problem posed in Equation (1) can be solved. A series of pareto-optimal topologies are resulted and illustrated in Figure 9. Therefore, the algorithm is capable to find pareto-optimal solutions to the problem:

$$\text{Min}_{\Omega \subset D} \{J, |\Omega|\} \quad (12)$$

Since all topologies are pareto-optimal, the topology optimization problem in Equation (2) is trivially solved by terminating the algorithm when the desired volume fraction has been reached.

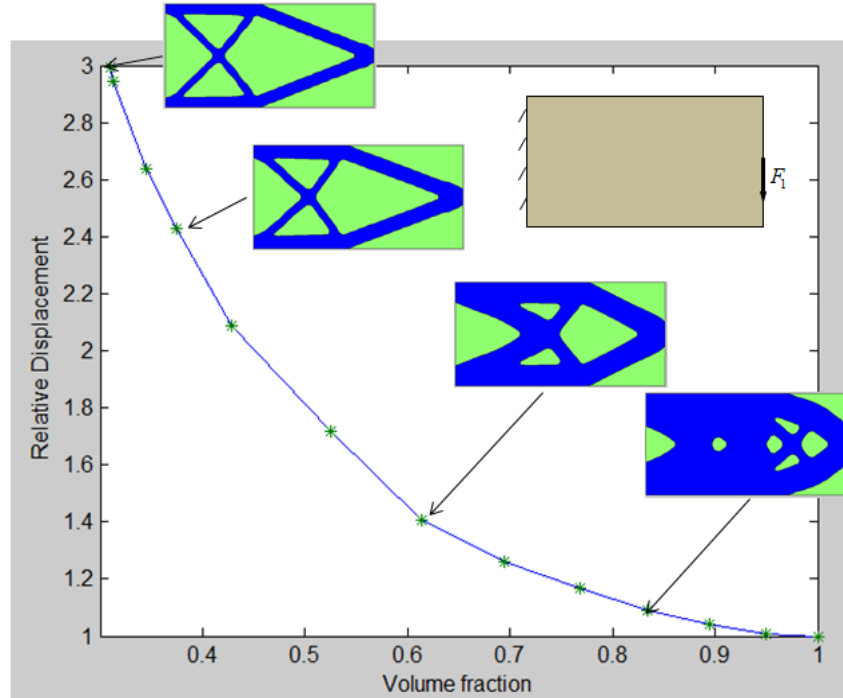


Figure 9: Pareto-optimal topologies

Observe that the above “Pareto” method is applicable to other objective functions (besides compliance) by replacing the compliance topological sensitivity field with the appropriate topological sensitivity field.

After the introduction of the concept of the topological sensitivity based level-set method, its application in thermo-elastic topology optimization problem is illustrated in Chapter 4 and its implementation with augmented Lagrangian approach is demonstrated in Chapter 5, respectively.

4. THERMO-ELASTIC TOPOLOGICAL LEVEL-SET METHOD

The focus of this chapter is to apply the topological sensitivity based level-set method to solve thermo-elastic topology optimization problems (see Figure 10) where the structure is subject to both mechanical and thermal loads. The goal is to find the optimal topology of minimum volume, subject to stress and compliance constraints. Unlike in pure elastic problems, in thermo-elastic problems, the displacements and stresses are computed after taking into account the additional thermal load. This poses both new theoretical and computational challenges discussed later in this chapter.

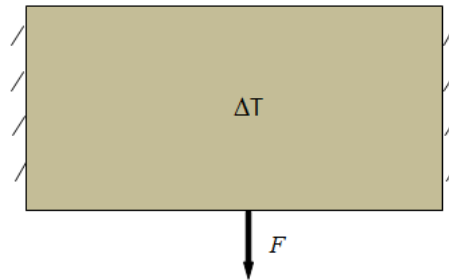


Figure 10: A thermo-elastic problem.

In the following sections, we first provide a brief review of necessary technical background. Then, the proposed thermo-elastic topology optimization and its implementation are discussed. Next, numerical experiments are presented, followed by conclusions.

4.1 Formulation of Thermal Elastic FEA

Finite element formulations of (weakly-coupled) thermo-elastic problems essentially reduce to solving two linear algebra problems:

$$K_t t = q \tag{13}$$

$$Ku = f + f^{th} \tag{14}$$

where:

- f : Mechanical load
- f^{th} : Structural load due to thermal effects
- K : Structural stiffness matrix
- K_t : Thermal stiffness matrix
- q : Thermal load
- t : Temperature field
- u : Displacement field

The thermal load vector in Equation (14) is formed via [112]:

$$f_e^{th} = \int_{\Omega_e} B_e^T D_e \varepsilon_e^{th} d\Omega \quad (15)$$

$$\varepsilon_e^{th} = \alpha(t_e - t_0)\Phi^T \quad (16)$$

where:

- B_e : Element strain-displacement matrix
- D_e : Element elasticity matrix
- e : Finite elements
- f_e^{th} : Nodal thermal load vector for each element
- t_e : Element temperature from thermal analysis
- t_0 : Reference temperature
- α : Thermal expansion coefficient
- ε_e^{th} : Element thermal strain vector
- Φ : [1 1 1 0 0 0] in 3D; [1 1 0] in 2D
- Ω_e : Element domain

Finally, the stresses are obtained by subtracting the thermal strain from the total strain, and multiplying the resulting strain by the material tensor:

$$\sigma_e = D_e B_e u_e - D_e \varepsilon_e^{th} \quad (17)$$

Further explanations and details may be found, for example, in [112]. The compliance for a thermo-elastic system is defined as:

$$J = (f + f^{th})^T u = u^T K u \quad (18)$$

Observe that Equation (14) represents a weakly-coupled problem where the thermal field influences the displacements, but not the inverse. Strongly-coupled thermo-elastic problems are beyond the scope of this thesis.

In this chapter, we extend the Pareto method to thermo-elastic problems with constraints. In particular, we consider two different formulations described in the following two sections. In both formulations, a compliance constraint and a stress constraint are imposed as follows:

$$J / J_0 \leq \eta_J \quad (19)$$

$$\sigma_{\max} / \sigma_0 \leq \eta_\sigma \text{ in } \Omega \quad (20)$$

Equation (19) states that the ratio of compliance J of the final topology to the compliance J_0 of the initial topology must not exceed a prescribed value of η_J .

Similarly, Equation (20) states that the ratio of maximum stress σ_{\max} (across all elements) in the final topology to the initial maximum stress σ_0 (across all elements) in the initial topology must not exceed a prescribed value of η_σ .

In the numerical experiments, η_J and η_σ range from 1.01 to 10.0, and they control the final termination. On the other hand, the path taken by the optimization process is controlled by choosing one of the two formulations described in Section 4.2.1 and 4.2.2

4.2 Formulation of Thermal Elastic Topology Optimization

In this chapter, we extend the Pareto method to thermo-elastic problems with constraints. In particular, we consider two different formulations described in Section 4.2.1 and 4.2.2. In both formulations, a compliance constraint and a stress constraint are imposed as follows:

$$J / J_0 \leq \eta_J \tag{21}$$

$$\sigma_{\max} / \sigma_0 \leq \eta_\sigma \text{ in } \Omega \tag{22}$$

Equation (21) states that the ratio of compliance J of the final topology to the compliance J_0 of the initial topology must not exceed a prescribed value of η_J .

Similarly, Equation (22) states that the ratio of maximum stress σ_{\max} (across all elements) in the final topology to the initial maximum stress σ_0 (across all elements) in the initial topology must not exceed a prescribed value of η_σ .

In the numerical experiments, η_J and η_σ range from 1.01 to 10.0, and they control the final termination. On the other hand, the path taken by the optimization process is controlled by choosing one of the two formulations described in Section 4.2.1 and 4.2.2.

4.2.1 Compliance Minimization

In the first formulation the objective φ is the compliance, i.e.:

$$\begin{aligned}
& \underset{\Omega \subset D}{\text{Min}} \{J, |\Omega|\} \\
& J / J_0 \leq \eta_J \\
& \sigma_{\max} / \sigma_0 \leq \eta_\sigma \text{ in } \Omega \\
& \text{subject to} \\
& Ku = f + f^{th} \\
& K_t t = q
\end{aligned} \tag{23}$$

In other words, the goal is to trace the pareto-optimal topologies involving compliance and volume fraction until the stress (in any element) exceeds all allowable value, or until the compliance exceeds a specified value. Such topologies will be referred to as *stiff topologies* for thermo-elastic problems.

4.2.2 Stress-Minimization

In the second formulation φ is the p-norm stress measure, i.e.:

$$\begin{aligned}
& \underset{\Omega \subset D}{\text{Min}} \{\sigma_p, |\Omega|\} \\
& J / J_0 \leq \eta_J \\
& \sigma_{\max} / \sigma_0 \leq \eta_\sigma \text{ in } \Omega \\
& \text{subject to} \\
& Ku = f + f^{th} \\
& K_t t = q
\end{aligned} \tag{24}$$

where σ_p is the p-norm stress measure [113] of the von Mises stress over all elements:

$$\sigma_p = \left(\sum_e (\sigma_e)^p \right)^{1/p} \tag{25}$$

The goal is to trace the pareto-optimal topologies involving the global stress measure and volume fraction until the stress (in any element) exceeds a specified value, or until the

compliance exceeds a specified value. Such topologies will be referred to here as *strong* topologies.

Generating ‘strong’ topologies is computationally more expensive than generating ‘stiff’ topologies [54], but arguably more important [16].

4.2.3 Analytical Topological Sensitivity Fields

For each of the two formulations, the topological sensitivity field associated with the objective φ must be computed. For the compliance, the topological sensitivity expression is well-known and is given by [107]:

$$\mathcal{T}_J = \frac{4}{1+\nu} \sigma : \varepsilon - \frac{1-3\nu}{1-\nu^2} \text{tr}(\sigma) \text{tr}(\varepsilon) \quad (26)$$

Note that the strain fields in Equation (26) is the total strain, while the stress field is computed via Equation (17).

For the p-norm stress field, the topological sensitivity depends not only on the primary displacement field u but also on an adjoint field λ [74]:

$$\mathcal{T}_{\sigma_p} = \frac{4}{1+\nu} \sigma(u) : \varepsilon(\lambda) - \frac{1-3\nu}{1-\nu^2} \text{tr}(\sigma(u)) \text{tr}(\varepsilon(\lambda)) \quad (27)$$

The adjoint field associated with the p-norm stress, by definition, satisfies the following equation [104]:

$$K\lambda = -\nabla_u (\sigma_p) \quad (28)$$

Using the definition in Equation (25), one can show that (see [74]):

$$\nabla_u(\sigma_p) = -\frac{1}{p} \left(\sum_e (\sigma_e)^p \right)^{1/p-1} \left[\sum_e g_e \right] \quad (29)$$

and

$$g_e = 0.5p(\sigma_e)^{p-2} \left(\begin{array}{l} (2\sigma_{11} - \sigma_{22})(F_{1,:}) + (2\sigma_{22} - \sigma_{11})(F_{2,:}) + \\ 6\sigma_{12}F_{3,:} \end{array} \right) \quad (30)$$

$$[F] = [D][B] \quad (31)$$

4.3 Algorithm of Thermo-Elastic Topological Level-Set

- 1) Once the topological sensitivities can be computed, the overall algorithm (for both formulations) is fairly simple, and proceeds as follows:
- 2) The optimization starts at a volume fraction of 1.0. The ‘current volume fraction’ ν is set to 1.0, and ‘volume decrement’ $\Delta\nu$, is set to 0.05.
- 3) The thermal and structural finite element problems in Equation (14) are solved, and the total strain and stress are extracted at the center of each element. For the stress-objective, an additional adjoint problem in Equation (28) is solved.
- 4) The topological sensitivity field (Equation (26) or (27)) is computed at the center of each element, and locally smoothed with neighboring elements.
- 5) Treating the topological sensitivity field as a level-set, a new topology with a volume fraction of $(\nu - \Delta\nu)$ is extracted. The compliance is computed over the new topology. If the compliance has converged, then the optimization moves to the next step, else it returns to step 2.
- 6) The current volume fraction is set to $(\nu - \Delta\nu)$, and the optimization returns to step 2, until the final volume fraction is reached or until one of the constraints is violated.

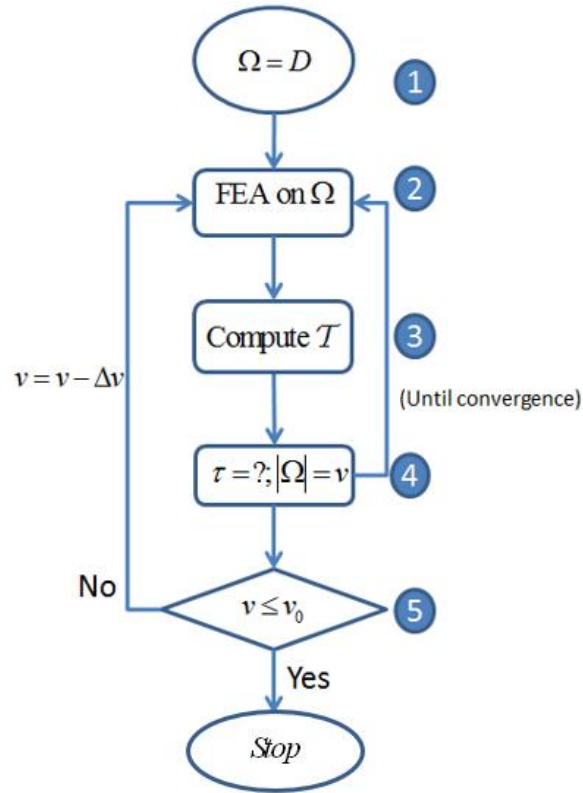


Figure 11: An overview of the algorithm.

4.4 Numerical Experiments

- In this Section, we demonstrate the proposed method through numerical experiments. The default parameters are as follows:
 - The material is assumed to be steel, i.e., the elastic modulus is $E = 2e11 Pa$, the Poisson's ratio is $\nu = 0.3$ and the coefficient of thermal expansion $\alpha = 1.1e-5$.
 - The reference temperature is zero C, and a thermal load is applied by increasing the temperature uniformly by ΔT
 - Unless otherwise noted, the p-norm value is 8.

Bilinear quad elements are used for finite element analysis. For all experiments, the constraints are:

$$J / J_0 \leq 3.0 \quad (32)$$

$$\sigma_{\max} / \sigma_0 \leq 1.5 \quad (33)$$

Further, the desired volume fraction is 0.1. In other words, the optimization terminates if the constraints are violated or if the final volume fraction is reached.

4.4.1 Bi-clamped beam with a point load

The first experiment is inspired by the classic bi-clamped structure which was previously studied by Rodrigues and Fernandes [18]. As illustrated in Figure 12, the structure is clamped on right and left edges and a mechanical point load of $F = 1e6N$ is applied at the center of the bottom edge; the structure is also subject to a homogeneous temperature increase of ΔT . The domain is meshed with 4500 elements.

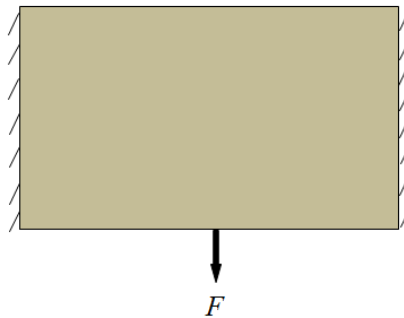





Figure 12: The bi-clamped structure with point-load.

Compliance Formulation (Stiff Designs)

The results of the compliance minimization problem for three different levels of temperature loadings are summarized in Table 3. Observe that the final volume fraction and the topologies are a strong function of the temperature increase. Compared to the default case (middle column), a lower volume fraction is reached with decrease in temperature (left column); both are

compliance constrained. On the other hand, with an increase in temperature, the structure is stress constrained (stress constraints are difficult to meet exactly).



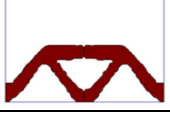
Table 3: Final topologies and results for compliance minimization of the bi-clamped structure.

ΔT	-1.0	0.0	1.0
Final topology			
v_{final}	0.106	0.175	0.205
J_{final}	$2.89J_0$	$2.98J_0$	$2.16J_0$
σ_{final}	$0.99\sigma_0$	$1.00\sigma_0$	$1.37\sigma_0$

Stress Formulation (Strong Designs)

The results of the *stress* minimization problem are summarized in Table 4. The results are similar to that of Table 3, except that in the last column, a lower volume fraction has been reached due to the compliance constraint. This highlights the difference between tracing compliance-minimization and tracing stress-minimization

Table 4: Final topologies and results for stress minimization of the bi-clamped structure.

ΔT	-1.0	0.0	1.0
Final topology			
v_{final}	0.112	0.183	0.155
J_{final}	$2.96J_0$	$2.97J_0$	$3.00J_0$
σ_{final}	$1.08\sigma_0$	$1.00\sigma_0$	$1.20\sigma_0$

4.4.2 Bi-clamped beam with distributed loads

Next we consider a similar bi-clamped beam but with distributed loads on the top edge as shown in Figure 13 [18]. The dimension of this beam is $0.5m \times 0.28m \times 0.01m$ and the distributed load is $6e9N/m^2$. The domain is meshed with 3200 finite elements and subject to three different uniform temperature changes.

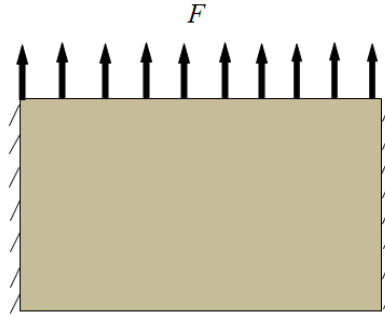





Figure 13: The bi-clamped structure with a distributed load.

Compliance Formulation (Stiff Designs)

The results of the *compliance minimization* problem for three different levels of temperature loadings are summarized in Table 5. Some minor differences in topologies are noted.


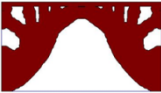
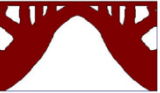
Table 5: Final topology and results for compliance minimization of the bi-clamped structure with distributed load.

ΔT	-20	0.0	20
Final topology			
v_{final}	0.355	0.40	0.375
J_{final}	$2.95J_0$	$2.88J_0$	$2.93J_0$
σ_{final}	$1.47\sigma_0$	$1.47\sigma_0$	$1.45\sigma_0$

Stress Formulation (Strong Designs)

The results of the corresponding *stress* minimization problem are summarized in Table 6. The topologies are consistent with those reported in [18]; relaxing the compliance constraint would result in a lower volume fraction.

Table 6: Final topologies and results for stress-minimization of the bi-clamped structure with distributed loads.

ΔT	-20	0.0	20
Final topology			
v_{final}	0.478	0.488	0.468
J_{final}	$2.99J_0$	$3.00J_0$	$2.99J_0$

σ_{final}	$1.43\sigma_0$	$1.41\sigma_0$	$1.42\sigma_0$
------------------	----------------	----------------	----------------

4.4.3 Clamped beam with tip load

The next example is illustrated in Figure 14, where a beam that is 1.5m long, 1m wide and 0.01m thick, is clamped on the left edge and subject to a point load $F = 5e8N$. The geometry is meshed with 3000 elements.






Figure 14: The cantilever beam problem.

Compliance Formulation (Stiff Designs)

The results of the compliance minimization problem for three different levels of temperature loadings are summarized in Table 7. The impact of temperature on the final result is minimal in this case, i.e., the structure is largely dominated by the external force.

Table 7: Final topologies and results for compliance minimization of cantilever beam.




ΔT	0	5	10
Final topology			
v_{final}	0.55	0.56	0.53
J_{final}	$1.55J_0$	$1.52J_0$	$1.60J_0$
σ_{final}	$1.50\sigma_0$	$1.49\sigma_0$	$1.50\sigma_0$

Stress Formulation (Strong Designs)

The results of the stress minimization problem are summarized in Table 8. The topologies are significantly different from those in Table 7. Also note that for a temperature increase of 5, the

final stress is much closer to the constraint of 1.5, hence a lower volume fraction has been reached; this is purely a numerical artifact.

Table 8: Final topologies and results for stress minimization of cantilever beam.

ΔT	0	5	10
Final topology			
v_{final}	0.42	0.38	0.44
J_{final}	$2.47J_0$	$2.85J_0$	$2.55J_0$
σ_{final}	$1.43\sigma_0$	$1.49\sigma_0$	$1.48\sigma_0$

The main contribution of the chapter is a new method for stress constrained topology optimization of thermo-elastic problems. Two different formulations were presented and compared. Both formulations exploit the concept of topological sensitivity; thus material parameterization is not required.

As the numerical experiments reveal, the impact of small temperature variations on the final topologies can be significant for certain problems, and minimal for other problems. Future work will focus on including other constraints including buckling and eigen-modes.

5. AUGMENTED TOPOLOGICAL LEVEL-SET METHOD

The objective of this chapter is to introduce and demonstrate a robust method for multi-constrained topology optimization. The method is derived by combining the topological sensitivity with the classic augmented Lagrangian formulation.

The primary advantages of the proposed method are: (1) it rests on well-established augmented Lagrangian formulation for constrained optimization, (2) the augmented topological level-set can be derived systematically for an arbitrary set of loads and constraints, and (3) the level-set can be updated efficiently. The method is illustrated through numerical experiments.

5.1 Multi-Constrained Topology Optimization

A typical single-load topology optimization problem in structural mechanics may be posed as (see Figure 15):

$$\begin{aligned}
 & \underset{\Omega \subset D}{\text{Min}} \varphi(u, \Omega) \\
 & g_i(u, \Omega) \leq 0; i = 1, 2, \dots, m \\
 & \text{subject to} \\
 & Ku = f
 \end{aligned} \tag{34}$$

where:

D : Domain within which the topology must lie

f : External force vector

g_i : Constraints

K : Finite element stiffness matrix

m : Number of constraints

u : Finite element displacement field

φ : Objective to be minimized

Ω : Topology to be computed

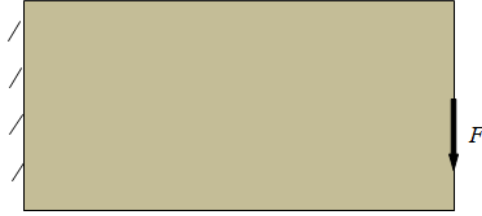


Figure 15: A single-load structural problem.

A classic example is compliance minimization:

$$\begin{aligned}
 & \underset{\Omega \subset D}{\text{Min}} J = f^T u \\
 & |\Omega| - v_0 \leq 0 \\
 & \text{subject to} \\
 & Ku = f
 \end{aligned} \tag{35}$$

Similarly, a *stress-constrained* volume-minimization problem [54], [16] (with additional compliance constraint to avoid pathological conditions) may be posed as:

$$\begin{aligned}
 & \underset{\Omega \subset D}{\text{Min}} |\Omega| \\
 & \sigma \leq \sigma_{\max} \text{ in } \Omega \\
 & J \leq J_{\max} \\
 & \text{subject to} \\
 & Ku = f
 \end{aligned} \tag{36}$$

where:

- J : Compliance
- J_{\max} : Max. compliance allowed
- σ : von Mises Stress
- σ_{\max} : Max. allowable von Mises Stress
- Ω : Topology to be computed

A multi-constrained multi-load problem on the other hand, may be posed as (see Figure 16 for an example of a two-load problem):

$$\begin{aligned}
& \underset{\Omega \subset D}{\text{Min}} \varphi(u_1, u_2, \dots, u_N, \Omega) \\
& g_i(u_1, u_2, \dots, u_N, \Omega) \leq 0; i = 1, 2, \dots, m \\
& \text{subject to} \\
& Ku_n = f_n; n = 1, 2, \dots, N
\end{aligned} \tag{37}$$

where:

f_n : External force vector for load-n

N : Number of loads

u_n : Displacement field for load-n

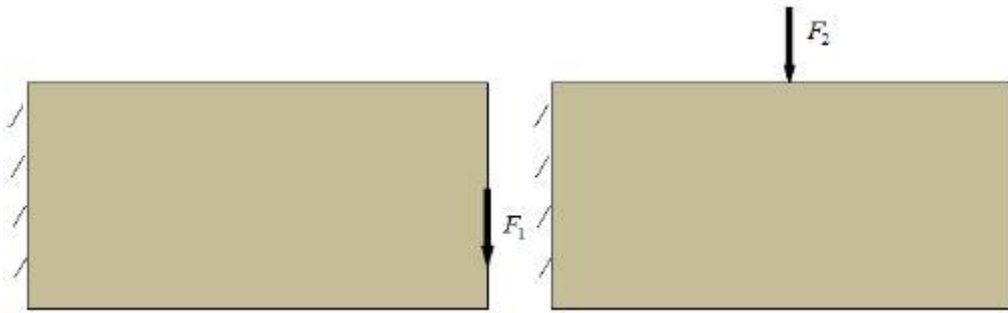


Figure 16: A multi-load structural problem.

While various methods have been proposed to solve specific instances of single and multi-constrained problems (see Section 2 for a review), the objective of this chapter is to develop a unified method that is applicable to all flavors of multi-constrained problems.

The proposed method relies on the concepts of topological level-set [74], [109], [111], [114], [115] and augmented Lagrangian [49], and it overcomes the deficiencies of existing methods discussed next.

5.2 Augmented Lagrangian Method

Towards this end, consider the classic *continuous-variable* constrained optimization problem:

$$\begin{aligned} & \underset{x}{\text{Min}} f(x) \\ & g_i(x) \leq 0 \end{aligned} \quad (38)$$

Observe that this is a continuous variable problem involving a continuous variable x opposed to a topology optimization problem. One of the most popular methods for solving such problems is the *augmented Lagrangian method*, also referred to as the “Method of Multipliers” [49]. Since the augmented Lagrangian method is well established, we only provide a brief summary of the method.

In this method, the objective and the constraints are combined into a single unconstrained function, referred to as the augmented Lagrangian:

$$L(x, \mu, \gamma) = f(x) - \sum_{i=1}^m \bar{L}_i(x, \mu, \gamma) \quad (39)$$

In the above equation, $\bar{L}_i(x, \mu, \gamma)$ is defined as [116]:

$$\bar{L}_i(x, \mu, \gamma) = \begin{cases} \mu_i g_i(x) - \frac{1}{2} \gamma_i (g_i(x))^2 & \mu_i - \gamma_i g_i(x) > 0 \\ \frac{1}{2} \mu_i^2 / \gamma_i & \mu_i - \gamma_i g_i(x) \leq 0 \end{cases} \quad (40)$$

where μ_i are the Lagrangian multipliers and γ_i are the penalty parameters.

Note that the gradient of the augmented Lagrangian is given by:

$$\nabla L(x, \mu, \gamma) = \nabla f - \sum_{i=1}^m \nabla \bar{L}_i(x, \mu, \gamma) \quad (41)$$

Where

$$\nabla \bar{L}_i(x, \mu, \gamma) = \begin{cases} (\mu_i - \gamma_i g_i) \nabla g_i & \mu_i - \sigma_i g_i(x) > 0 \\ 0 & \mu_i - \sigma_i g_i(x) \leq 0 \end{cases} \quad (42)$$

The Lagrangian multipliers and penalty parameters are initialized to an arbitrary set of positive values. Then, the Lagrangian in Equation (39) is minimized, typically via nonlinear conjugate gradient. Once the minimization terminates, the Lagrangian multipliers are updated as follows [116]:

$$\mu_i^{k+1} = \max\{\mu_i^k - g_i(\hat{x}^k), 0\}, i = 1, 2, 3, \dots, m \quad (43)$$

where the \hat{x}^k is the minimum at the (current) k iteration. The penalty parameters are also updated:

$$\gamma_i^{k+1} = \begin{cases} \gamma_i^k & \min(g_i^{k+1}, 0) \leq \zeta \min(g_i^k, 0) \\ \max(\eta \gamma_i^k, k^2) & \min(g_i^{k+1}, 0) > \zeta \min(g_i^k, 0) \end{cases} \quad (44)$$

where $0 < \zeta < 1$ and $\eta > 0$; typically $\zeta = 0.25$ and $\eta = 10$. The updates ensure rapid minimization of the objective, while satisfying the constraints. In the following iterations, the augmented Lagrangian in Equation (39) is once again minimized with the updated values. The cycle is repeated until the objective cannot be reduced further. The implementation details and the robustness of the algorithm are discussed, for example, in [116].

5.3 Augmented Topological Level-Set

Now consider the topology optimization problem:

$$\begin{aligned} & \underset{\Omega \subset D}{\text{Min}} \varphi \\ & g_i(u, \Omega) \leq 0 \end{aligned} \quad (45)$$

The objective is to extend the classic augmented Lagrangian method to solve the above problem. Drawing an analogy between Equations (38) and Equation (45), we define the *topological augmented Lagrangian* as follows:

$$L(u, \Omega; \gamma_i, \mu_i) \equiv \varphi - \sum_{i=1}^m \bar{L}_i(u, \Omega; \gamma_i, \mu_i) \quad (46)$$

Where

$$\bar{L}_i(u, \Omega; \gamma_i, \mu_i) = \begin{cases} \mu_i g_i - \frac{1}{2} \gamma_i (g_i)^2 & \mu_i - \gamma_i g_i > 0 \\ \frac{1}{2} \mu_i^2 / \gamma_i & \mu_i - \gamma_i g_i \leq 0 \end{cases} \quad (47)$$

In classic continuous optimization, the gradient was defined with respect to the continuous variable x . Here, the gradient is defined with respect to a topological change. Drawing an analogy to the gradient operator in Equation (41), we propose the following *topological gradient operator*:

$$\mathcal{T}_\Omega[L(u, \Omega; \gamma_i, \mu_i)] \equiv \mathcal{T}_L = \mathcal{T}_\varphi - \sum_{i=1}^m \mathcal{T}_{\bar{L}_i} \quad (48)$$

where \mathcal{T}_φ is the topological level-set associated with the objective, and

$$\mathcal{T}_{\bar{L}_i} = \begin{cases} (\mu_i - \gamma_i g_i) \mathcal{T}_{g_i} & \mu_i - \gamma_i g_i > 0 \\ 0 & \mu_i - \gamma_i g_i \leq 0 \end{cases} \quad (49)$$

where

$$\mathcal{T}_{g_i} \equiv \mathcal{T}(g_i) \quad (50)$$

are the topological level-sets associated with each of the constraint functions. Observe that we have essentially combined various topological level-sets into a single topological level. The multipliers and penalty parameters are updated as described earlier.

The above concept easily generalizes to multi-load constrained topology optimization problem:

$$\begin{aligned} & \underset{\Omega \subset D}{\text{Min}} \varphi(u_1, u_2, \dots, u_N, \Omega) \\ & g_i(u_1, u_2, \dots, u_N, \Omega) \leq 0; i = 1, 2, \dots, I \end{aligned} \quad (51)$$

in that the augmented Lagrangian is now defined as:

$$L \equiv \varphi - \sum_{i=1}^m \bar{L}_i(u_1, u_2, \dots, u_N, \Omega; \gamma_i, \mu_i) \quad (52)$$

Thus, the only difference is that the constraint and objective depend on multiple displacement fields.

5.4 Illustrative Examples

Before we discuss implementation details, a few examples are provided to illustrate the concept of the augmented topological level-set.

Displacement Constraint at a Point

Consider the single-load problem posed in Figure 17, where a y-displacement constraint is imposed at point q :

$$\begin{aligned} & \underset{\Omega \subset D}{\text{Min}} |\Omega| \\ & u_y(q) - \delta_{\max} \leq 0 \end{aligned} \quad (53)$$

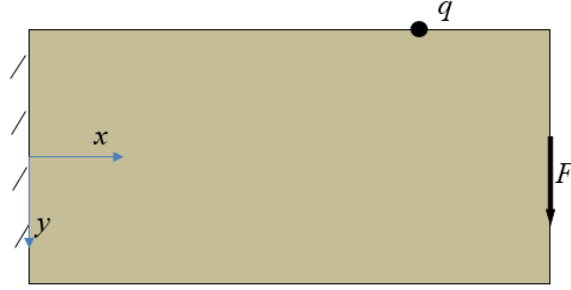


Figure 17: A single-load problem with displacement constraint.

First consider the objective function. It is true that:

$$\mathcal{T}_\varphi \equiv \lim_{r \rightarrow 0} \frac{|\Omega_r| - |\Omega|}{\pi r^2} = \lim_{r \rightarrow 0} \frac{-\pi r^2}{\pi r^2} = -1 \quad (54)$$

Next consider the displacement constraint. Since the point of interest does not coincide with the point of force-application, we first pose an adjoint problem:

$$K\lambda = -\hat{\delta}(q) \quad (55)$$

where $\hat{\delta}(q)$ is the Dirac delta function at point q . Specifically, we have:

$$\nabla_u (u_y(q) - \delta_{\max}) = \nabla_u (u_y(q)) = \hat{\delta}(q) \quad (56)$$

In other words, as expected, one must apply a negative unit force at point q and solve for the adjoint. Once the adjoint is obtained, the topological sensitivity of the constraint is obtained as usual via:

$$\mathcal{T}_g = -\frac{4}{1+\nu} \sigma(u) : \varepsilon(\lambda) + \frac{1-3\nu}{1-\nu^2} \text{tr}[\sigma(u)] \text{tr}[\varepsilon(\lambda)] \quad (57)$$

Therefore, the combined topological level-set is given by:

$$\mathcal{T}_L = -1 - \mathcal{T}_{\bar{L}} \quad (58)$$

Where

$$\mathcal{T}_{\bar{L}} = \begin{cases} (\mu - \gamma g) \mathcal{T}_g & \mu - \gamma g > 0 \\ 0 & \mu - \gamma g \leq 0 \end{cases} \quad (59)$$

Global p-norm Stress Constraint

Now consider a global stress constraint:

$$\begin{aligned} & \underset{\Omega \subset D}{Min} |\Omega| \\ & \sigma - \sigma_{\max} \leq 0 \end{aligned} \quad (60)$$

where the global stress is defined by weighting the von Mises stresses over all elements via the popular p-norm:

$$\sigma = \left(\sum_e (\sigma_e)^p \right)^{1/p} \quad (61)$$

Computing the adjoint and the gradient of this global constraint is described in [74]. Once the adjoint has been computed, the topological level-set is defined as in Equation (57), followed by the augmented level-set as in Equation (58).

Multi-load Displacement Constraint

As an example of a multi-load problem, consider Figure 18, where the objective is to minimize volume such that the y-displacement at point q does not exceed a prescribed value under two different load conditions, i.e.,

$$\begin{aligned}
& \underset{\Omega \subset D}{\text{Min}} |\Omega| \\
& u_{1y}(q) - \delta_{\max} \leq 0 \\
& u_{2y}(q) - \delta_{\max} \leq 0
\end{aligned} \tag{62}$$

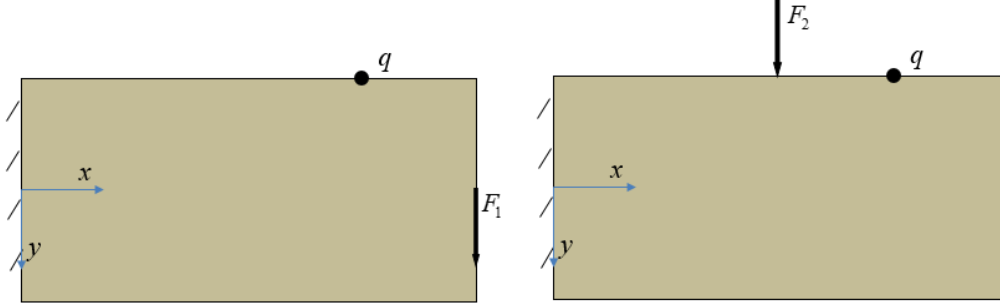


Figure 18: A multi-load problem with displacement constraint.

Three different topological sensitivity fields must be computed. As before, the field associated with the objective is:

$$\mathcal{T}_\varphi = -1 \tag{63}$$

Next, since the constraint is applied at point q , a unit load is used to construct a *single adjoint field* per Equation (55). Given the two displacements fields and the adjoint fields, the remaining two topological sensitivity fields are computed as follows:

$$\mathcal{T}_{g_1} = -\frac{4}{1+\nu} \sigma(u_1) : \varepsilon(\lambda) + \frac{1-3\nu}{1-\nu^2} \text{tr}[\sigma(u_1)] \text{tr}[\varepsilon(\lambda)] \tag{64}$$

$$\mathcal{T}_{g_2} = -\frac{4}{1+\nu} \sigma(u_2) : \varepsilon(\lambda) + \frac{1-3\nu}{1-\nu^2} \text{tr}[\sigma(u_2)] \text{tr}[\varepsilon(\lambda)] \tag{65}$$

5.5 Algorithm of Augmented Topological Level-Set

The overall algorithm is illustrated in Figure 19, and described below:

- 1) The domain, desired volume fraction, multipliers and penalty parameters are initialized as described earlier.
- 2) Multiple FEA are performed depending on the number of loads and adjoint problems.
- 3) The constraints are evaluated, and the multipliers and penalty parameters are updated; the constraints are normalized to unity for numerical robustness.
- 4) If the constraints are not satisfied, the volume decrement is decremented, and the algorithm returns to step-2.
- 5) If the constraints are satisfied, the topological sensitivity fields for the objective and constraints are computed, and normalized to unity.
- 6) The iso-surface is extracted using the augmented topological level-set \mathcal{T}_L
- 7) The topology is assumed to have converged if the compliance of the structure has converged to within 1%.

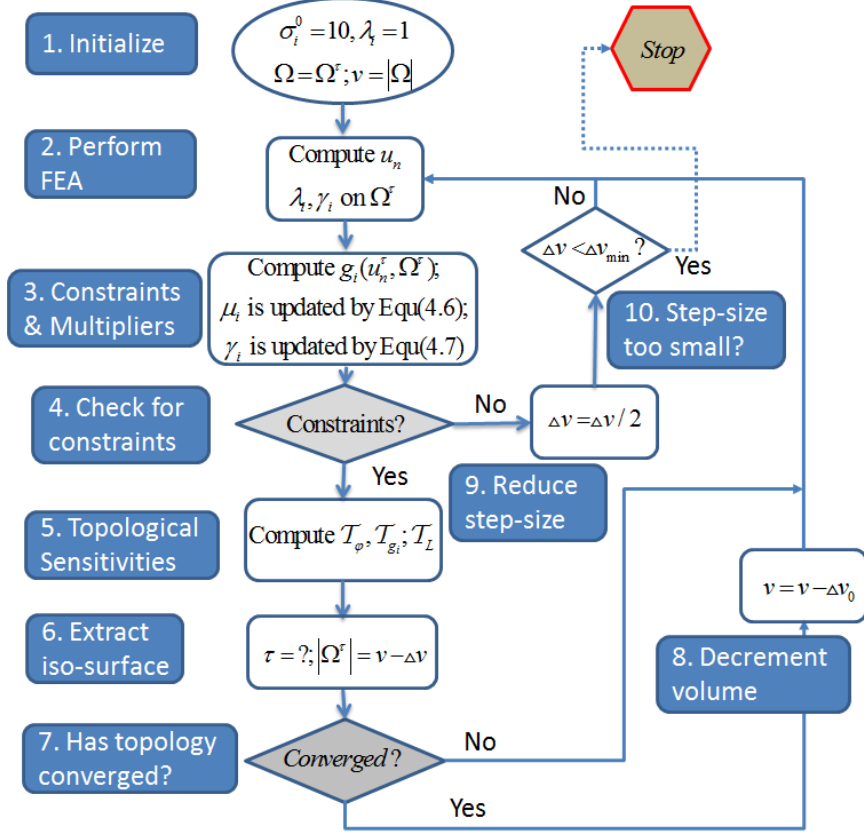


Figure 19: Proposed algorithm

5.6 Numerical Experiments

In this section, we demonstrate the proposed method through numerical experiments. The default material properties are $E = 2 * 10^{11}$ and $\nu = 0.33$. All experiments were conducted on a Windows 7 64-bit machine with the following hardware: Intel I7 960 CPU quad-core running at 3.2GHz with 6 GB of memory.

All constraints are relative to the initial displacement and stresses, prior to optimization.

Thus, a constraint:

$$u_y(q) - 3.0 \leq 0 \quad (66)$$

implies that the vertical displacement at point q must not exceed three times the initial displacement at that point, prior to optimization. The constraint:

$$\sigma - 2.0 \leq 0 \quad (67)$$

implies that the maximum von Mises stress must not exceed twice the maximum von Mises stress prior to optimization.

5.6.1 Cantilever Beam: Displacement Constraints

The first experiment involves the classic 2-D cantilever beam illustrated in Figure 20. A point of interest ‘ q ’ is located in the middle of the top edge. The problem is:

$$\begin{aligned} & \underset{\Omega \subset D}{\text{Min}} |\Omega| \\ & u_y(q) - \delta_q^{\max} \leq 0 \\ & u_y(a) - \delta_a^{\max} \leq 0 \end{aligned} \quad (68)$$

Thus, a displacement constraint is placed at the point-of-force application ‘ a ’, and a secondary point-of-interest ‘ q ’.

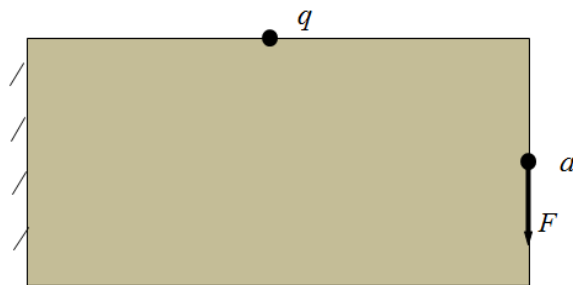





Figure 20: A single load cantilever beam problem with a displacement constraint

Specific values for the allowable relative displacements at both points of interest are specified in Table 9. For FEA, the domain was discretized into 2000 elements.

The final volume fractions, the actual relative displacements reached, and the final topologies are also illustrated in Table 9. Observe that, at least one of the constraints is active (illustrated with a ‘box’) at termination.

Table 9: Constraints and results for problem in Figure 20

Constraints	Final Volume Fraction	Final displacements	Final Topologies
$\delta_a^{\max} = 10.00$ $\delta_q^{\max} = 1.50$	0.48	$\delta_a^{\text{result}} = 1.75$ $\delta_q^{\text{result}} = 1.50$	
$\delta_a^{\max} = 1.50$ $\delta_q^{\max} = 10.00$	0.55	$\delta_a^{\text{result}} = 1.50$ $\delta_q^{\text{result}} = 1.63$	
$\delta_a^{\max} = 1.50$ $\delta_q^{\max} = 1.50$	0.56	$\delta_a^{\text{result}} = 1.50$ $\delta_q^{\text{result}} = 1.40$	

5.6.2 Cantilever Beam: Multi-load

We now consider a multi-load problem illustrated in Figure 21. The displacement constraint for each load is placed at the point of force application, i.e., the problem is:

$$\begin{aligned}
 & \text{Min}_{\Omega \subset D} |\Omega| \\
 & u_{1,y} - \delta_1^{\max} \leq 0 \\
 & u_{2,y} - \delta_2^{\max} \leq 0
 \end{aligned} \tag{69}$$

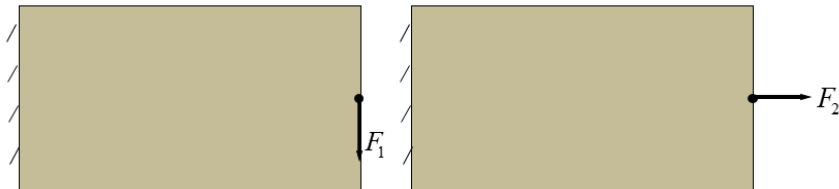





Figure 21: A multi-load cantilever beam problem.

The specific constraints and the final results are summarized in Table 10. Observe that the final topology is strongly dependent on the constraints.

Table 10: Constraints and results for problem in Figure 21

Constraints	Final Volume Fraction	Final displacements	Final Topologies
$\delta_1^{\max} = 1.50$ $\delta_2^{\max} = 50.00$	0.59	$\delta_1^{\text{result}} = 1.50$ $\delta_2^{\text{result}} = 1.47$	
$\delta_1^{\max} = 50.0$ $\delta_2^{\max} = 1.50$	0.48	$\delta_1^{\text{result}} = 5.87$ $\delta_2^{\text{result}} = 1.50$	
$\delta_1^{\max} = 1.50$ $\delta_2^{\max} = 1.50$	0.62	$\delta_1^{\text{result}} = 1.50$ $\delta_2^{\text{result}} = 1.36$	

5.6.3 L-bracket: Displacement & Stress Constraints

We now consider a displacement (at the point of force application) and global stress constrained problem over an L-bracket (see Figure 22):

$$\begin{aligned}
 & \underset{\Omega \subset D}{\text{Min}} |\Omega| \\
 & u_y - \delta^{\max} \leq 0 \\
 & \sigma - \sigma^{\max} \leq 0
 \end{aligned} \tag{70}$$

The domain is discretized using 2000 finite elements.

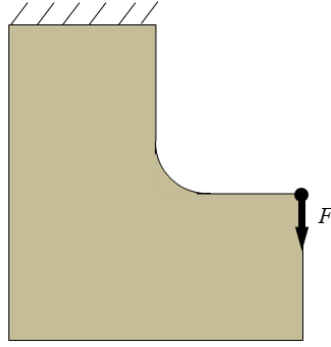


Figure 22: A single-load L-bracket problem with global stress constraint.

The specific constraints and the final results are summarized in Table 11. If the displacement constraint is active, then the topology corresponds to the classic ‘compliance-minimization’ problem, and if the stress constraint is active, the topology corresponds to the stress constraint problem [113].

Table 11: Constraints and results for problem in Figure 22.

Constraints	Final Volume Fraction	Final displacements	Final Topologies
$\delta^{\max} = 1000$ $\sigma^{\max} = 1.5$	0.35	$\delta_j^{result} = 2.49$ $\sigma^{result} = 1.50$	
$\delta^{\max} = 1.5$ $\sigma^{\max} = 1000$	0.49	$\delta^{result} = 1.50$ $\sigma^{result} = 1.14$	
$\delta^{\max} = 1.5$ $\sigma^{\max} = 1.1$	0.53	$\delta^{result} = 1.48$ $\sigma^{result} = 1.09$	

5.6.4 L-bracket: Multi-load, Multi-Constraint

In this experiment, we consider the multi-load structure in Figure 23, where the topology optimization problem is

$$\begin{aligned}
 & \underset{\Omega \subset D}{\text{Min}} |\Omega| \\
 & u_{1,y} - \delta_1^{\max} \leq 0 \\
 & \sigma_1 - \sigma_1^{\max} \leq 0 \\
 & u_{2,x} - \delta_2^{\max} \leq 0 \\
 & \sigma_2 - \sigma_2^{\max} \leq 0
 \end{aligned} \tag{71}$$

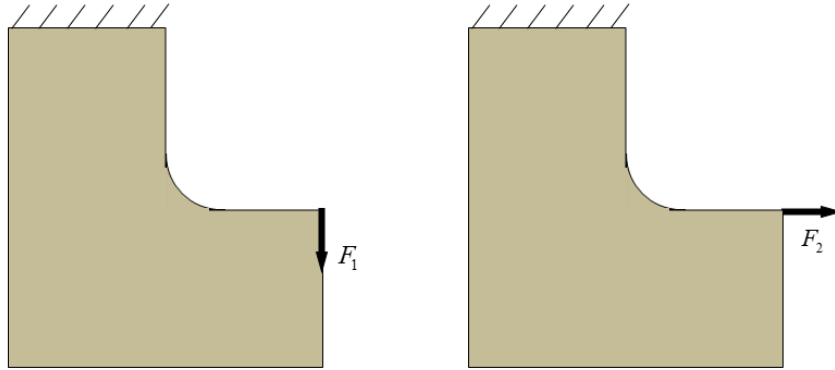







Figure 23: A multi-load L-bracket problem.

The results are summarized in Table 12; once again, the topologies are consistent with previous results.

Table 12: Constraints & results for problem in Figure 23

Constraints	Final displacements	Final Topologies
$\delta_1^{\max} = 1.5$ $\delta_2^{\max} = 10000$ $\sigma_1^{\max} = 10000$ $\sigma_2^{\max} = 10000$	$\delta_1^{\text{result}} = 1.50$ $\delta_2^{\text{result}} = 5.05$ $\sigma_1^{\text{result}} = 1.14$ $\sigma_2^{\text{result}} = 2.85$	 $V=0.50$
$\delta_1^{\max} = 10000$ $\delta_2^{\max} = 1.5$ $\sigma_1^{\max} = 10000$ $\sigma_2^{\max} = 10000$	$\delta_1^{\text{result}} = 25.30$ $\delta_2^{\text{result}} = 1.50$ $\sigma_1^{\text{result}} = 11.22$ $\sigma_2^{\text{result}} = 1.29$	 $V=0.33$

$\delta_1^{\max} = 10000$ $\delta_2^{\max} = 10000$ $\sigma_1^{\max} = 1.5$ $\sigma_2^{\max} = 10000$	$\delta_1^{\text{result}} = 2.54$ $\delta_2^{\text{result}} = 22.99$ $\sigma_1^{\text{result}} = 1.50$ $\sigma_2^{\text{result}} = 5.40$	 V=0.37
$\delta_1^{\max} = 10000$ $\delta_2^{\max} = 10000$ $\sigma_1^{\max} = 10000$ $\sigma_2^{\max} = 1.5$	$\delta_1^{\text{result}} = 72.04$ $\delta_2^{\text{result}} = 2.42$ $\sigma_1^{\text{result}} = 16.96$ $\sigma_2^{\text{result}} = 1.50$	 V=0.25
$\delta_1^{\max} = 1.50$ $\delta_2^{\max} = 1.50$ $\sigma_1^{\max} = 1.50$ $\sigma_2^{\max} = 1.50$	$\delta_1^{\text{result}} = 1.49$ $\delta_2^{\text{result}} = 1.50$ $\sigma_1^{\text{result}} = 1.13$ $\sigma_2^{\text{result}} = 1.26$	 V=0.58

5.6.5 Mitchell Bridge: Multi-load, Multi-Constraint

We now solve the problem posed in Equation (71) over the classic Mitchell bridge structure in Figure 24. The results are summarized in Table 13.

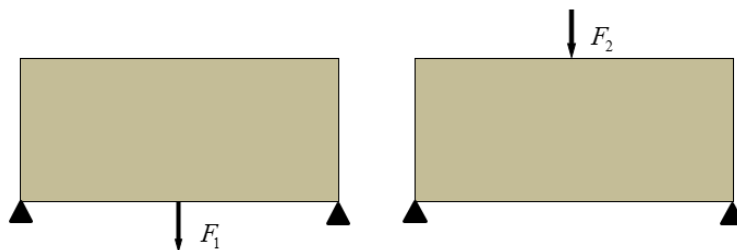







Figure 24: A multi-load Mitchell bridge problem.

Table 13: Constraints & results for problem in Figure 24

Constraints	Final displacements	Final Topologies
-------------	---------------------	------------------

$\delta_1^{\max} = 1.50$ $\delta_2^{\max} = 10.00$ $\sigma_1^{\max} = 10.00$ $\sigma_2^{\max} = 10.00$	$\delta_1^{result} = 1.50$ $\delta_2^{result} = 1.32$ $\sigma_1^{result} = 1.04$ $\sigma_2^{result} = 1.03$	 V=0.51
$\delta_1^{\max} = 10.00$ $\delta_2^{\max} = 1.50$ $\sigma_1^{\max} = 10.00$ $\sigma_2^{\max} = 10.00$	$\delta_1^{result} = 2.77$ $\delta_2^{result} = 1.50$ $\sigma_1^{result} = 1.89$ $\sigma_2^{result} = 1.09$	 V=0.40
$\delta_1^{\max} = 10.00$ $\delta_2^{\max} = 10.00$ $\sigma_1^{\max} = 1.50$ $\sigma_2^{\max} = 10.00$	$\delta_1^{result} = 4.12$ $\delta_2^{result} = 3.18$ $\sigma_1^{result} = 1.50$ $\sigma_2^{result} = 1.22$	 V=0.21
$\delta_1^{\max} = 10.00$ $\delta_2^{\max} = 10.00$ $\sigma_1^{\max} = 10.00$ $\sigma_2^{\max} = 1.50$	$\delta_1^{result} = 5.68$ $\delta_2^{result} = 4.15$ $\sigma_1^{result} = 2.05$ $\sigma_2^{result} = 1.47$	 V=0.16
$\delta_1^{\max} = 1.50$ $\delta_2^{\max} = 1.50$ $\sigma_1^{\max} = 1.50$ $\sigma_2^{\max} = 1.50$	$\delta_1^{result} = 1.50$ $\delta_2^{result} = 1.36$ $\sigma_1^{result} = 1.03$ $\sigma_2^{result} = 1.01$	 V=0.51

In this chapter, a new method for multi-loaded, multi-constrained topology optimization is proposed, where the topological sensitivity field for each loading condition and constraint is calculated, and then combined via classic augmented Lagrangian methods. This is embedded in the Pareto algorithm to generate a set of Pareto-optimal topologies. As illustrated via numerical

examples, the proposed method not only generates topologies consistent with those published in the literature, but provides solutions to more complex problems that have not been considered before.

6. LARGE-SCALE CONSTRAINED TOPOLOGY OPTIMIZATION

The objective of this chapter is to introduce and demonstrate a robust methodology for solving multi-constrained 3D topology optimization problems. The proposed methodology is a combination of the topological level-set formulation, augmented Lagrangian algorithm, and assembly-free deflated finite element analysis (FEA).

The salient features of the proposed method include: (1) it exploits the topological sensitivity fields that can be derived for a variety of constraints, (2) it rests on well-established augmented Lagrangian formulation to solve constrained problems, and (3) it overcomes the computational challenges by employing assembly-free deflated FEA. The proposed method is illustrated through several 3D numerical experiments.

6.1 Literature Review of Large-scale Topology Optimization

In [117], the authors noted that in SIMP, as the density drops to zero, the underlying linear system becomes ill-conditioned, and iterative solvers such as conjugate gradient or MINRES perform poorly. Consequently, topology optimization of 3-D problems (where iterative solvers are essential) consume a significant amount of time. In [118] problems with 1~3 million degrees of freedom were optimized in 3~40 hours (depending on the specific problem) on a Cray T3E super computer. In [117], using specialized Krylov recycling methods, problems with about 1 million degrees of freedom was optimized in 45 hours on a regular desktop. In [119], using approximate reanalysis, a speed-up of 3~5 was achieved (compared to standard implementation). In [120], the authors exploited graphics processing unit (GPU), and solved ‘box-like’ design spaces problem with 3 million degrees of freedom in about 2 hours. Using Optistruct (2013 release) [121], the benchmark problem posed in [117] was solved in 20 hours on a high-end server desktop.

All of the above problems are simple single-load unconstrained compliance-minimization problems. The challenges increase many-fold in practice.

For example, stress minimization problems are much harder to solve than compliance minimization problems [122], but arguably more important [123]. Numerous challenges arise in such problems; for example, stress singularity [124], and consistent agglomeration of point-wise stress constraints [125].

In multi-load topology optimization, not only must one solve dozens of finite element problems at each step of the optimization, chances of disconnected topologies increase significantly [126].

In multi-objective optimization, the notion of pareto-optimal topologies arises that represent a compromise between potentially conflicting objectives [127]; such problems require careful treatment, and significantly more computation [128].

Finally, constraints cannot be neglected during optimization; while several methods have been proposed for handling constraints in topology optimization [129], the theoretical, computational and robustness challenges have not been fully resolved.

The evolutionary and level-set methods face their own set of challenges [92].

From the above literature review, one can conclude that significant progress has been made in recent years on constrained topology optimization. Yet, a single method that can handle a variety of constraints, especially in 3D, has not been reported.

In this chapter, we extend the 2D method proposed in [130] to achieve this goal; the main contributions of this chapter are:

- The topological level-set in 3D is combined with the augmented Lagrangian method. The 3D computational challenges are addressed by exploiting the assembly-free deflated FEA [122].
- While only displacement and stress constraints were addressed in [130], additional buckling and Eigen-value constraints, are included here. Inclusion of buckling and Eigen-value constraints necessitates the need for soft and hard constraints, discussed later in the chapter.
- Casting constraints are also addressed in this chapter.
- While single-load problems were considered in [130], multiple and multi-load problems are considered here.

6.2 Formulation of Large-Scale Topology Optimization

A practical challenge that arises in solving large-scale topology optimization is the computational costs rising from underlying FEA. To address the computational cost, we rely here on the assembly-free deflated conjugate gradient (AF-DCG) method proposed in [131]. The AF-DCG is a combination of three distinct but complimentary concepts: assembly-free, voxelization and deflation method. In this section, the three fundamental components are reviewed briefly.

6.2.2 Assembly-Free FEA

In classic FEA, the global stiffness matrix is assembled before solved as shown in Figure 71.

$$Ku = \left(\sum_e K_e \right) u \quad (72)$$

The computational bottleneck under modern computer architect is data transportation between CUP and memory. For a large scale problem, the size of an assembled global stiffness matrix can be up to millions of degrees of freedom. Frequent transportation of the assembled stiffness matrix seriously slows down FEA speed.

To overcome the deficiency, the assembly-free (or matrix-free) approach [131] is adopted, where neither the global stiffness matrix K is assembled or stored. Instead, the fundamental matrix operations are carried out on element level as shown in Equation (73).

$$Ku = \sum_e (K_e u_e) \quad (73)$$

In other words, instead of assembly, an elemental level of matrix multiplication between element stiffness matrix K_e and displacement u_e is performed and the multiplication result vector is then assembled.

The assembly-free technique is more advantageous if (1) fewer element types are used, and element congruency and voxelization are explored; (2) deflated method is used to accelerate underlying iterative solvers.

6.2.2 Element Congruency and Mesh Voxelization

Two elements with the same number of DOF are said to be congruent within a specified tolerance ε if:

$$\frac{\|K_{e2} - K_{e1}\|}{\|K_{e1}\|} \leq \varepsilon$$

Where

K_e is element stiffness

(74)

For isotropic elements, the element-congruency can also be decided by comparing geometry. Congruent elements have identical element stiffness matrix. For assembly-free method, the solver only needs to compute and store distinct element stiffness matrix. By reducing memory fetching ‘footprint’, element-congruency can significantly accelerate computational speed.

Hexahedral elements (voxelization) are used for congruency in this research. For example, the bearing support in Figure 25 is meshed by congruent voxel elements with the same stiffness matrix. The most important benefits of adopting voxelization includes: (1) it is relatively easy for automatic mesh generator to create; (2) it significantly reduces memory foot-print and (3) when conjectured with mesh-free method and multi-core computer architecture, it significantly reduces finite element computational expense. Please refer to [131] for more details.

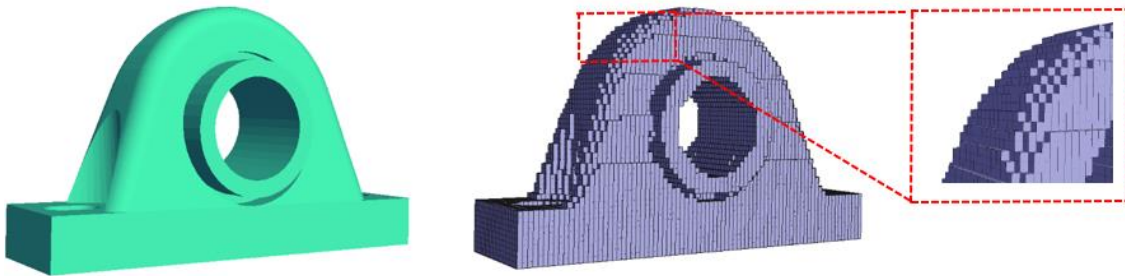


Figure 25: Bearing support CAD model and its voxelization mesh.

6.2.3 Deflated Method

The deflated method rests on the observation that the computational bottle-neck in modern architecture is memory access [132]. The AF-DCG computes the preconditioner and the solution to the underlying linear system in an assembly-free manner, significantly reducing memory bandwidth. Similarly, for modal analysis, an assembly-free modal analysis proposed in [133] is employed. Finally, for linear buckling analysis, the assembly-free extension of this method to buckling [134] is used.

6.2.4 Pareto in 3D

Integrated by AF-DCG, the Pareto method discussed in Chapter 3.3 can be easily generalized to 3D [97]; Figure 26, for example illustrates the Pareto-optimal for a 3D structural problem.

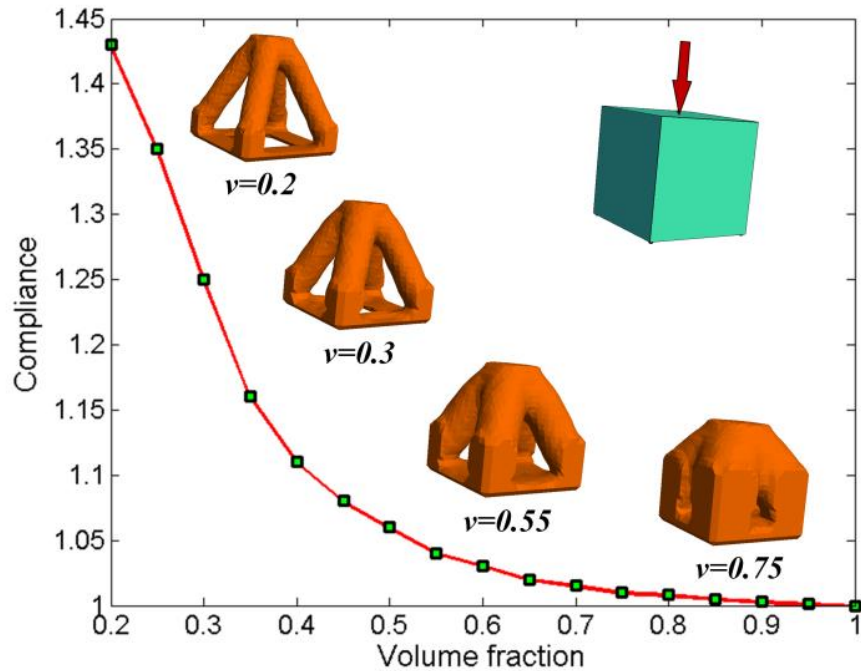


Figure 26: The Pareto-optimal curve and optimal topologies for a 3D structural problem.

6.3 Formulation of Constraints

6.3.1 Hard and Soft Constraints

In classic optimization [49], constraints are typically treated as ‘hard’ constraints, i.e., the algorithm will terminate if any of the constraints is violated. In design optimization, this can be too restrictive since design constraints may be unreasonable, and the algorithm may terminate without any solution.

Researchers have therefore developed algorithms for handling of soft constraints [135]: “*Hard constraints limit the feasible space, while soft constraints prioritize solutions within this space.*” Soft constraints are particularly useful in engineering [136] as an alternate to multi-objective problems.

In this study, we permit hard and soft constraints; for example:

$$\begin{aligned}
 & \underset{\Omega \subset D}{\text{Min}} \varphi \\
 & g_1(u, \Omega) \leq 0 \\
 & g_2(u, \Omega) \leq 0 \quad (\text{soft})
 \end{aligned} \tag{75}$$

The first constraint is hard, while the second constraint is treated as soft. Soft constraints influence the topology through the Lagrangian multiplier (see algorithm below), but do not influence the termination of the algorithm, i.e., do not influence the feasible space. Typically, compliance and stress are treated as hard constraints, while buckling and Eigen-value can be treated as either hard or soft constraints.

6.3.2 Casting Constraints

In addition to performance constraints, it is often important to include manufacturing constraints. For example, in [78] the authors proposed a projection method within a level-set formulation to impose thickness constraint for cast parts. Similarly, in [137], the authors imposed a density constraint, within the SIMP formulation, along the casting direction. This ensures that the density variable is non-decreasing along the casting direction (on either sides of the parting plane), preventing cavities in cast parts. In this chapter, we adopt this method to the topological level-set formulation; specifically, after a casting direction is selected, we impose a constraint on topological level-set to be non-decreasing along the casting direction to prevent cavities.

6.4 Algorithm of Large-Scale Constrained Topology Optimization

The four performance constraints considered here are compliance (J), p-norm Von Mises stress (σ), lowest Eigen-value (λ) and buckling load (P); soft constraints are identified, and casting constraints are optional.

The constraints are typically set relative to their initial values prior to optimization, and the objective is to minimize volume, i.e., the generic problem considered here is:

$$\begin{aligned}
 & \underset{\Omega \subset D}{\text{Min}} |\Omega| \\
 & J \leq (\alpha_1) J_0 \\
 & \sigma \leq (\alpha_2) \sigma_0 \\
 & P \geq (\alpha_3) P_0 \quad (\alpha_3 < 1) \\
 & \lambda \geq (\alpha_4) \lambda_0 \quad (\alpha_4 < 1) \\
 & P \geq (\alpha_5) P_0 \quad (\text{soft}) \\
 & \lambda \geq (\alpha_6) \lambda_0 \quad (\text{soft}) \\
 & Ku = f
 \end{aligned} \tag{76}$$

Thus a constraint:

$$J \leq 3J_0 \tag{77}$$

implies that the final compliance must not exceed three times the initial compliance. Similarly,

$$\sigma \leq 2\sigma_0 \tag{78}$$

implies that the final p-norm von Mises stress must not exceed twice the initial p-norm stress. On the other hand, the buckling and Eigen-value constraints may be hard or soft. For a soft constraint

$$P \geq 1.2P_0 \quad (\text{soft}) \tag{79}$$

the algorithm will attempt to find solutions (within the feasible space) that satisfy the above equation.

Observe that, if one imposes a hard constraint:

$$P \geq 1.2P_0 \quad (80)$$

the algorithm will terminate at the first iteration since the initial design will not satisfy this constraint!

The overall algorithm is illustrated in Figure 19, and it proceeds as follows:

- 1) The domain is discretized using hexahedral elements; the optimization parameters are initialized as $\mu = 100$ and $\gamma = 10$.
- 2) Depending on the constraint imposed, several FEAs are performed.
- 3) The constraints are evaluated, and the Lagrangian parameters are updated.
- 4) If any of the *hard* constraints are violated, the algorithm proceeds to step-9, else, it proceeds to step-5.
- 5) The topological sensitivity fields are computed, and the augmented topological level-set is extracted.
- 6) The topology for the current volume fraction is extracted.
- 7) If the topology has converged (i.e., if the change in compliance is less than 1%), proceed to step-8, else return to step-2.
- 8) Decrement the target-volume fraction $v = v - \Delta v$, and return to step-2.
- 9) Decrease the volume step-size Δv ; if the step-size is smaller than Δv_{\min} , terminate the algorithm, else return to step-2.

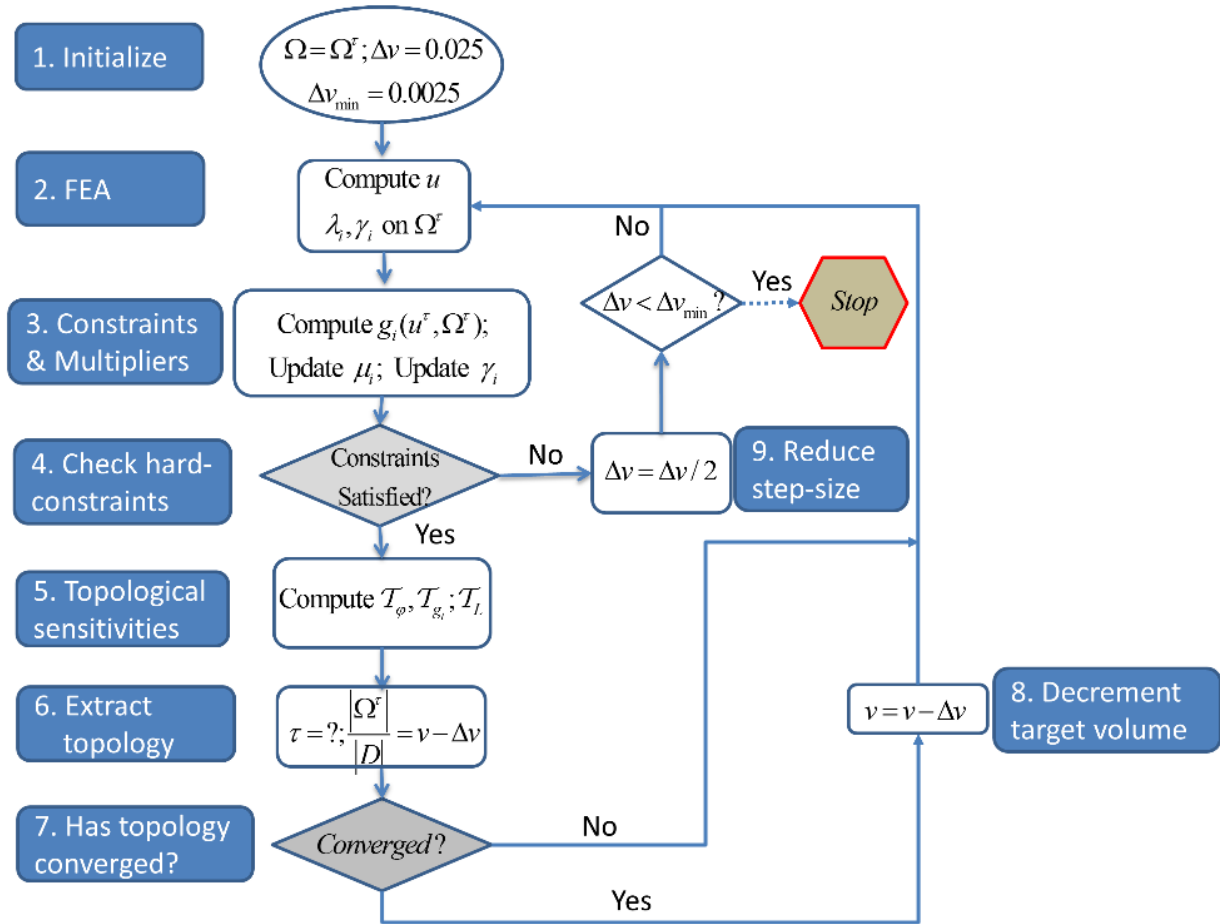


Figure 27: A multi-load Mitchell bridge problem.

6.5 Numerical Examples

In this section, numerical experiments are carried out to illustrate the above algorithm; the default parameters are:

- Material properties: $E = 2 * 10^{11}$ and $\nu = 0.3$
- All experiments were conducted using C++ on a Windows 7 64-bit machine with the following hardware: Intel I7 960 CPU quad-core running at 3.2GHz with 6 GB of memory.

6.5.1 L-bracket with Tip Load

The first experiment involves the L-bracket, whose cross-section is illustrated in Figure 28 (units in mm), with a thickness of 6 mm. In the topology optimization literature, it is common to use an L-bracket with a sharp reentrant corner [138]. This is perfectly acceptable for compliance dominated problems, but may not be desirable for stress-constrained problems due to the stress singularity at the reentrant corner. We have therefore added a small fillet to relieve the stress singularity. The L-bracket is fixed on the top edge, while a unit load is applied as illustrated. The domain is discretized with 24,330 elements, i.e., 90,738 degrees of freedom (DOF).

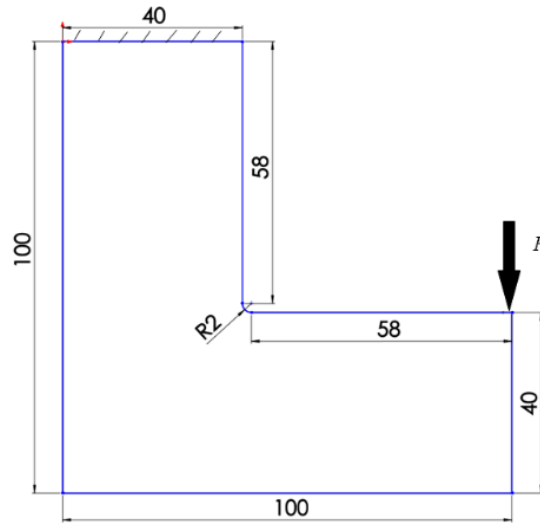


Figure 28: L-bracket cross-section.

The specific constrained topology optimization problem considered here is:

$$\begin{aligned}
 & \underset{\Omega \subset D}{\text{Min}} |\Omega| \\
 & J \leq (\alpha_1) J_0 \\
 & \sigma \leq (\alpha_2) \sigma_0
 \end{aligned} \tag{81}$$

Two scenarios are summarized in Table 10; the first scenario is compliance dominant, while the second is stress dominant. The final results, volume fractions and computing time are also summarized in Table 10. The active constraints are identified with a ‘box’.

Table 14: Constraints and results for problem in Figure 28.

Dominant Constraint	Initial Constraints	Final Results	Final volume & running time (s)
Compliance	$J \leq 2J_0$ $\sigma \leq 100\sigma_0$	$J = 2J_0$ $\sigma = 1.27\sigma_0$	$v = 0.34$ $t = 142.11$
Stress	$J \leq 100J_0$ $\sigma \leq 1.05\sigma_0$	$J = 1.75J_0$ $\sigma = 1.05\sigma_0$	$v = 0.47$ $t = 194.32$

The corresponding optimized topologies are illustrated in Figure 29. Observe that when compliance is dominant, the classic stiff design is obtained, whereas when stress is dominant, a strong design is obtained where the fillet radius is increased to reduce stress [113].

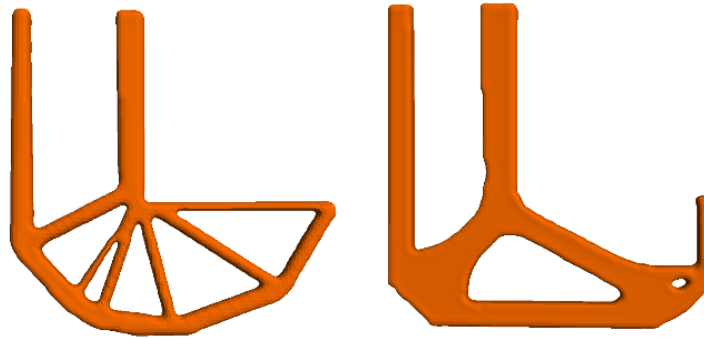


Figure 29: Final topologies which are subject to dominant constraints of compliance (left) and Von Mises stress (right).

Figure 30 illustrates the relative cost of various parts of the algorithm. As one can observe, significant portion (88%) of the time is spent on FEA, while the remaining 12% is spent on computing the topological sensitivity field, and other tasks. This is typical for all the numerical examples considered.

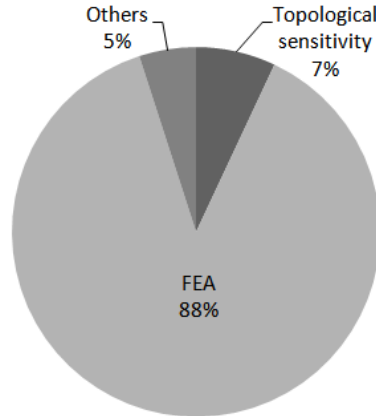


Figure 30: Computational cost for scenario-1 in Table 10.

6.5.2 Plate with Pressure Load

In the next example, we consider a plate geometry whose cross-section is illustrated in Figure 31 (units in mm); the thickness is 10 mm. The left face is fixed while a unit horizontal pressure is applied on the right face. The geometry is meshed with 50,560 hexahedral elements, i.e., 167,280 DOF.

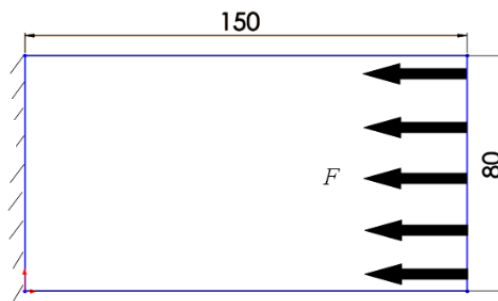


Figure 31: Thick plate dimensions with pressure loading.

The specific constrained topology optimization problem considered here is:

$$\begin{aligned}
 & \underset{\Omega \subset D}{\text{Min}} |\Omega| \\
 & J \leq (\alpha_1) J_0 \\
 & \sigma \leq (\alpha_2) \sigma_0 \\
 & P \geq (\alpha_3) P_0
 \end{aligned} \tag{82}$$

Three instances are summarized in Table 15; once again, the active final constraints are identified with a box. The execution time for the buckling-dominated problem is much longer due to the inherent computational complexity.

Table 15: Constraints and results for problem in Figure 31.

Dominant Constraint	Initial Constraints	Final Results	Final volume & running time (s)
Compliance	$J \leq 5J_0$ $\sigma \leq 100\sigma_0$ $P \geq 0.1P_0$	$J = 5J_0$ $\sigma = 2.39\sigma_0$ $P = 0.16P_0$	$v = 0.22$ $t = 342.63$
Stress	$J \leq 100J_0$ $\sigma \leq 2\sigma_0$ $P \geq 0.1P_0$	$J = 5.25J_0$ $\sigma = 2\sigma_0$ $P = 0.11P_0$	$v = 0.22$ $t = 401.09$
Buckling load	$J \leq 100J_0$ $\sigma \leq 100\sigma_0$ $P \geq 0.9P_0$	$J = 1.90J_0$ $\sigma = 1.73\sigma_0$ $P = 0.9P_0$	$v = 0.71$ $t = 234.34$

The corresponding topologies are illustrated in .Figure 32 As one can observe, the topologies for the first two cases are similar, and this is consistent with the results in Table 15. The topology for the buckling-dominated problem is, however, significantly different.

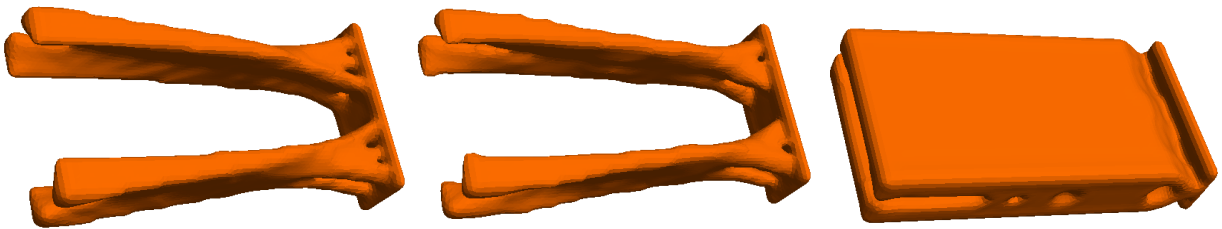


Figure 32: Final topologies for compliance dominated (top) stress dominated (left) and buckling-dominated (right).

In order to study the termination criterion, the iteration history for scenario-2 is illustrated in Figure 33 (the plot is to be interpreted from the right to left). Observe that the optimization starts with a volume decrement of 0.025, and it reduces when divergence is detected; the decrement

increases slightly towards the end. Most importantly, the volume decrement is well above the minimum value during optimization. Thus the termination is triggered by the hard stress constraint rather than due to the volume decrement constraint.

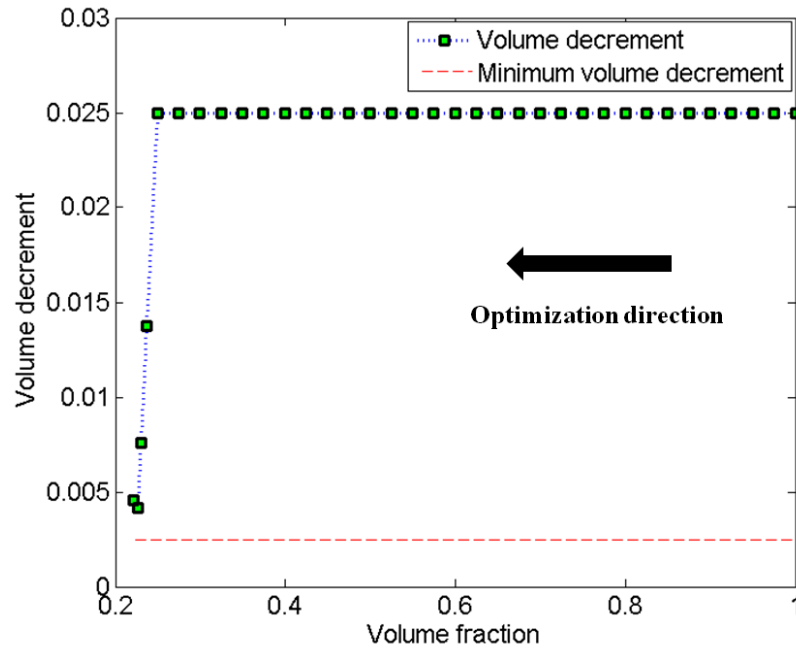


Figure 33: Iteration history of volume decrement for scenario-2 in Table 15.

For scenario-2 in Table 15, the relative constraints are illustrated in Figure 34 (the plots are to be interpreted from the right to left). The optimization terminates due to a relative stress constraint of 2.0 at a final volume fraction of 0.22.

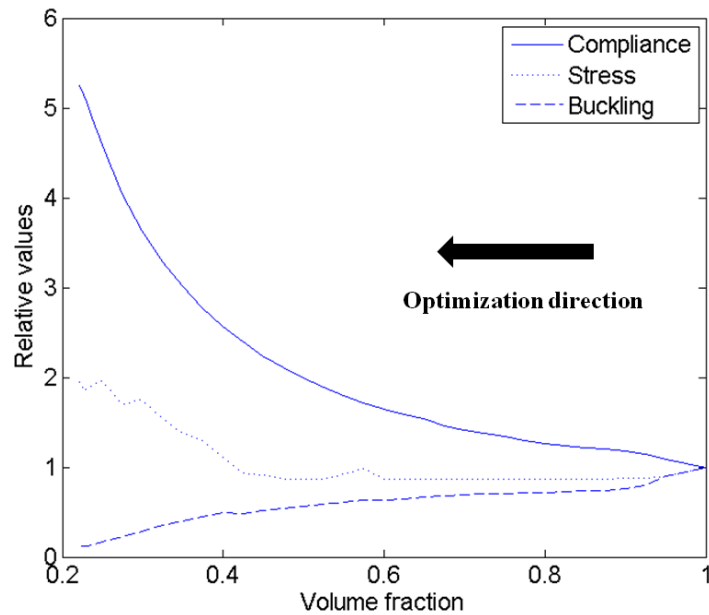
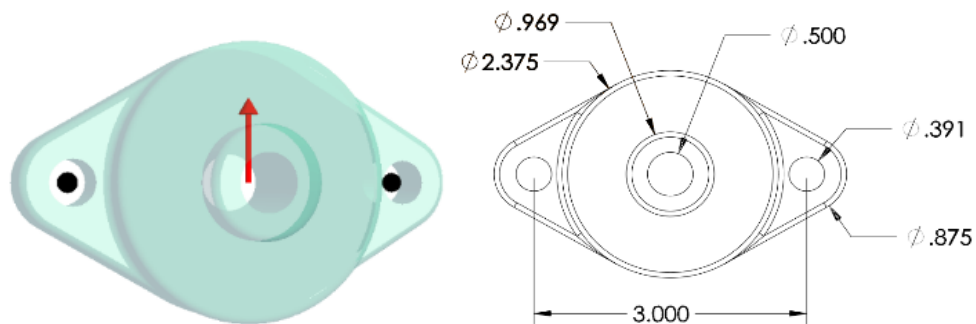


Figure 34: Constraint iteration history for scenario-2 in Table 15.

6.5.3 Case Study: Flange

This case study involves the flange illustrated in Figure 35; units are in inches. Flanges are commonly used, for example, to fasten pipes and rail-joints. The objective is to minimize the flange weight while subject to compliance, stress and Eigen-mode constraint. For FEA, 19,924 hexahedral elements are used to discretize the design domain, resulting in 63,666 DOF.



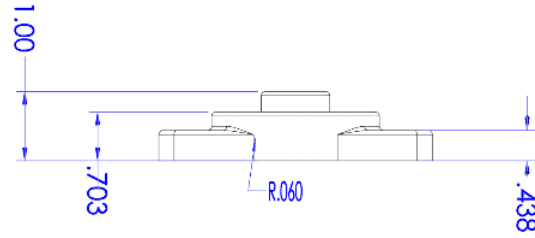


Figure 35: Flange structure and dimensions.

The specific constrained topology optimization problem considered here is:

$$\begin{aligned}
 & \underset{\Omega \subset D}{\text{Min}} |\Omega| \\
 & J \leq (\alpha_1) J_0 \\
 & \sigma \leq (\alpha_2) \sigma_0 \\
 & \lambda \geq (\alpha_4) \lambda_0 \quad (\text{soft, if } \alpha_4 > 1)
 \end{aligned} \tag{83}$$

The Eigen-mode constraint is soft if the corresponding multiplier is greater than 1, to avoid early termination.

Table-4 summarizes the results for 3 different scenarios. In particular, for scenario-3, observe that although the Eigen-value constraint is soft, its impact on the final result and topology is self-evident.

Table 16: Constraints and results for problem in Figure 35.

Dominant Constraint	Initial Constraints	Final Results	Final volume & running time (s)
Compliance	$J \leq 2J_0$ $\sigma \leq 100\sigma_0$ $\lambda \geq 0.1\lambda_0$	$J = 2J_0$ $\sigma = 1.12\sigma_0$ $\lambda = 0.69\lambda_0$	$v = 0.44$ $t = 156.91$
Stress	$J \leq 100J_0$ $\sigma \leq 1.05\sigma_0$ $\lambda \geq 0.1\lambda_0$	$J = 4.66J_0$ $\sigma = 1.05\sigma_0$ $\lambda = 1.27\lambda_0$	$v = 0.44$ $t = 185.97$

Stress and Eigen-value	$J \leq 100J_0$	$J = 1.84J_0$	$\nu = 0.68$
	$\sigma \leq 1.2\sigma_0$	$\sigma = 1.20\sigma_0$	$t = 77.22$
	$\lambda \geq 1.5\lambda_0$ (soft)	$\lambda = 2.49\lambda_0$	

The corresponding topologies are illustrated in Figure 36. The volume fractions for the first two scenarios are identical, but the difference in topology is worth noticing (also see Table-4).

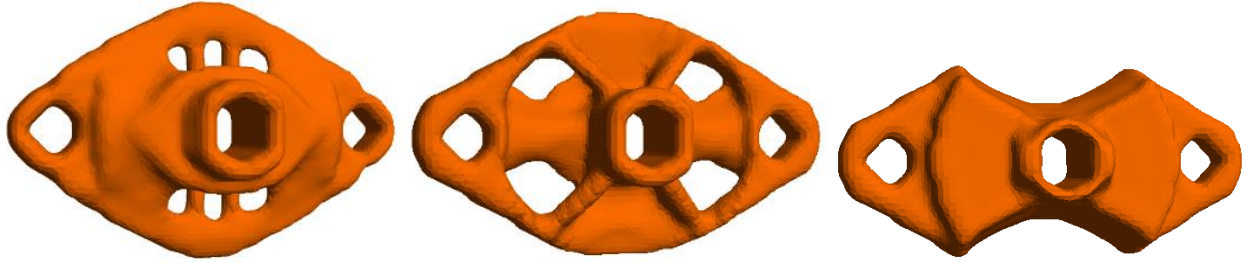


Figure 36: Final topologies for compliance dominated (top-left) stress dominated (top-right), and stress and Eigen-value dominated (bottom).

In order to study the iteration history of the soft-constrained optimization, the volume decrement history is plotted in Figure 37 for scenario-3 in Table 16. It is seen the volume decrement was kept constant until the last two steps when convergence error was detected.

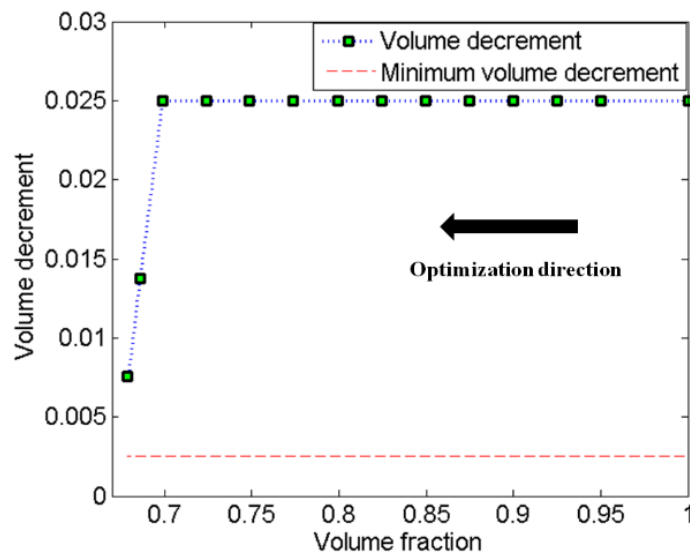


Figure 37: Volume decrement history for scenario-3 in Table 16.

The constraint iteration history for scenario-3 in Table 16 is illustrated in Figure 38 (plots are to be interpreted from right to left) where the lowest eigen-value sees a significant increase with material removal. However, since the eigen-value constraint is ‘soft’, it does not lead to early termination. The optimization terminated due to a hard stress constraint of 1.2 at a final volume of 0.68.

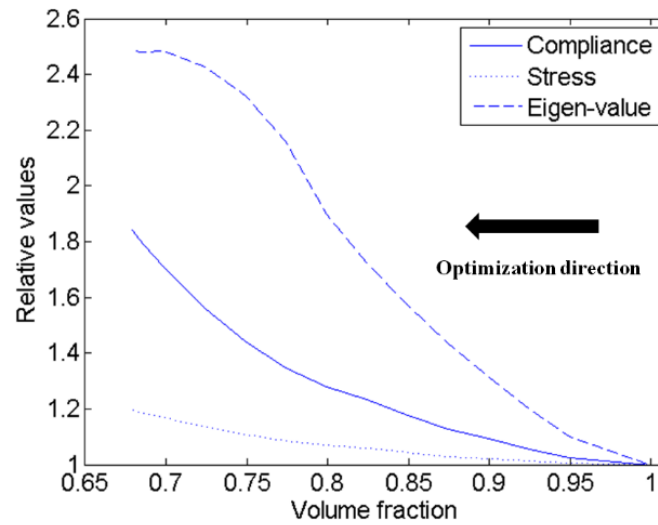


Figure 38: Iteration history of constraints for scenario-3 in Table 16.

6.5.4 Case Study: Bicycle Frame

In this case study, we use the proposed algorithm to find a conceptual design for a bicycle frame. The design space is illustrated in Figure 39 where all units are in centimeters.

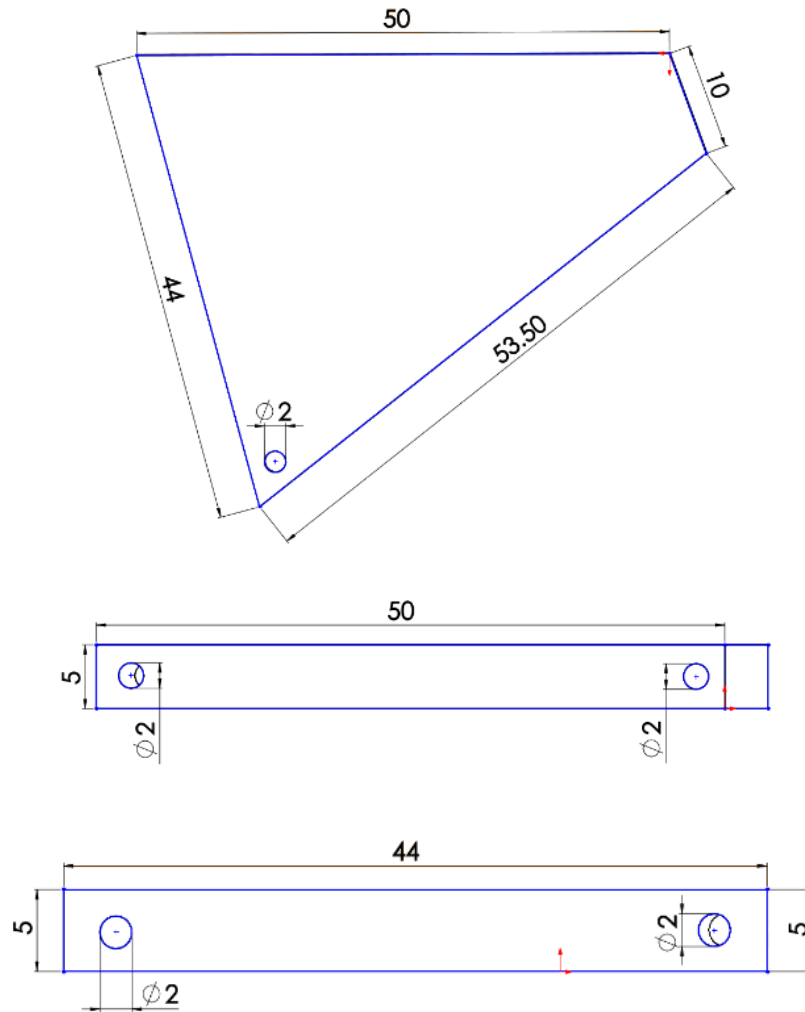


Figure 39: Design space of bike frame: front view (1st), top view (2nd) and side view (3rd)

Two loads are applied as in Figure 40, where F_1 is 60 N, and F_2 is 140 N; see [139]. The two loads act simultaneously, i.e., this is a *multiple-load problem*. The design is discretized into 51,280 hexahedral elements, i.e. 176,367 DOFs.

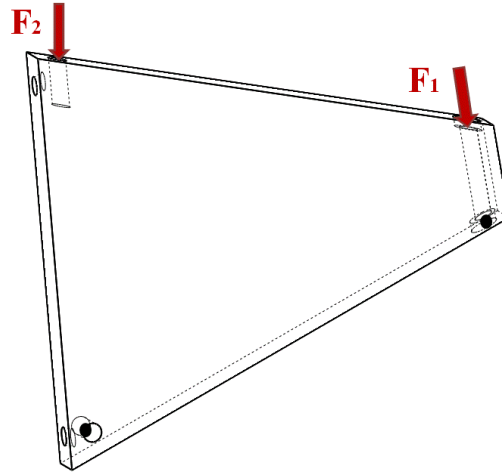


Figure 40: The bike frame subject to multiple loads.

Only one scenario is considered; the constraints and final results are summarized in Table 17.

Table 17: Constraints and results for problem in Figure 40.

Dominant Constraint	Initial Constraints	Final Results	Final volume & running time (s)
Compliance, Stress and Buckling	$J \leq 20J_0$ $\sigma \leq 20\sigma_0$ $P \geq 1.5P_0$ (<i>soft</i>)	$J = 19.47J_0$ $\sigma = 11.92\sigma_0$ $P = 0.08P_0$	$v = 0.22$ $t = 953.58$

The final design is illustrated in Figure 41.



Figure 41: Proposed design for a bike frame.

6.5.5 Case Study: Bicycle crank

In the final case-study, we optimize the design of a bicycle crank arm. The 2-D sketch of the design space is illustrated in Figure 42 (units in mm), with a thickness of 15 mm. The structure is discretized using 36,608 elements, with 128,250 DOFs.

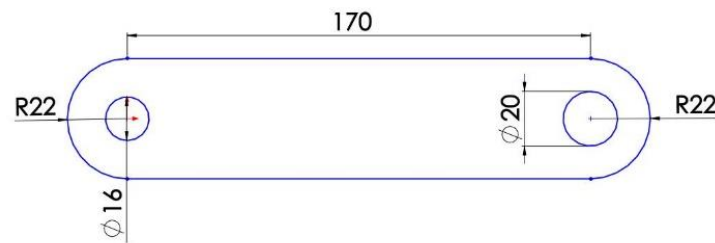


Figure 42: Dimensions of the crank arm.

In this example, a *multi-load* scenario is considered, i.e., during a full pedaling cycle, the crank arm passes through four distinct positions as illustrated in Figure 43. At each position, it experiences a different loading condition. At position A where the pedal is passing through the highest point, it sees a compressive load. At position B where the crank arm is horizontally placed, it sees a bending load. At position C, it sees a tension force. At position D, the load is negligible. The magnitudes of pedaling forces F_1 , F_2 and F_3 are in the ratio 1:5:2.2, with F_1 being 50 N [140].

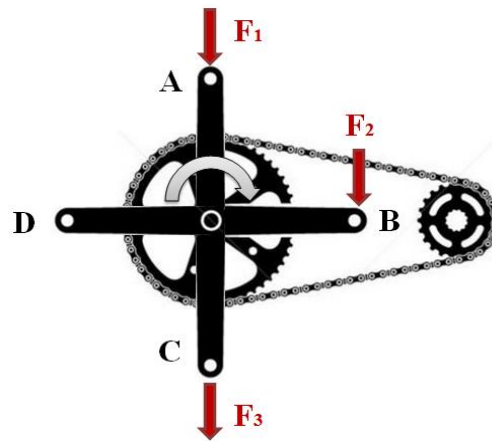


Figure 43: The crank arm subject to multi-load during a pedaling cycle [140].

The objective is to minimize the weight subject to the constraints summarized in Table 18; stiffness and strength being the most important constraints. A soft buckling constraint is imposed for the compressive load F_1 . Thus, one can impose different constraints for different sets of loads.

The optimization results are summarized in Table 18 where it is noted that the compliance constraints for loads F_1 and F_3 are active at termination. Since this is a multi-load problem, the computational cost is fairly high (about 25 minutes), despite the use of fast assembly-free methods.

Table 18: Constraints and results for problem in Figure 42.

Loads	Initial Constraints	Final Results	v & t (s)
Compression F_1	$J \leq 1.5J_0$ $\sigma \leq 4\sigma_0$ $P \geq 5P_0$ (soft)	$J = 1.50J_0$ $\sigma = 1.33\sigma_0$ $P = 0.75P_0$	$v = 0.69$ $t = 1507.29$
Bending F_2	$J \leq 1.5J_0$ $\sigma \leq 4\sigma_0$	$J = 1.25J_0$ $\sigma = 1.01\sigma_0$	
Tension F_3	$J \leq 1.5J_0$ $\sigma \leq 4\sigma_0$	$J = 1.50J_0$ $\sigma = 1.33\sigma_0$	

The final topology is illustrated in Figure 44. Although the design meets the performance constraints, it exhibits ‘undercuts’, i.e., cavities. This may not be desirable if the part needs to be cast.

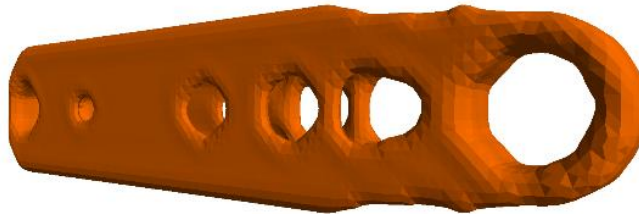


Figure 44: Final design of crank arm.

We therefore imposed a casting constraint (through the thickness) in addition to the performance constraints; the results are summarized in Table 19. Observe that the design now not only meets the performance constraint, but also the manufacturing constraint. In this example, the impact of the manufacturing constraint on performance, and computational time, was found to be negligible.

Table 19: Constraints and results for problem in Figure 42.

Loads	Initial Constraints	Final Constraints	v & t (s)
Compression F_1	$J \leq 1.5J_0$ $\sigma \leq 4\sigma_0$ $P \geq 5P_0$ (<i>soft</i>)	$J = 1.50J_0$ $\sigma = 1.30\sigma_0$ $P = 0.72P_0$	$v = 0.70$ $t = 1489.59$
Bending F_2	$J \leq 1.5J_0$ $\sigma \leq 4\sigma_0$	$J = 1.23J_0$ $\sigma = 1.01\sigma_0$	
Tension F_3	$J \leq 1.5J_0$ $\sigma \leq 4\sigma_0$	$J = 1.50J_0$ $\sigma = 1.30\sigma_0$	

The resulting design is illustrated in Figure 45; observe that the design does not exhibit undercuts.

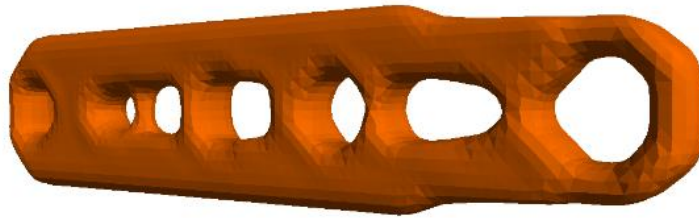


Figure 45: Final design of crank arm with casting constraint.

The proposed method inherits the robustness and generality of the classic augmented Lagrangian method. Specifically, through several numerical experiments, we demonstrated that the proposed method can solve a variety of multi-constrained (single-load, multiple-load and

multi-load) topology optimization problems. By varying the constraint limits, we were able to explore the impact of these constraints on the final topology. We were also able to explore the impact of manufacturing constraint on the topology.

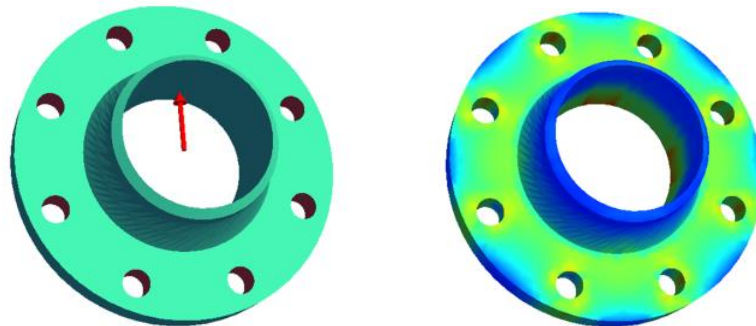
7. LARGE-SCALE THERMO-ELASTIC MULTI-CONSTRAINED TOPOLOGY OPTIMIZATION

Popular methods for solving thermo-elastic topology optimization problems include Solid Isotropic Material with Penalization (SIMP) and Rational Approximation of Material Properties (RAMP). Here we propose an augmented topological level-set method that combines discrete topological sensitivity with augmented Lagrangian formulation. Both spatially uniform and spatially varying temperature changes are considered, and appropriate adjoint equations are developed.

This leads to a comprehensive and efficient method for solving 3D stress and compliance constrained thermo-elastic topology optimization problems. Benchmark examples and case studies are presented to illustrate the efficacy of the proposed algorithm.

The focus of this chapter is on thermo-elastic topology optimization where the objective is to optimize components that are subject to both structural and thermal loads.

Figure 46, for example, illustrates a flange⁴ that is subject to both a structural load, and a thermal load.



⁴ The corresponding STL file is downloaded from www.grabcad.com.

Figure 46: The structurally loaded flange (left) is also subject to a thermal load; the resulting stress plot (right).

The objective of this chapter is to develop an efficient thermo-elastic topology optimization method, accounting for various thermal/elastic scenarios.

Table 2 provides a chronological summary of the above literature review. From the table, one can identify the following research gaps.

First, most of the researchers have focused on *uniform* temperature elevation; few have studied the effects of spatially varying temperature. Figure 47, for example, illustrates an exhaust duct⁵ subject to a spatially varying temperature. Such structures pose additional challenges during optimization, and these are discussed and addressed in this chapter.

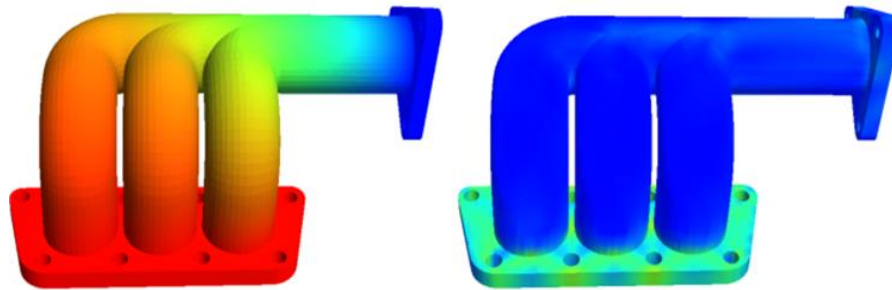


Figure 47: Restrained exhaust duct subject to temperature gradient (left) and resulting stress (right).

Second, most of the existing thermo-elastic topology optimization methods have focused on 2D problems; very little progress has been reported on large-scale 3D problems, where the efficiency of the underlying optimization method becomes important.

⁵ The corresponding STL file is downloaded from www.grabcad.com.

Finally, constraints in thermo-elastic topology optimization have largely been restricted to simple constraints such as volume and compliance. A methodology to include a variety of performance constraints is lacking.

To address these research gaps, a new level-set method is proposed in this chapter. The proposed combines a discrete approximation to the topological sensitivity with augmented Lagrangian formulation to address spatially varying thermal problems, subject to a variety of constraints. In addition, to address the computational challenges, the assembly-free deflated finite element method proposed in [131] is extended here to address efficient 3D thermo-elastic analysis.

7.1 Approximate Thermo-Elastic Topological Sensitivity

Let Q be any quantity of interest in a thermo-elastic optimization problem; Q can either be an objective, or a constraint. To compute the sensitivity of Q with respect to a topological change, two distinct cases are considered: (a) spatially uniform increase in temperature, and (b) spatially varying temperature.

7.1.1 Spatially Uniform Increase in Temperature

In the case of a uniform temperature change, the sensitivity of Q , by definition, is given by:

$$Q' = (\nabla_d Q)^T d' \quad (84)$$

Further, from Equation (14):

$$K'd + Kd' = f_{st}' + f_{th}' \quad (85)$$

If one assumes that the structural body forces are absent, then its sensitivity to a topological change is zero:

$$d' = K^{-1}(f_{th}' - K'd) \quad (86)$$

Since the temperature change is spatially uniform, the change in thermal load (due to topological change) is given by (see Equation (15) and Equation (16)):

$$f_{th}' = H'\Delta t \quad (87)$$

where

$$H = \sum_{elems} \int_{\Omega} B^T D \alpha \Phi d\Omega \quad (88)$$

Substituting Equation (87) in Equation (86) we have:

$$d' = K^{-1}(H'\Delta t - K'd) \quad (89)$$

Finally, substituting Equation (89) in Equation (84), we have:

$$Q' = (\nabla_d Q)^T K^{-1}(H'\Delta t - K'd) \quad (90)$$

One can now define the structural adjoint λ as follows:

$$K\lambda = -\nabla_d Q \quad (91)$$

Thus, we have:

$$Q' = -\lambda^T (H'\Delta t - K'd) \quad (92)$$

For clarity, Equation (92) can be expressed as:

$$Q' = Q_{th}' - Q_{st}' \quad (93)$$

where

$$\begin{aligned} Q_{th}' &= -\lambda^T H' \Delta t \\ Q_{st}' &= -\lambda^T K' d \end{aligned} \quad (94)$$

Observe that, as the topology evolves, the sensitivity in Equation (93) can take either a positive or a negative value. This non-monotonic behavior can pose challenges for traditional monotonic approximation methods such as MMA and CONLIN [141]. In this chapter, we employ fixed-point iteration that does not suffer from this limitation, as illustrated later through numerical experiments.

Further observe that the structural adjoint λ depends on the quantity of interest; two specific instances are considered below.

Compliance

If the quantity of interest Q is compliance, i.e., if

$$Q = J = d^T (f_m + f_{th}) \quad (95)$$

then

$$\lambda = -K^{-1} \nabla_d Q = -K^{-1} f = -d \quad (96)$$

Therefore

$$Q' = J' = d^T H' \Delta t - d^T K' d \quad (97)$$

P-norm von Mises Stress

On the other hand, if Q is the p -norm stress [74], i.e., if

$$Q = \left(\sum_e (\sigma_e)^p \right)^{1/p} \quad (98)$$

where:

$$\sigma_e = \frac{1}{\sqrt{2}} \sqrt{(\sigma_{11} - \sigma_{22})^2 + (\sigma_{11} - \sigma_{33})^2 + \dots} \\ \sqrt{(\sigma_{22} - \sigma_{33})^2 + \dots} \\ \sqrt{6(\sigma_{12}\sigma_{12} + \sigma_{13}\sigma_{13} + \sigma_{23}\sigma_{23})} \quad (99)$$

Then, the adjoint is defined by (see [74]):

$$K\lambda = -\nabla_d Q = g \quad (100)$$

where

$$g = -\frac{1}{p} \left(\sum_e (\sigma_e)^p \right)^{\frac{1}{p}-1} \left[\sum_e g_e \right] \quad (101)$$

and

$$g_e = \frac{1}{\sqrt{2}} p (\sigma_e)^{p-2} \begin{pmatrix} (\sigma_{11} - \sigma_{22})(F_1 - F_2) + \\ (\sigma_{11} - \sigma_{33})(F_1 - F_3) + \\ (\sigma_{22} - \sigma_{33})(F_2 - F_3) + \\ 6(\sigma_{12}F_4 + \sigma_{13}F_5 + \sigma_{23}F_6) \end{pmatrix} \quad (102)$$

$$[F] = [D][B_e] \quad (103)$$

where B_e was defined in Equation (15); please see [74] for details.

7.1.2 Non-Uniform Change in Temperature

Now consider the case of a non-uniform temperature change. In this case, one must solve Equation (13), and we have:

$$Q' = (\nabla_d Q)^T d' + (\nabla_t Q)^T t' \quad (104)$$

As before, the displacement sensitivity is given by Equation (86); therefore:

$$Q' = (\nabla_d Q)^T K^{-1} (f_{th}' - K'd) + (\nabla_t Q)^T t' \quad (105)$$

However, the sensitivity of the thermal load is governed by:

$$f_{th}' = Ht' + H't \quad (106)$$

If one assumes that the sensitivity of the thermal flux in Equation (13) to a topological change is zero, then:

$$t' = K_t^{-1} K_t' t \quad (107)$$

Therefore:

$$Q' = \nabla_d Q^T K^{-1} (Ht' + H't - K'd) + \nabla_t Q^T K_t^{-1} K_t' t \quad (108)$$

We now define the thermal adjoint ξ and thermo-elastic adjoint ω as follows:

$$K_t \xi = \nabla_t Q \quad (109)$$

$$K_t \omega = H^T \lambda \quad (110)$$

To the best of our knowledge, these adjoints have not been identified in the literature.

Substituting these definitions into Equation (108):

$$Q' = -\omega^T K_t' t + \lambda^T H t - \lambda^T K' d + \xi^T K_t' t \quad (111)$$

Once again, for clarity, one can express Equation (111) as:

$$Q' = Q_{th}' - Q_{st}' \quad (112)$$

with

$$\begin{aligned} Q_{th}' &= \xi^T K_t' t - \omega^T K_t' t + \lambda^T H t \\ Q_{st}' &= \lambda^T K' d \end{aligned} \quad (113)$$

As before, we consider two special cases for the quantity of interest.

Compliance

If the quantity of interest Q is compliance, the adjoints are given by:

$$\lambda = -K^{-1} f = -d \quad (114)$$

$$\xi = K_t^{-1} H^T d \quad (115)$$

$$\omega = K_t^{-1} H^T \lambda = -K_t^{-1} H^T d = -\xi \quad (116)$$

Therefore, the compliance sensitivity simplifies to:

$$Q' = J' = -2\omega^T K_t' t - d^T H t + d^T K' d \quad (117)$$

P-norm von Mises Stress

If the quantity of interest is p-norm stress (see Equation (98)) the structural adjoint λ is given by Equation (100), while thermal adjoint is defined by:

$$K_t \xi = -\nabla_t Q \equiv g_t \quad (118)$$

where:

$$g_t = -\frac{1}{p} \left(\sum_e (\sigma_e)^p \right)^{\frac{1}{p}-1} \left[\sum_e g_{te} \right] \quad (119)$$

with

$$g_{te} = \frac{1}{\sqrt{2}} p (\sigma_e)^{p-2} \begin{pmatrix} (\sigma_{11} - \sigma_{22})(G_1 - G_2) + \\ (\sigma_{11} - \sigma_{33})(G_1 - G_3) + \\ (\sigma_{22} - \sigma_{33})(G_2 - G_3) + \\ 6(\sigma_{12}G_4 + \sigma_{13}G_5 + \sigma_{23}G_6) \end{pmatrix} \quad (120)$$

$$[G] = \frac{1}{8} \alpha [D] [\Phi] \quad (121)$$

where Φ was defined in Equation (16). Once these two adjoints have been computed, the thermo-elastic adjoint can be computed via Equation (110).

To summarize, various expressions for the sensitivity are summarized in the table below.

Table 20: Sensitivity expressions

Q'	Compliance	Generic
<i>Uniform temperature change</i>	$d^T H' \Delta t - d^T K' d$	$-\lambda^T (H' \Delta t - K' d)$
<i>Spatially varying temperature</i>	$\begin{bmatrix} -2\omega^T K'_t t - d^T H' t \\ +d^T K' d \end{bmatrix}$	$\begin{bmatrix} -\omega^T K'_t t + \lambda^T H' t \\ -\lambda^T K' d + \xi^T K'_t t \end{bmatrix}$

7.1.3 Sensitivity of Stiffness Matrices

The last step is to compute the sensitivity of the stiffness matrices (K , H and K_i) in the above table. If pseudo-density parameterization is used (as in SIMP and RAMP), then the sensitivities can be computed via their respective material interpolation scheme [53]. One of the challenges with this approach is that the stiffness matrices will exhibit large condition numbers due to the spread in pseudo-densities [131]. This will result in slow convergence of iterative solvers. Here, we employ a discrete approximation, i.e., the sensitivities of the stiffness matrices are computed at the center of each element, for example:

$$K' \equiv [K_e] \quad (122)$$

and then smoothened.

7.2 Algorithm of Large-Scale Thermo-Elastic Constrained Topology Optimization

Finally, the proposed algorithm proceeds as follows (see Figure 48):

- 1) The domain is discretized using finite elements (here 3D hexahedral elements). The optimization starts at a volume fraction of 1.0. The ‘volume decrement’ Δv is set to 0.025. The initial values of Lagrangian multiplier and penalty number are set as 100 and 10.
- 2) The thermal problem (if necessary) and the structural problem in Equations (13) and (14) are solved.
- 3) The constraint values are calculated, and the optimization parameters (multiplier and penalty) are updated.
- 4) If any of the constraints is violated, the algorithm proceeds to step-9, else, it proceeds to step-5.

- 5) The sensitivities are calculated for each of the constraints, and the augmented element sensitivity field is computed.
- 6) Treating the augmented sensitivity field as a level-set; a new topology with a volume fraction of $(v - \Delta v)$ is extracted.
- 7) The compliance is now computed over the new topology. If the compliance has converged, then the optimization moves to the next step, else it goes to step 9.
- 8) The current volume fraction is set to $(v - \Delta v)$. If the target volume fraction has not been reached, the optimization returns to step 2 to repeat iterations; else, terminate iteration and exit.
- 9) Step-size is reduced; check if volume decrement is below threshold. If not, the optimization returns to Step-2; else, terminate the iteration.

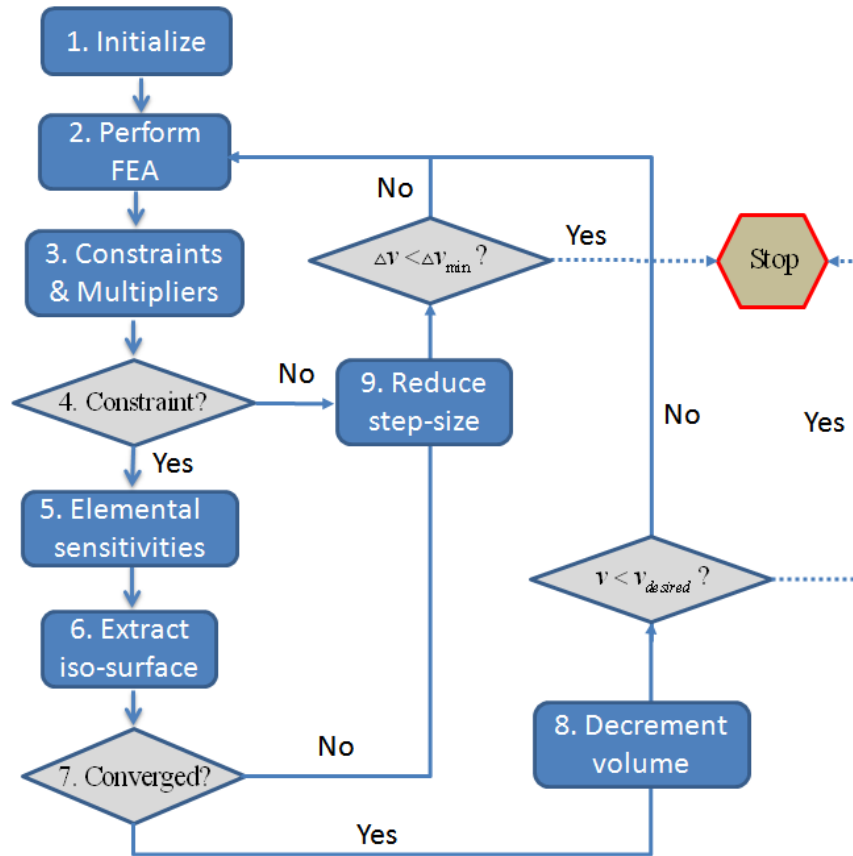


Figure 48: An overview of the algorithm.

7.3 Numerical Experiments

In this Section, we demonstrate the efficacy of the proposed algorithm through numerical experiments. The default parameters are as follows:

- The material is assumed to be steel, i.e., the elastic modulus is $E = 2e11 Pa$, the Poisson ratio is $\nu = 0.3$ and the coefficient of thermal expansion $\alpha = 1.2 * 10^{-5} / C$.
- The reference temperature with zero stress is $23^{\circ}C$.
- Unless otherwise noted, the p-norm value used for computing the p-norm stress is 6.
- 8-noded hexahedral elements are used for 3D FEA.

- All experiments were conducted using C++ on a Windows 7 64-bit machine with the following hardware: Intel I7 960 CPU quad-core running at 3.2GHz with 6 GB of memory.
- The desired volume fraction is 0.25, unless otherwise noted. In other words, the optimization terminates if the constraints are violated or if the desired volume fraction of 0.25 is reached.

The numerical experiments are organized as follows. Section 5.1 is a benchmark example to study the effectiveness of the proposed method for uniformly elevated temperature; both compliance and stress dominated problems are considered. In Section 5.2, another benchmark example is considered to study the effect of spatially varying temperature. In Section 5.3, a case-study involving a flange subject to a uniform temperature increase is considered. Finally, in Section 5.4, a case study is considered where the structure is subject to temperature gradient fields. Important conclusions are drawn for each of the examples.

7.3.1 Benchmark: Bi-clamped beam with a point load

The aim of this experiment is two-fold: (1) illustrate the proposed algorithm for a benchmark problem [18], (2) illustrate the impact of temperature variations on the final topology.

The structure is illustrated in Figure 49 [18], units are in meters, the load is 105 N, the thickness is 0.02m, and the structure is also subject to a homogeneous temperature increase of ΔT , specified below. Since the thickness is small, the problem can be modeled as plane-stress [18]. However, it is modeled here in 3D, and the domain is meshed with 15,000 hexahedral elements.

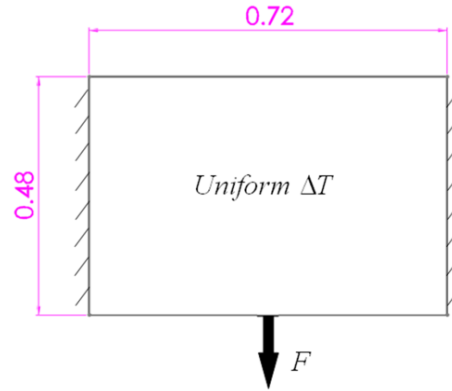


Figure 49: The bi-clamped structure with a central point load.

Compliance Formulation (Stiff Designs)

We first consider compliance-constrained thermo-elastic topology optimization problem:

$$\begin{aligned}
 & \underset{\Omega \subset D}{\text{Min}} |\Omega| \\
 & |\Omega| \geq 0.25|D| \\
 & J \leq 5J_0 \\
 & \text{subject to} \\
 & Kd = f_{st} + f_{th} \\
 & \Delta T : \text{Specified}
 \end{aligned} \tag{123}$$

Observe that the thermal problem in Equation (13) need not be considered since the temperature increase is prescribed.

If the temperature increase ΔT is 10C, the optimized topology for a 0.25 volume fraction is illustrated in Figure 50. The computational time is 58 seconds, involving 242 FEAs; the topology is identical to the one obtained in [18]. The final compliance is almost twice the initial compliance, while the stress has not increased significantly.

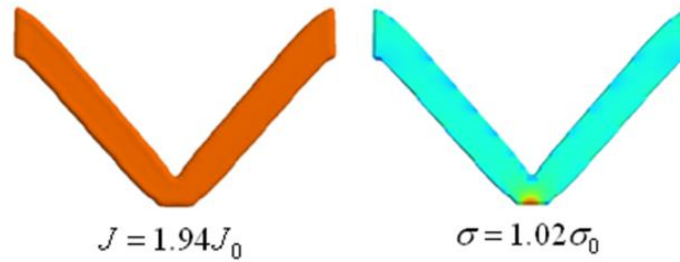


Figure 50: Optimized topology for compliance-constrained topology optimization.

The iteration history is illustrated in Figure 51; one can observe the non-monotonic behavior of compliance, consistent with the discussion following Equation (94).

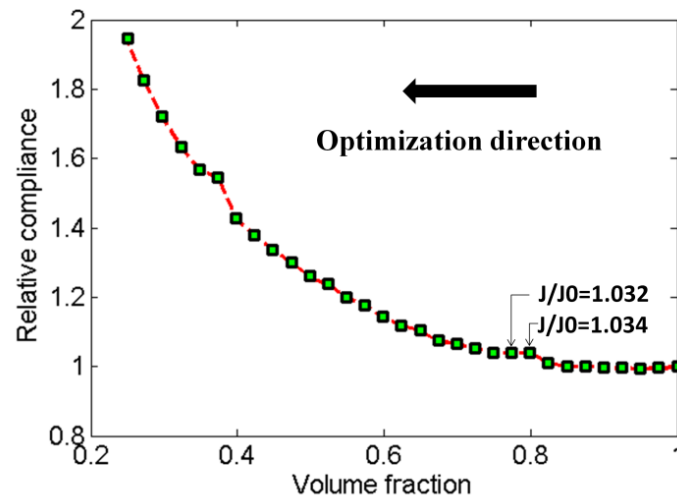


Figure 51: Iteration history of compliance for problem in Equation (123).

Next, we consider the impact of temperature change ΔT on the final topology. The target volume fraction was set to 0.25 and the final topologies are illustrated in Figure 52 for a temperature change ranging from $-5^\circ C$ to $+5^\circ C$. As one can observe, the final topology is a strong function of the temperature change, especially for a positive change.

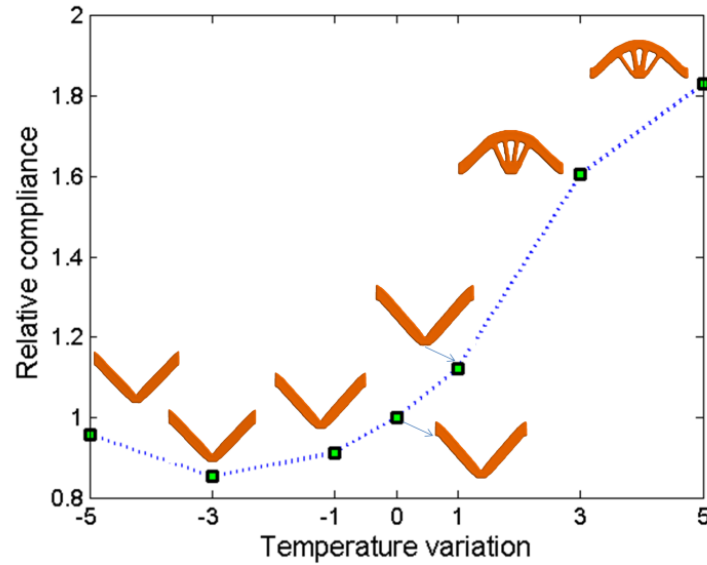


Figure 52: The final topologies for different temperature variations for problem in Equation (123).

There are two observations: First, if the temperature is increased, the compliance monotonically increases; second, if the temperature is decreased, the compliance first decreases, and then increases. One possible reason is that when the temperature decrement is small (e.g. $-1^{\circ}C$), the compressive thermal load partly cancels the tensile structural load.

The relative magnitudes of thermal and mechanical loads are summarized in Table 21.

Table 21: Load ratios for different temperature variations

ΔT ($^{\circ}C$)	-5	-3	-1	0	1	3	5
$\ \mathbf{f}_{th}\ /\ \mathbf{f}_{st}\ $	3.83	2.06	0.35	0	0.42	2.08	3.91

Stress Formulation (Strong Designs)

We pose a stress dominated thermo-elastic topology optimization as follows:

$$\begin{aligned}
& \underset{\Omega \subset D}{\text{Min}} |\Omega| \\
& |\Omega| \geq 0.25|D| \\
& \sigma \leq 2\sigma_0 \\
& \text{subject to} \\
& Kd = f_{st} + f_{th} \\
& \Delta T : \text{Specified}
\end{aligned} \tag{124}$$

Similar to the previous experiment, the temperature is uniformly elevated by 10^0C . The resulting topology of 0.25 volume fraction is illustrated in Figure 53. The computing time was 122 seconds involving 363 FEA. The increased computing time is due to the additional adjoint FEA that needs to be performed.

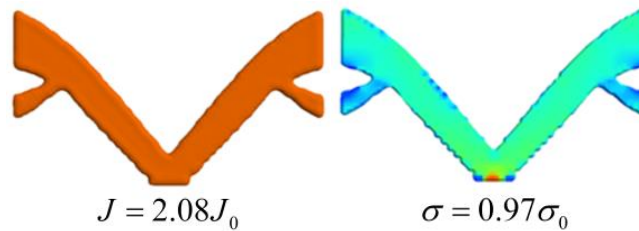


Figure 53: The optimized topology for stress-constrained topology optimization.

Comparing Figure 53 and Figure 50, it can be observed that: (1) compliance and stress dominated topology optimization lead to slightly different topologies, and (2) the topology in Figure 50 has lower compliance while the topology in Figure 53 and has lower stress, as expected.

The final topologies for different temperature variations are illustrated in Figure 54. As one can observe, the topologies are significantly different from those in Figure 52.

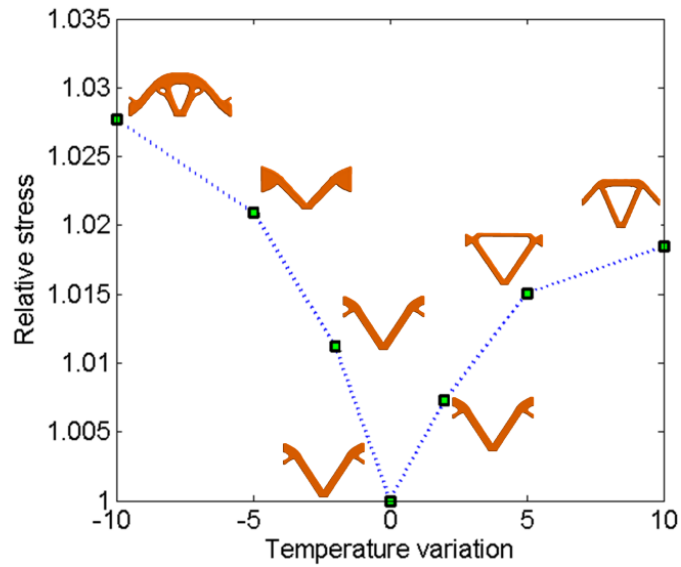


Figure 54: The final topologies for different temperature variations.

7.3.2 Benchmark: Distributed load Bi-clamped beam

The aim of this experiment is to study the impact of non-uniform temperature on the final topology.

We once again consider the bi-clamped beam but with a distributed load as illustrated in Figure 13 [18]. The dimension of this beam is $0.5m \times 0.28m \times 0.01m$ and the distributed load is $P = 6e5Pa$. Once again the problem is modeled in 3D, and the domain is meshed with 15,000 hexahedral elements.

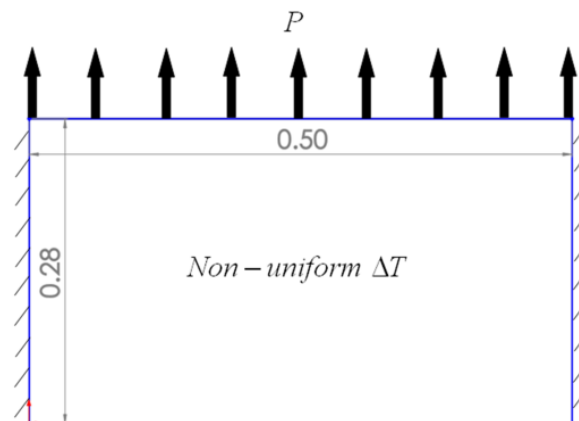


Figure 55: The bi-clamped structure with a distributed load.

Compliance Formulation (Stiff Designs)

The specific problem being considered here is:

$$\begin{aligned}
 & \underset{\Omega \subset D}{\text{Min}} |\Omega| \\
 & |\Omega| \geq 0.30 |D| \\
 & J \leq 5J_0 \\
 & \text{subject to} \\
 & Kd = f_{st} + f_{th} \\
 & K_t t = q
 \end{aligned} \tag{125}$$

If the temperature is uniformly elevated by $\Delta T = 20^\circ C$, the resulting topology and stress distribution are illustrated in Figure 56. This is consistent with the topology in [18].

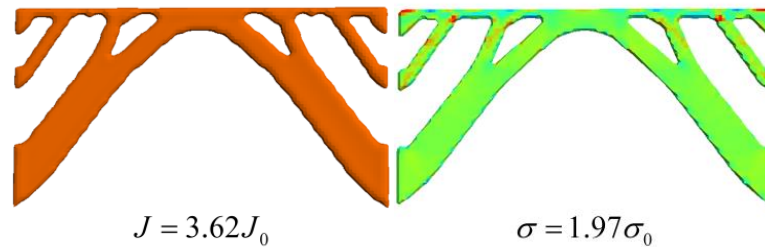


Figure 56: Final topology and stress distribution when the structure in Figure 13 is subject to uniform temperature rise.

Next, we consider the impact of spatially varying temperature on the optimal designs. Specifically, we increased the temperature on the left edge by $\Delta T = 0^\circ C$, and on the right edge by $\Delta T = 40^\circ C$, i.e., the average change in temperature is $\Delta T = 20^\circ C$. The final topology and its stress distribution are shown in Figure 57 where the asymmetry is due to the spatial thermal gradient. Comparison between Figure 56 and Figure 57 highlights the importance of accounting for spatially distributed temperature profiles.

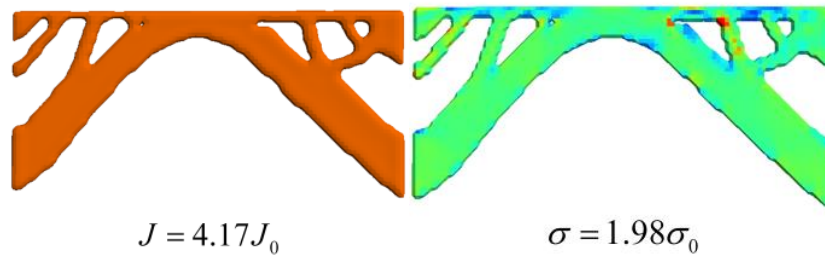


Figure 57: Final topology and stress distribution when the structure is subject to spatially temperature gradient.

The iteration history for the second experiment is illustrated in Figure 58. It is observed that: (1) both compliance and stress increase as volume decreases, although not monotonically; (2) the increase of compliance is generally smoother than stress.

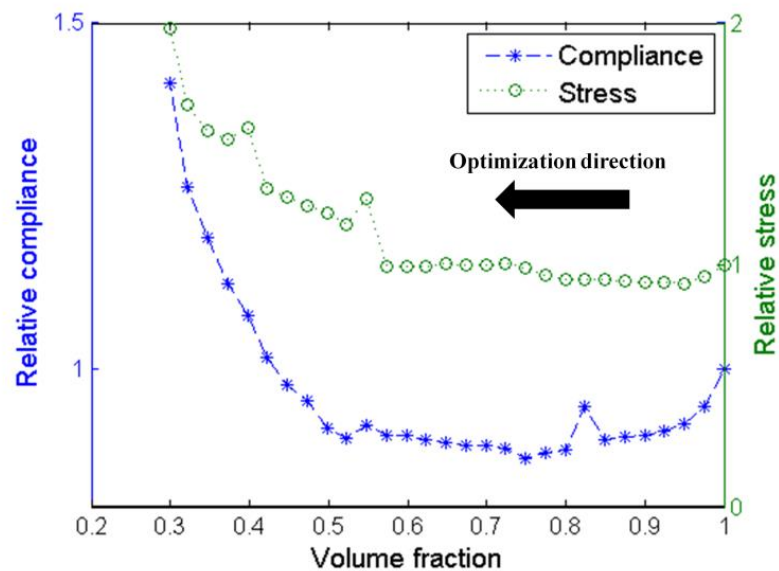


Figure 58: Iteration history of compliance and stress for problem in Equation (125).

Stress Formulation (Strong Designs)

Next a stress dominated problem is considered for the above problem in Figure 13:

$$\begin{aligned}
& \underset{\Omega \subset D}{\text{Min}} |\Omega| \\
& |\Omega| \geq 0.30|D| \\
& \sigma \leq 2\sigma_0 \\
& \text{subject to} \\
& Kd = f_{st} + f_{th} \\
& K_t t = q
\end{aligned} \tag{126}$$

On the left edge there was no temperature change, i.e., $\Delta T = 0^\circ C$, and on the right edge the change was $\Delta T = 40^\circ C$.

The final topology and stress distribution results are illustrated in Figure 59. Observe the strong asymmetry in the stress-dominated problem.

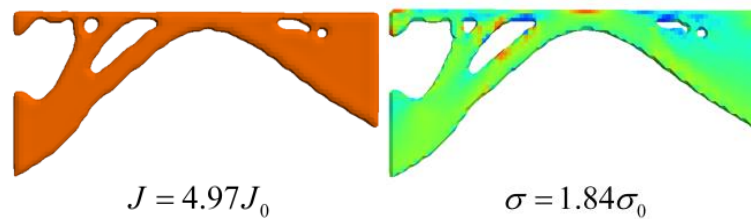


Figure 59: Final topology and stress distribution of stress-constrained topology optimization subject to spatially temperature gradient.

Comparing the results in Figure 59 with Figure 57, it is clear: (1) the two optimization problems lead to distinct topologies; (2) for the same final volume fraction, a compliance minimization leads to a lower compliance result while a stress minimization leads to a lower stress value. The iteration history of the optimization process is shown in Figure 60.

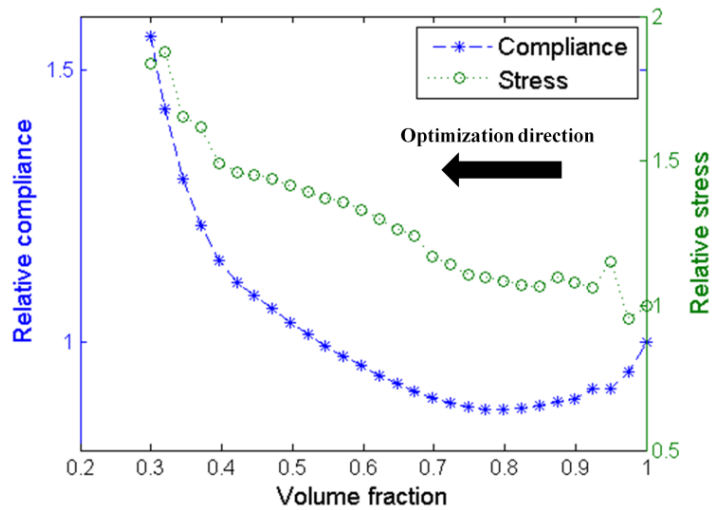
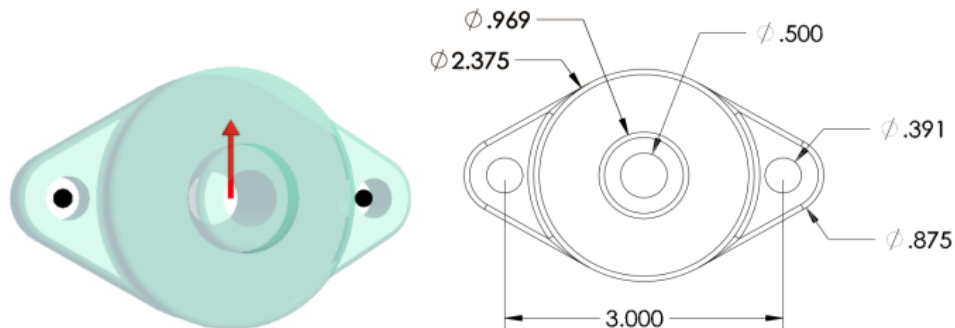


Figure 60: Iteration history of stress constrained topology optimization for problem in Equation (126).

7.3.3 Case study: Flange

The purpose of this section is to show the robustness of the proposed algorithm for a non-trivial application. In particular, a thermo-elastic topology optimization problem over a flange is studied in this section. Flanges are commonly used, for example, to fasten pipes and rail-joints, and they are often subject to temperature changes. The dimensions of the flange and boundary conditions are illustrated in Figure 35. The flange is fixed at the two bolt centers, and a vertical force of $10^5 N$ is applied as shown. For FEA, 51,500 hexahedral elements are used to discretize the design domain, resulting in 175,374 DOF.



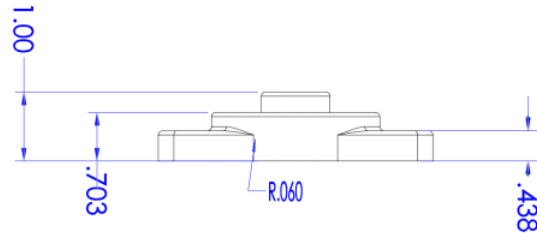


Figure 61: Flange structure and dimensions (unit: m).

The specific thermo-elastic topology optimization problem considered here is:

$$\begin{aligned}
 & \underset{\Omega \subset D}{\text{Min}} |\Omega| \\
 & |\Omega| \geq 0.25|D| \\
 & J \leq 5J_0 \\
 & \sigma \leq 1.5\sigma_0 \\
 & \text{subject to} \\
 & Kd = f_{st} + f_{th}
 \end{aligned} \tag{127}$$

First, a pure elastic problem (i.e., zero thermal load in Equation (127)) is considered. The resulting topology is illustrated in Figure 62 and the final constraint values are shown in Table 22 where the optimization terminates due to the active stress constraint identified with a "box".

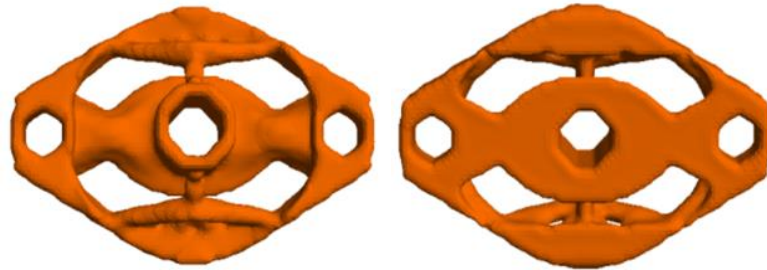


Figure 62: Top view and bottom view of final topology for the pure elastic flange problem.

Table 22: Constraints and results for problem in Figure 62.

Initial Constraints	Final Results	Final volume fraction & time (sec)	Final load ratio
$J \leq 5J_0$ $\sigma \leq 1.5\sigma_0$	$J = 4.89J_0$ <div style="border: 1px solid black; padding: 2px; display: inline-block;">$\sigma = 1.50\sigma_0$</div>	$V = 0.36$ $T = 212.39$	$\frac{\ f_m\ }{\ f_m\ } = 0$

Then, the thermal effect is added; we subject the structure to a uniform temperature elevation of 300C.

The optimized topology, computed in 160 FEAs, is illustrated in Figure 63. Other results are summarized in Table 10; this problem terminated due to an active compliance constraint. Although the thermal load is small compared to the structural load, as noted in the fourth column of Table 10, this has a significant effect on the final topology.

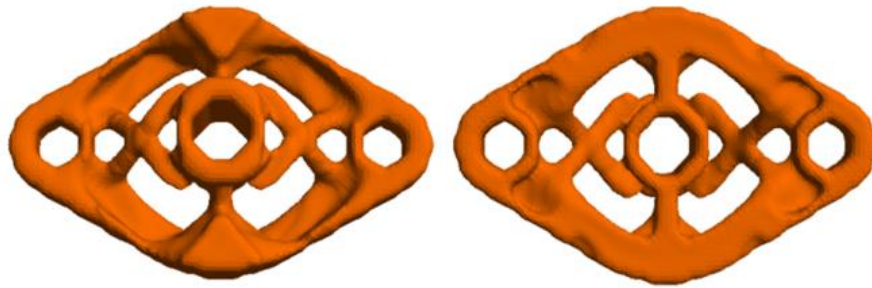


Figure 63: Top view and bottom view of final topology of the flange subject to a uniform temperature rise.

Table 23: Constraints and results for problem in Equation (127).

Initial Constraints	Final Results	Final volume fraction & time (sec)	Final load ratio
$J \leq 5J_0$ $\sigma \leq 1.5\sigma_0$	$J = 5J_0$ $\sigma = 1.48\sigma_0$	$V = 0.44$ $T = 239.98$	$\frac{\ f_m\ }{\ f_m\ } = 0.04$

7.3.4 Case study: Exhaust system

Next we consider engine exhaust-washed structure, used in a low observable supersonic aircraft; this was first studied by J. Deaton [1]. Due to low radar observability requirement, engine and exhaust system are buried inside the aircraft. Because of the space restriction, the exhaust system is supported at the aircraft skins; thermal expansion is therefore limited. In order to reduce infrared detectability, hot exhaust gas is cooled within the exhaust duct.

A simplified exhaust system is illustrated in Figure 64 where the structure is fixed at left and right ends, and at the supporting structures. A temperature at intake is $T = 400^{\circ}\text{C}$ and cooled down to $T = 100^{\circ}\text{C}$ at output nozzle. For FEA, the domain is meshed with 54,080 hexahedral elements, resulting in 208,374 DOF.

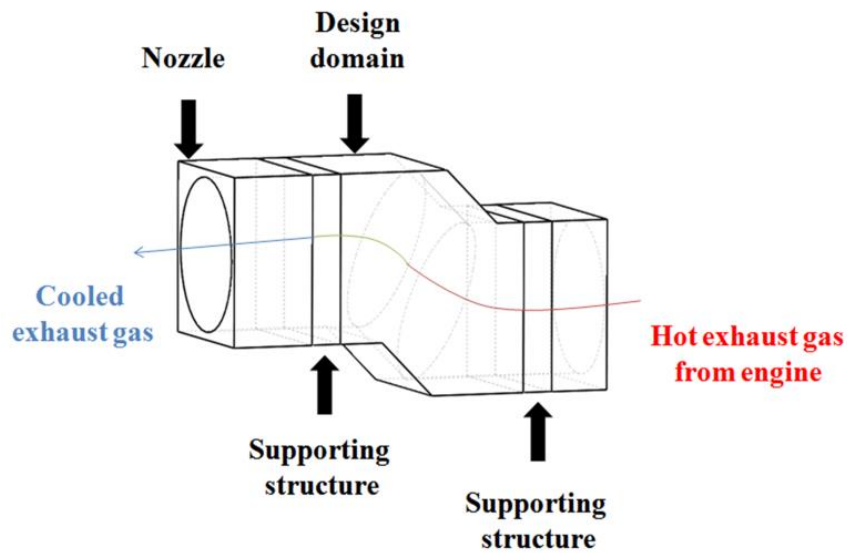


Figure 64: Conceptual exhaust system.

The dimensions of the exhaust duct are illustrated in Figure 65.

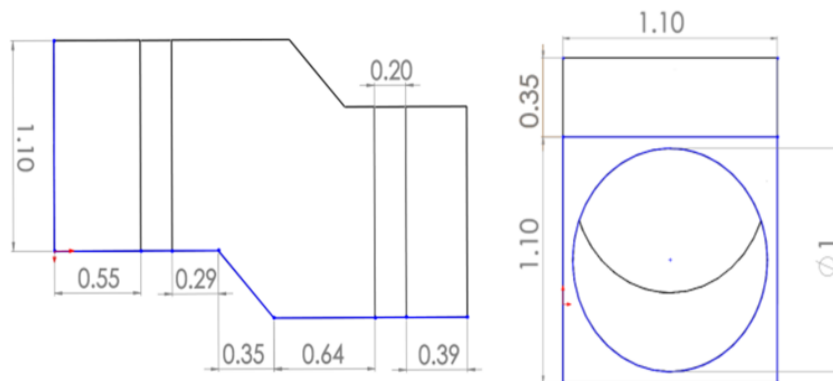


Figure 65: Dimensions of the exhaust system (unit: m).

The specific thermo-elastic topology optimization problem solved here is:

$$\begin{aligned}
& \underset{\Omega \subset D}{\text{Min}} |\Omega| \\
& J \leq 1.5J_0 \\
& \sigma \leq 1.5\sigma_0 \\
& \text{subject to} \\
& Kd = f_{st} + f_{th} \\
& K_t t = q
\end{aligned} \tag{128}$$

The final topology is illustrated in Figure 66. Optimization results are summarized in Table 24. On termination, the compliance constraint is active and the maximum p-norm stress is reduced.

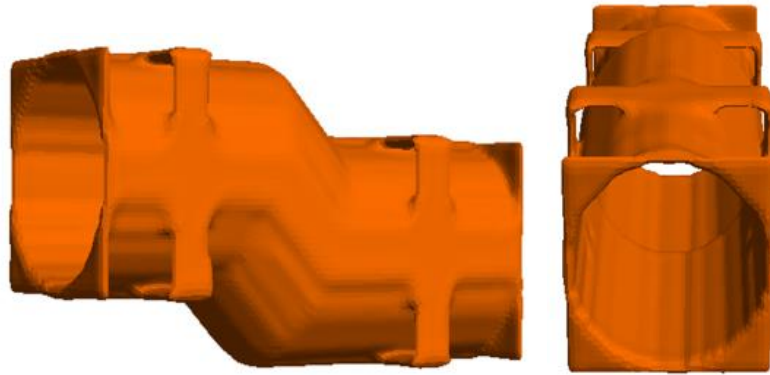


Figure 66: Side view (left) and front view (right) of the optimized exhaust

Table 24: Constraints and results for problem in Equation (128).

Initial Constraints	Final Results	Final volume & time (s)
$J \leq 1.5J_0$ $\sigma \leq 1.5\sigma_0$	$J = 1.50J_0$ $\sigma = 0.83\sigma_0$	$v = 0.46$ $T = 531.4$

The main contribution of this chapter is a comprehensive method for thermo-elastic topology optimization problems. Under two different thermal scenarios, the change in compliance and stress due to topological change are captured. Both formulations exploit the concept of discrete topological sensitivity; thus material parameterization is not required. Augmented Lagrangian

method was used for multi-constrained thermo-elastic topology optimization. AF-DCG method was implemented for FEA acceleration.

As the numerical experiments reveal, the impact of both uniform temperature variations and spatially thermal gradients on the final topologies can be significant for certain problems. Future work will focus on including other constraints including buckling and eigen-modes.

8 APPLICATION: BUCKLING TOPOLOGY OPTIMIZATION

8.1 Introduction to Thermo-Elastic Buckling

This chapter focuses on topology optimization of structures subject to a compressive load in a thermal environment. Such problems are important, for example, in aerospace, where structures are prone to thermally induced buckling.

Popular strategies for thermo-elastic topology optimization include Solid Isotropic Material with Penalization (SIMP) and Rational Approximation of Material Properties (RAMP). However, since both methods fundamentally rely on material parameterization, they are often challenged by: (1) pseudo buckling modes in low-density regions, and (2) ill-conditioned stiffness matrices.

To overcome these, we consider here an alternate level-set approach that relies discrete topological sensitivity. Buckling sensitivity analysis is carried out via direct and adjoint formulations. Augmented Lagrangian method is then used to solve a buckling constrained compliance minimization problem. Finally, 3D numerical experiments illustrate the efficiency of the proposed method.

The focus of this chapter is on thermo-elastic buckling topology optimization where structures are restrained and subject to thermal loading. For example, consider the wing rib structure of a high Mach supersonic aircraft in Figure 67. During rocket boost phase when the aircraft is subject to rapid acceleration and significant thermal gradients, its surface temperature can be as high as $1650^{\circ}C$. Since the rib structures are welded onto wing skins, uneven thermal heating may induce significant compressive stresses to cause buckling. Therefore, a primary goal

for structural designs of airplanes operating in extreme thermal environment is to provide a light-weight structure with thermal buckling resistance.

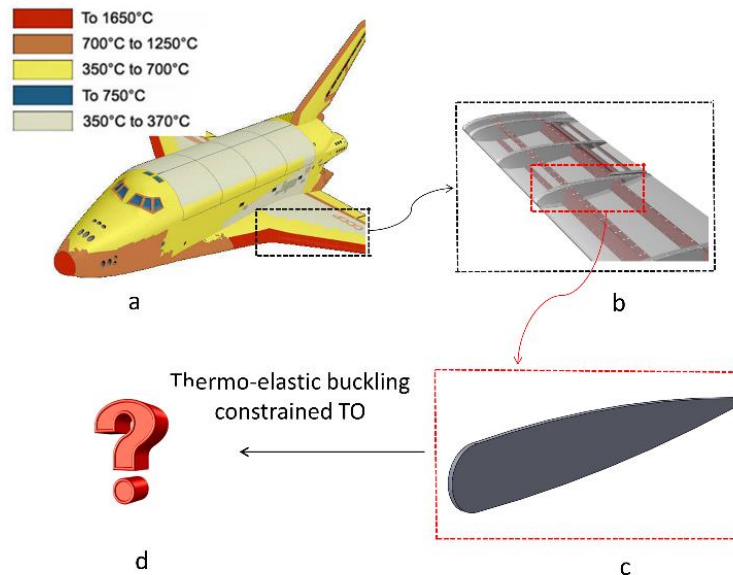


Figure 67: (a) aircraft operating in high temperature⁶; (b) wing rib structures⁷; (c) design space of rib structure; (d) optimized rib structure.

However, unlike in pure elasticity, for thermo-elastic problems, the displacements are computed after accounting for the additional thermal load. This poses both theoretical and computational challenges in topology optimization discussed later in the chapter.

8.2 Literature Review of Buckling Constrained Topology Optimization

Buckling problems mostly occur in thin-walled structures [142]. Buckling constrained topology optimization problems were originally studied by ground structure method, while more recent methods are continuum based and can be classified into the following types: Solid

⁶ The figure is downloaded from www.ae.metu.edu.tr.

⁷ The figure is downloaded from www.buran-energia.com.

Isotropic Material with Penalization (SIMP), evolutionary structural optimization (ESO) and level-set. In following sections, we review previous publications based on their methods.

Ground structure approach

Ground structure approach is the classic method for optimizing the topology of truss systems. In this approach, a network of potential truss members is first prescribed in a design domain. A size optimization is carried out on each truss member until the cross-section areas of non-optimal trusses approach zero and can therefore be removed [5].

However, including buckling constraint into truss topology optimization is non-trivial. The member forces in each truss have to satisfy functions which discontinuously depend on design variables [143]. Traditional optimizers face difficulty in solving such problems. In [143], the author argued that including slenderness constraints into buckling problems can guarantee solution existence and simplify the process. In [144], by using a smooth procedure to remove singular optimum from original formulation, size optimization was made more efficient. In a recent publication [145], the author used a mixed variable formulation to linearize buckling constraints in each ground structure member.

Solid Isotropic Material with Penalization (SIMP)

In continuum topology optimization, the most popular method is Solid Isotropic Material with Penalization (SIMP). Its primary advantages are that it is well understood, robust and easy to implement [7]. Indeed, SIMP has been applied to a variety of topology optimization problems ranging from fluids to non-linear structural mechanics.

In buckling constrained topology optimization, the appearance of pseudo buckling modes in low-density regions can pose problems. In [146], a buckling load criterion was introduced to

ignore the geometric stiffness matrix of the elements whose density and principal stress were smaller than a prescribed value. In [147], the author argued such cut-off methods may abruptly change the objective function and sensitivity field, leading to oscillation. Instead, the author suggested using different penalization scheme for stiffness matrix and geometric stiffness matrix. Although the author in [148] suggested it was difficult to select an appropriate penalty scheme for accurate calculation of buckling load factor, the proposed approach by [147] became a popular formulation for many researchers [149]. In a recent publication [150], a new approach to remove pseudo buckling mode was based on eigen-value shift, and pseudo mode identification.

ESO

ESO [8] is an alternate topology optimization formulation where finite elements are gradually removed based on their significance with respect to the objective function. BESO [11] addresses some of the limitations of ESO by permitting insertion of elements. In [151], a modified ESO method was proposed to maximize buckling load factor. The sensitivity of the lowest eigen-value was first derived, and the buckling eigen-value maximization was then formulated by suitably selecting the optimization criteria.

Level-Set

The level-set strategy is gaining popularity for solving topology optimization problems for a main reason that the boundary is well-defined at all times, and some of the challenges associated with low-density regions do not arise; see [14] for a recent review and comparison of level-set based methods in structural topology optimization. In [134], a simplified buckling sensitivity field was incorporated into a level-set based framework to accelerate large-scale topology optimization process, however thermally induced buckling was not considered.

Research gap

From the above literature review, one can conclude that there has been significant research devoted to solving buckling constrained topology optimization problems. However, one can identify the following research gaps:

Although thermal buckling is of significant importance to stability analysis of structures under thermal gradients, there is very little research on buckling constrained thermo-elastic topology optimization.

Computing buckling topological sensitivity is expensive, and efficient approaches are needed.

Prior publications have validated their algorithms on simple bench mark examples for the sake of computational expense. Extension to large scale 3D problems is lacking.

Proposed

In this paper, we consider the topological level-set method proposed in [134] for pure-elastic buckling problems, and extend this to thermo-elastic buckling through two distinct approaches: direct and adjoint methods. In the topological level-set method, instead of relying on the Hamilton-Jacobi equations for level-set propagation [13], fixed-point iteration is exploited to advance the topology [111].

8.2 Buckling Sensitivity Analysis

In this section, two approaches are used to calculate the sensitivity of linear buckling load factor. The linear buckling load factor can be calculated from a well-known formulation [142]:

$$(K + \lambda K_\sigma)v = 0 \tag{129}$$

Where

K_σ : Global geometric stiffness matrix
 v : Buckling mode vector
 λ : Linear buckling load factor

In Equation (129), the global geometric stiffness matrix is defined via the assembly:

$$K_\sigma = \sum_{e=1}^N [k_\sigma]_e \quad (130)$$

where N is the number of finite elements and the elemental geometric stiffness matrix are defined as:

$$[k_\sigma]_e = \int_{\Omega_e} G^T S G dv \quad (131)$$

where G is obtained from shape functions by appropriate differentiation and reordering [142]. The matrix S can be defined as:

$$S = \begin{bmatrix} s & 0 & 0 \\ 0 & s & 0 \\ 0 & 0 & s \end{bmatrix} \quad (132)$$

Where

$$s = \begin{bmatrix} \sigma_x & \tau_{xy} & \tau_{xz} \\ \tau_{xy} & \sigma_y & \tau_{yz} \\ \tau_{xz} & \tau_{yz} & \sigma_z \end{bmatrix} \quad (133)$$

In addition, the stress in an element can be defined as:

$$[\sigma]_e = [\sigma_x, \sigma_y, \sigma_z, \tau_{xy}, \tau_{xz}, \tau_{yz}]^T \quad (134)$$

It is clear that in Equation (130) the geometric stiffness matrix K_σ is a function of stress (σ) which depends on the topological design variable, while the stiffness matrix (K), buckling load factor (λ) and buckling mode vector (v) are explicitly dependent on design variables. It is also noted since the temperature field is uniformly elevated to a prescribed value, the temperature field (t) is not dependent on those quantities.

Let Q be any quantity of interest in an optimization problem. The sensitivity of Q with respect to any design variable is defined as:

$$Q' = \frac{\partial Q}{\partial x} \quad (135)$$

The derivatives of the global stiffness matrix and geometric stiffness matrix can be expressed as:

$$K' \equiv \frac{\partial K}{\partial x} \quad (136)$$

$$K'_\sigma \equiv \frac{\partial K_\sigma}{\partial \sigma} \sigma' \quad (137)$$

8.3.1 Direct method

Multiplying the buckling mode vector (v^T) on both sides of Equation (129), and taking the derivative with respect to design variable, we have:

$$2v^T(K + \lambda K_\sigma)v + v^T(K' + \lambda K'_\sigma + \lambda' K_\sigma)v = 0 \quad (138)$$

Due to Equation (129), the first term in Equation (138) vanishes. Reordering terms in Equation (138), we have the sensitivity of the linear buckling load factor as:

$$\lambda' = -\frac{\nu^T (K' + \lambda K'_\sigma) \nu}{\nu^T K_\sigma \nu} \quad (139)$$

A simple method to calculate (K'_σ) is to use finite difference, i.e., calculate the effect of removing a single element on the global geometric stiffness matrix. Obviously, this method is too expensive for topology optimization ... the computational cost will increase significantly with the number of elements. Alternatively, we can employ a more direct and efficient approach.

The term on the right hand side of Equation (137) can be written as the summation of all finite elements:

$$\frac{\partial K_\sigma}{\partial \sigma} \sigma' = \sum_{j=1}^N \left(\frac{\partial K_\sigma}{\partial \sigma_j} \sigma'_j \right) \quad (140)$$

where N is the number of all finite elements. In words, the sensitivity of global geometric stiffness matrix equals the summation of the combinational effect between sensitivity of global geometric stiffness matrix with respect to each finite element stress and the sensitivity of the elemental stress.

For a specific j -element in Equation (140), reuse the summation rule as Equation (140):

$$\frac{\partial K_\sigma}{\partial \sigma_j} \sigma'_j = \sum_{k=1}^6 \left(\frac{\partial K_\sigma}{\partial \sigma_{jk}} \sigma'_{jk} \right) \quad (141)$$

where the summation refers to the six elemental stress components in Equation (134).

Further:

$$\frac{\partial K_\sigma}{\partial \sigma_{jk}} = \frac{\partial \int_{\Omega_j} G^T S G dv + \sum_{i=0}^{others} \left(\int_{\Omega_i} G^T S G dv \right)}{\partial \sigma_{jk}} \quad (142)$$

Since the geometric stiffness matrices in other elements are not explicitly dependent on the stress in j-element (σ_j^k), the second term in numerator of Equation (142) can be dropped:

$$\frac{\partial K_\sigma}{\partial \sigma_j^k} = \frac{\partial \int_{\Omega_j} G^T S G dv}{\partial \sigma_j^k} = \int_{\Omega_j} G^T \frac{\partial S}{\partial \sigma_k} G dv \quad (143)$$

Where

$$\frac{\partial S}{\partial \sigma_k} = \begin{bmatrix} \frac{\partial s}{\partial \sigma_k} & 0 & 0 \\ 0 & \frac{\partial s}{\partial \sigma_k} & 0 \\ 0 & 0 & \frac{\partial s}{\partial \sigma_k} \end{bmatrix} \quad (144)$$

For the six stress components in Equation (134), it is easy to calculate their matrices elements in Equation (144). For example, when $k = 1$, we have:

$$\frac{\partial s}{\partial \sigma_1} = \begin{bmatrix} 1 & 0 & 0 \\ 0 & 0 & 0 \\ 0 & 0 & 0 \end{bmatrix} \quad (145)$$

The term ($\frac{\partial \sigma_j^k}{\partial x}$) in Equation (141) can be derived as follows. Rewrite Equation (17) for the j-element:

$$\sigma_j = DBd_j - D\varepsilon_j^{th} \quad (146)$$

where the elemental thermal strain (ε_j^{th}) can be calculated in Equation (16). Clearly, it is independent of design variable (x). Take derivative of each term in Equation (146), we have:

$$\sigma'_j = DBd'_j + DBd'_j \quad (147)$$

We can calculate the term (d'_j) in Equation (147) in the following manner. Taking derivative of the static equilibrium equation in Equation (14):

$$K'd + Kd' = f'_{th} \quad (148)$$

where the structural force is assumed independent of design variable. Reordering terms, we have

$$d' = K^{-1}(f'_{th} - K'd) \quad (149)$$

The elemental displacement sensitivity in j-element (d'_j) can be directly obtained from Equation (149).

8.3.2 Adjoint method

An efficient way to compute the sensitivity field of buckling load factor is by adding adjoint variables and constraints into Equation (129) [152]. By carefully selecting the adjoint variables, the computational expensive terms (σ'_j) and (d'_j) in Equation (147) and (149) are expected to drop.

Multiplying buckling mode vector (v^T) on both sides of Equation (129) and augmenting with two constraints multiplied by two adjoint variables (μ) and (w) , we have:

$$v^T(K + \lambda K_\sigma)v + \mu^T[\sigma - Yd + Z\varepsilon_{th}] + w^T(f - Kd) = 0 \quad (150)$$

where the matrix (Y) and (Z) relate displacement and thermal strain to stress, respectively.

$$Y = \sum_{j=1}^N [DB]_j \quad (151)$$

$$Z = \sum_{j=1}^N [D]_j \quad (152)$$

In Equation (150), the adjoint μ link the stress to deformation, and the adjoint w link the deformation to external load. Then, taking derivative of Equation (150) and simplifying terms, we get:

$$\begin{aligned} v^T (K' + \lambda \frac{\partial K_\sigma}{\partial \sigma} \sigma' + \lambda' K_\sigma) v + \mu^T (\sigma' - Y' d - Y d' + Z' \varepsilon_{th}) + \\ w^T (f' - K' d - K d') = 0 \end{aligned} \quad (153)$$

The first adjoint (μ) is chosen such that the terms with (σ') can be dropped from Equation (153):

$$\lambda v^T \frac{\partial K_\sigma}{\partial \sigma} \sigma' v + \mu^T \sigma' = 0 \quad (154)$$

After factoring and rearranging terms, we have:

$$\mu^T = -\lambda v^T \frac{\partial K_\sigma}{\partial \sigma} v \quad (155)$$

where the term $\frac{\partial K_\sigma}{\partial \sigma}$ is the assembly of all elemental sensitivities, each containing six components.

$$\frac{\partial K_\sigma}{\partial \sigma} = \sum_{j=1}^N \sum_{k=1}^6 \frac{\partial K_\sigma}{\partial \sigma_j^k} \quad (156)$$

where the term $\frac{\partial K_\sigma}{\partial \sigma_j^k}$ can be calculated from Equation (143).

Equation (153) simplifies to:

$$\begin{aligned} & \nu^T (K' + \lambda' K_\sigma) \nu + \mu^T (-Y' d - Y d' + Z' \varepsilon_{th}) + \\ & w^T (f' - K' d - K d') = 0 \end{aligned} \quad (157)$$

The second adjoint w is chosen such that the terms containing d' can be cancelled out:

$$\mu^T Y d' + w^T K d' = 0 \quad (158)$$

After rearranging terms, we have:

$$w^T = -\mu^T Y K^{-1} \quad (159)$$

Therefore, the sensitivity of the buckling load factor can be expressed as:

$$\lambda' = -\frac{1}{\nu^T K_\sigma \nu} (\nu^T K' \nu + \mu^T Z' \varepsilon_{th} - \mu^T Y' d + w^T f' - w^T K' d) \quad (160)$$

8.3.3 Discrete element sensitivity approximation

The last step is to compute the sensitivity of the global matrices in Equation (139) and (160), i.e., K' , K_σ^x , Y' and Z' . If pseudo-density parameterization is used (e.g. SIMP), then the sensitivities can be computed via their respective material interpolation scheme [53]. One of the challenges with this approach is that the stiffness matrices will exhibit large condition numbers due to the elements with intermediate densities. This will result in slow convergence of iterative solvers.

Here, we employ a discrete approximation, i.e., the sensitivities of the stiffness matrices are computed at the center of each element [153], i.e.:

$$K' \equiv [K_e] \quad (161)$$

$$Y' \equiv [DB] \quad (162)$$

$$Z' \equiv [D] \quad (163)$$

and then smoothened.

8.4 Algorithm of Constrained Thermo-Elastic Buckling Topology Optimization

The overall algorithm proceeds as follows:

- 1) Start the optimization at a volume fraction of 1.0. The ‘current volume fraction’ v is set to 1.0, and ‘volume decrement’ Δv , is set to 0.025.
- 2) Solve the thermo-structural FEA problem in Equation (13) and the stress are extracted at the center of each element by Equation (17).
- 3) Solve the linear buckling eigen-value problem in Equation (129). The buckling topological sensitivity field is computed at the center of each element and locally smoothened with neighboring elements by either the direct method in Equation (139) or adjoint method in Equation (160).
- 4) Use augmented Lagrangian formulation to combine the sensitivity fields of the objective function and constraints in Equation (48).
- 5) Decrement volume fraction by (Δv) and trace the Pareto curve based on the sensitivity of the augmented Lagrangian equation. The compliance is computed over each new topology. If the compliance has converged, then the optimization moves to the next step, else it returns to step 2.
- 6) The current volume fraction is set to ($v - \Delta v$), and the optimization returns to step-2, until the final volume fraction is reached or the constraints are violated.

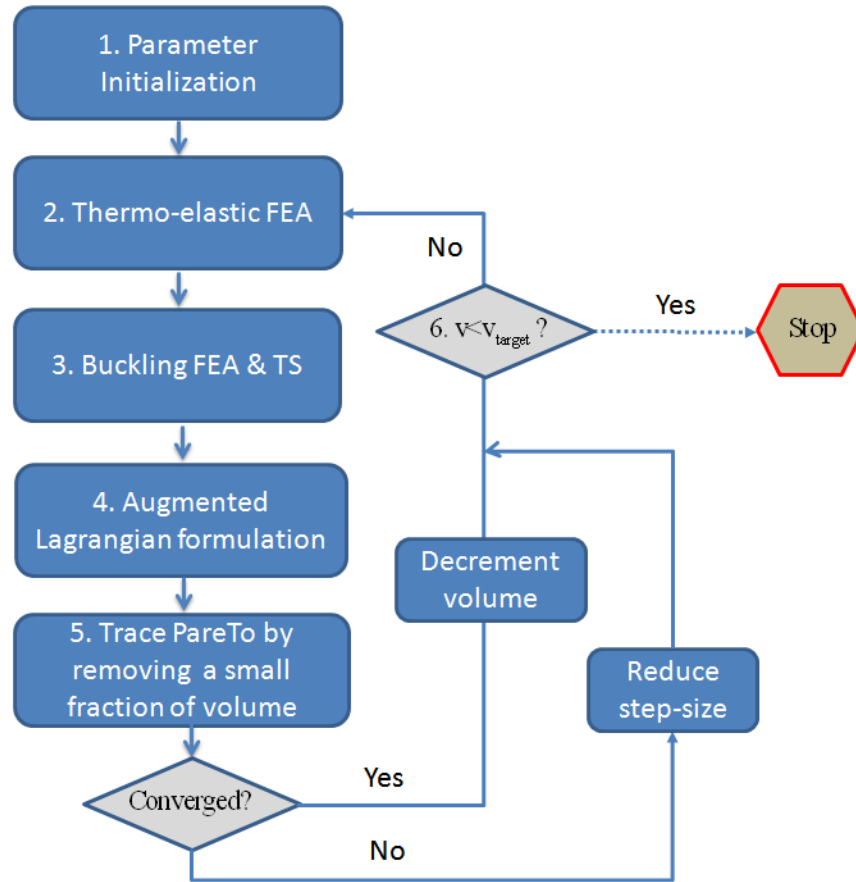


Figure 68: An overview of the algorithm.

8.5 Numerical Experiments

In this Section, we demonstrate the proposed method through numerical experiments. The default parameters are as follows:

- A thermal load is applied by increasing the temperature uniformly with respect to the reference temperature ($T_0 = 25^\circ C$).
- Hexahedral elements are used for 3D finite element analysis.

8.5.1 Benchmark example

The first experiment involves the classic thin plate structure which was previously studied in [134]. A thin plate is a flat sheet of material whose thickness is much smaller than other dimensions. A thin plate can support loads of significant magnitude in the direction of both normal to its surface and in-plane. However, a moderate compressive in-plane load may cause the plate to buckle whose magnitude can be much smaller than material yield strength. Since a buckled structure is considered unstable, it is important to consider buckling constraints in design process. In this section, a 3D thin column structure is optimized subject to buckling constraint with a uniformly elevated temperature.

The structure material is assumed to be steel, i.e., the elastic modulus is $E = 2e11 Pa$, the Poisson's ratio is $\nu = 0.3$ and the coefficient of thermal expansion is $\alpha = 1.1e-5 / ^\circ C$. As illustrated in Figure 69a, the structure is clamped at bottom and a compressive load of $F = 1.0e5 N$ is applied at the center of the top edge; the structure is also subject to a homogeneous temperature elevation of $\Delta T = 150^\circ C$. Note that the 3D column will buckle out of the plane as illustrated in Figure 69c where the thickness is 0.01m.

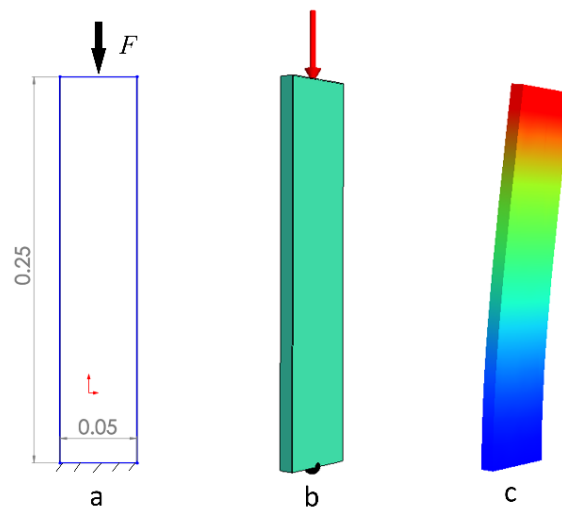


Figure 69: (a) A thin column, (b) CAD model, and (c) buckling mode.

The generic topology optimization problem considered in this section can be posted as:

$$\begin{aligned}
 & \underset{\Omega \subset D}{\text{Min}} \quad |\Omega| \\
 & J \leq 2.5J_0 \\
 & P \geq 0.6P_0 \\
 & \text{subject to} \\
 & Kd = f_{st} + f_{th} \\
 & \Delta T = 150^\circ C
 \end{aligned} \tag{164}$$

In words, we search for the optimal design whose final compliance should be no larger than 2.5 times its initial value while the final buckling load factor should be larger than or equal to 60% of its initial value. (We also consider special instances below where buckling is neglected.)

In order to test the direct and adjoint methods, we use different meshes and compare their computational time as in Figure 70. It is clear the proposed adjoint method is significantly more efficient. Since the inverse of the global stiffness matrix (K^{-1}) has to be computed for every element as illustrated in Equation (140), the computing time of the direct method increases exponentially with the number of finite elements.

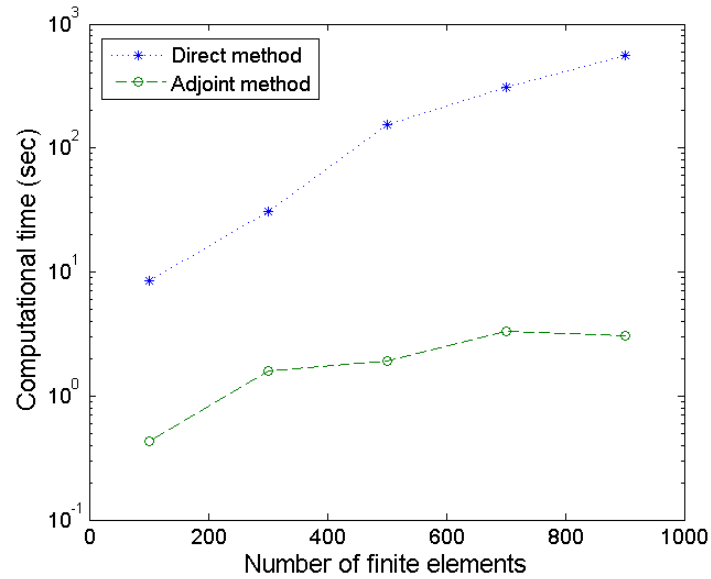


Figure 70: Comparison of computational time between direct and adjoint method

Due to its simplicity and efficiency, the adjoint method is preferred henceforth. If we use 30,000 elements (i.e., 104,832 degrees of freedom (DOF)) to mesh the design domain. We consider three different scenarios: (a) buckling constraint and temperature elevation are neglected, see Figure 71(a); (b) buckling constraint is neglected but temperature elevation is included, see Figure 71(b); and finally (c) where both buckling constraint and temperature elevation are included, see Figure 71(c).

The impacts of temperature change and buckling constraint are clearly observable.

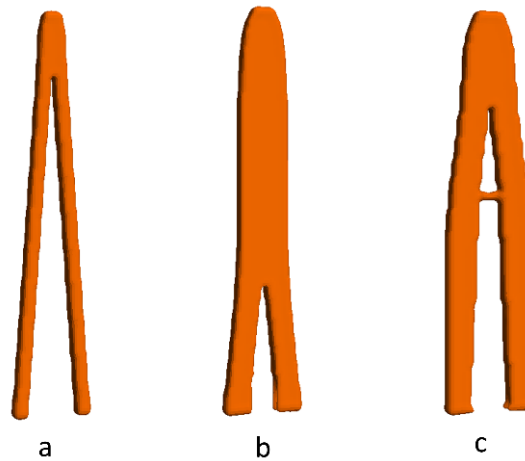


Figure 71: (a) compliance constrained elastic topology optimization; (b) buckling-compliance constrained elastic topology optimization; (c) buckling-compliance constrained thermal topology optimization from the adjoint method.

The final volume fractions and constraints are summarized in Table 25 where the active constraints are emphasized with a ‘box’.

Table 25: Constraints and results for problem in Figure 71

Topology	Initial Constraints	Final Constraints	Volume & time (sec)
Figure 71(a)	$J \leq 2.5J_0$	$J = 2.50J_0$	$v = 0.33$ $T = 67.32$
Figure 71(b)	$J \leq 2.5J_0$ $P \geq 0.6P_0$	$J = 1.48J_0$ $P = 0.60P_0$	$v = 0.59$ $T = 145.68$
Figure 71(c)	$J \leq 2.5J_0$ $P \geq 0.6P_0$ $\Delta T = 150^\circ C$	$J = 2.50J_0$ $P = 0.91P_0$ $\Delta T = 150^\circ C$	$v = 0.57$ $T = 197.03$

For the specific case of Figure 71(c), the iteration history with evolving topologies are illustrated in Figure 72 where the values of the compliance and buckling load factor are scaled to unit according to the initial value at volume fraction of 1.0. Observe that with the decrement of

volume fraction from 1.0, the compliance monotonously increases, while the buckling load factor generally decreases. The non-monotonous feature of the buckling load factor curve in Figure 72 is due to its inherent complexity as stated in Equation (139) and Equation (160).

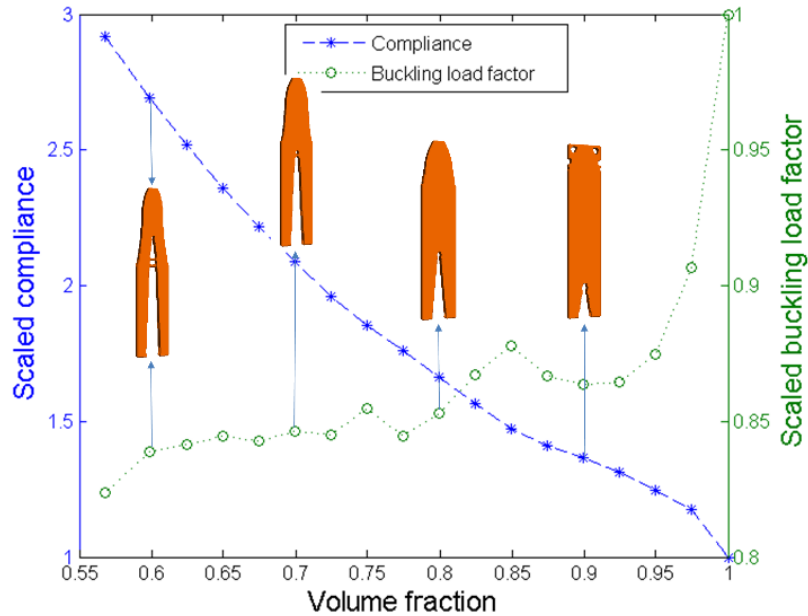


Figure 72: Iteration history of the adjoint approach.

In order to study the effect of temperature variations on the optimization, five thermal conditions are considered ($\Delta T = 25^\circ\text{C}, 50^\circ\text{C}, 75^\circ\text{C}, 100^\circ\text{C}, 125^\circ\text{C}$). Combining with the 2 previously studied cases in Figure 71 (a) and (b), we can plot the iteration history of compliance (in Figure 73) and buckling load factor (in Figure 74). Both plots are scaled to show their relative evolving values.

There are several observations: First, optimizations with temperature change of $\Delta T = 0^\circ\text{C}, 25^\circ\text{C}, 50^\circ\text{C}$ are terminated due to pre-set buckling constraints ($P \geq 0.6P_0$); optimizations with $\Delta T = 75^\circ\text{C}, 100^\circ\text{C}, 125^\circ\text{C}, 150^\circ\text{C}$ are terminated due to compliance constraint ($J \leq 2.5J_0$). Second, in Figure 73, structures with higher temperature variations have

lower compliance value. One possible reason is that compressive external load eases thermal expansions. Third, in Figure 74, structures subject to severe thermal gradients tend to have lower buckling load factor. It means buckling is more likely to occur in a hotter environment.

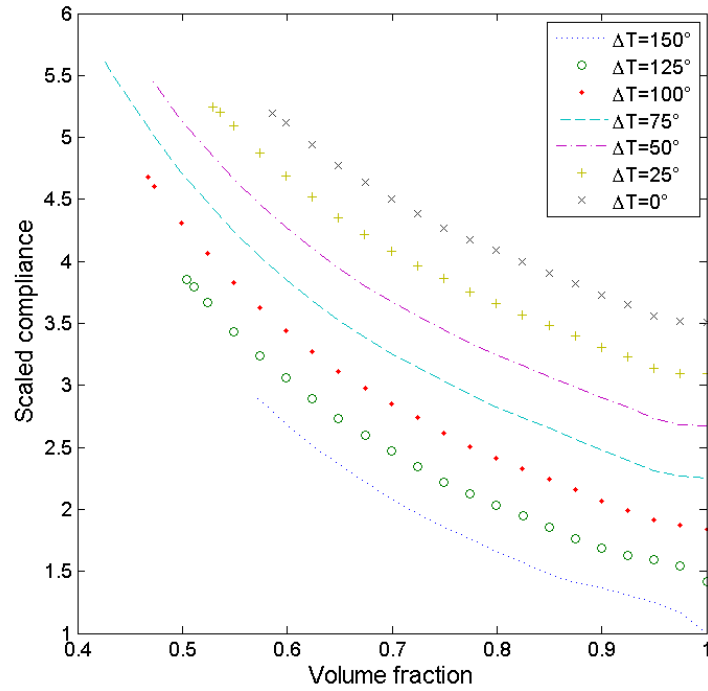


Figure 73: Iteration history of compliance for different temperature rises.

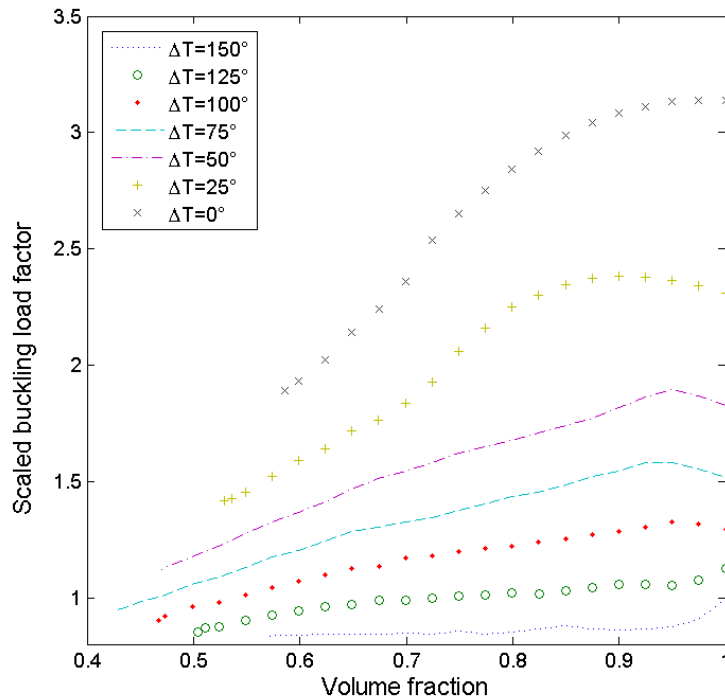


Figure 74: Iteration history of buckling load factor for different temperature rises.

8.5.2 Industrial application: airplane wing rib structure

The purpose of this experiment is to demonstrate the robustness of the proposed adjoint method for optimizing the airplane wing rib structure.

In wing structures, to maintain wing contours in chord-wise direction and to shorten the length of longitudinal wing stringers, ribs are used as internal supporting units as shown in Figure 75 [154].

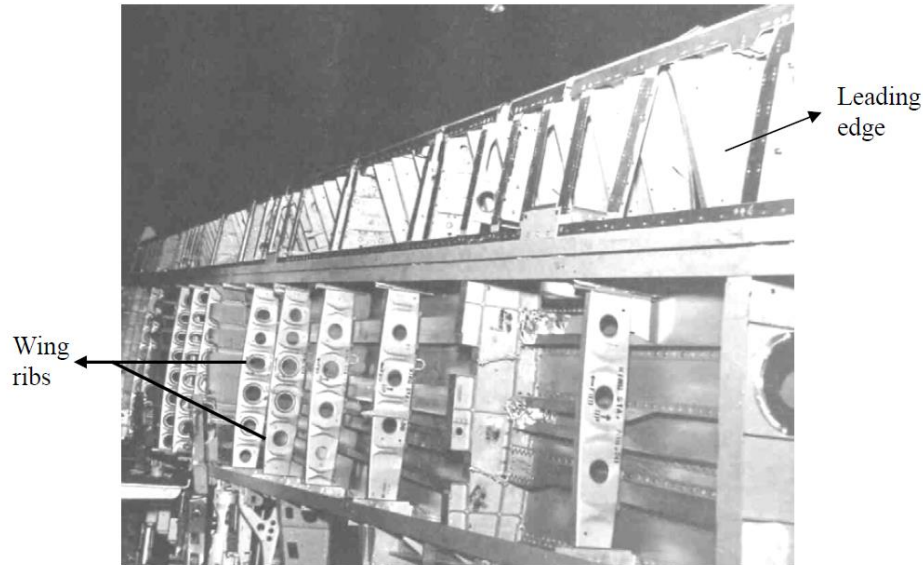


Figure 75: Wing rib structures with lower skin uninstalled [154].

The rib structure consists of three distinct sections as shown in Figure 76: the leading edge portion, the wing box portion and trailing edge. In the leading edge, lightening holes are often introduced for mass reduction and accessibility of wiring and pipe lines. Horizontal stiffeners are also used to prevent buckling. In the wing box portion, horizontal and vertical beads are used both to stiffen the structure and to prevent buckling. Trusses are heavily used in trailing edge portion. The rib can be welded, riveted or glued onto wing skins. Such assembly configuration can easily conduct heat from hot skin (shown in Figure 67) to the rib structures. Deduced thermal compressive stress significantly increases the buckling failure risk.

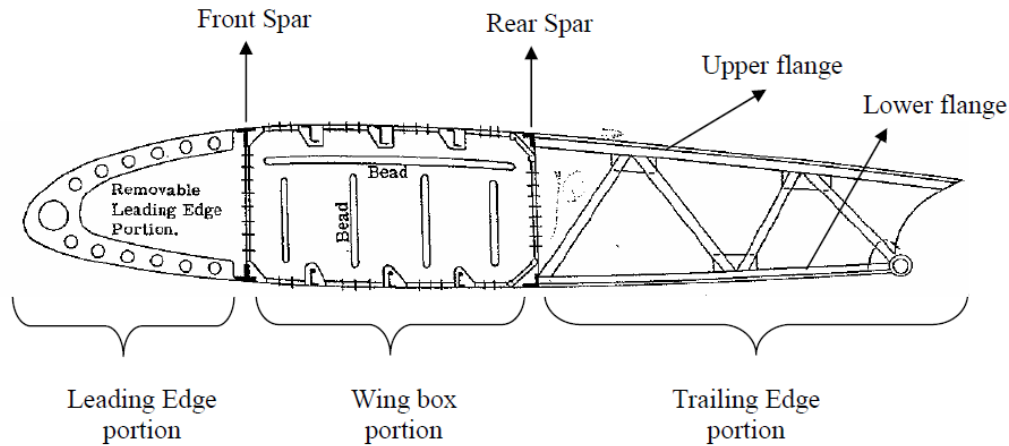


Figure 76: Wing rib construction [154].

Lightening holes and stiffening beads are often designed based on experience, and may not be optimal. In this section, the proposed thermo-elastic topology optimization method is used for optimizing both leading-edge portion and wing-box portion.

Leading-edge portion

During flight, the wing ribs are subject to three types of loads: (a) aerodynamic lift and drag forces, (b) concentrated forces from its connection with landing gears and fuselage, and (c) gravitational body force [154]. In this experiment, only the dominating aerodynamic forces are considered for simplicity. With speed limit up to 24 Mach, the lift and drag pressure on a supersonic aircraft (e.g. space shuttle) can be as high as $10^8(N/m^2)$, while the surface temperature can be as high as $1650^{\circ}C$. Although thermally protected [155], the ribs underneath the skin can still reach $170^{\circ}C \sim 270^{\circ}C$ [155].

As shown in Figure 35, the leading edge is assumed to be fixed at the right edge, and loaded with a drag pressure of $146MPa$ on the top edge and a lift pressure of $430MPa$ at the bottom. The entire structure is subject to an increase in temperature of $\Delta T = 270^{\circ}C$. The material is assumed to be titanium alloy [156] (online document shows the space shuttle is made of this

alloy and aluminum) with an elastic modulus of $E = 111 \text{ GPa}$, Poisson's ratio of $\nu = 0.33$ and coefficient of thermal expansion of $\alpha = 6.0e-6 / ^\circ\text{C}$.

For FEA, 294,670 hexahedral elements are used to discretize the design domain, resulting in 972,192 DOF. The optimization problem is set as follows:

$$\begin{aligned}
 & \underset{\Omega \subset D}{\text{Min}} \quad |\Omega| \\
 & J \leq 1.5J_0 \\
 & P \geq 0.4P_0 \\
 & \text{subject to} \\
 & Kd = f_{st} + f_{th} \\
 & \Delta T = 270^\circ\text{C}
 \end{aligned} \tag{165}$$

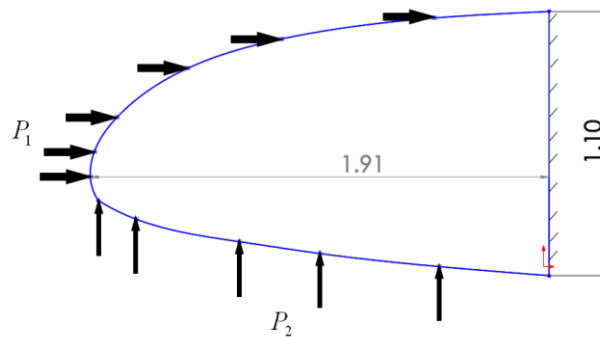


Figure 77: Leading-edge with a thickness of 0.1m, and applied boundary conditions (units are in meters).

In words, the objective is to find the optimal topology with the minimal volume and its compliance is no more than 1.5 times the initial compliance, and its buckling load factor is no less than 40% of original value.

To illustrate the impact of thermal load, we also solve the above problem by neglecting the temperature increase. The resulting topologies are illustrated in Figure 78. It can be observed that (we have to redo the experiments by neglecting the volume constraint: volume fraction constraint is not active here): (1) compared with elastic optimization result in Figure 78(b), the thermo-

elastic optimization (Figure 78(a)) is terminated due to the same buckling constraint but at a higher volume fraction. It indicates a temperature rise may lead to buckling instability in a structure which is stable in regular room temperature. (2) since compliance constraint outweighs buckling constraint, a Michell truss sub-structures are observed in the optimized results.

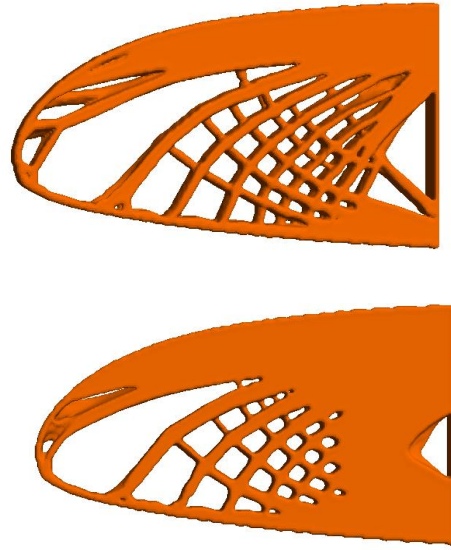


Figure 78: Optimal designs for the rib leading-edge portion: (a) With buckling constraint but no thermal load; (b) With buckling constraint and thermal load.

The numerical results are summarized in Table 26.

Table 26: Constraints and results for problem in Figure 78

Topology	Initial Constraints	Final Constraints	Volume & time
Figure 78(a)	$J \leq 1.5J_0$ $P \geq 0.4P_0$	$J = 1.44J_0$ $P = 0.4P_0$	$v = 0.52$ $T = 42 \text{ min}$
Figure 78(b)	$J \leq 1.5J_0$ $P \geq 0.4P_0$ $\Delta T = 270^\circ C$	$J = 1.17J_0$ $P = 0.4P_0$ $\Delta T = 270^\circ C$	$v = 0.70$ $T = 32 \text{ min}$

Wing-box portion

Next, we consider optimization of the wing-box portion as shown in Figure 79 where both left and right ends are fixed, a lift pressure of $430MPa$ is loaded at the bottom, and a shear drag pressure of $146MPa$ is exerted on the top edge. 308,480 finite elements are used to discretize the design domain, leading to 1,022,328 DOF. The temperature rise is assumed to be $\Delta T = 170^\circ C$, lower than that on leading edge portion [155]. A similar topology optimization problem is solved in Equation (166) where the buckling constraint is set stricter due to the slim and thin geometry feature.

$$\begin{aligned}
 & \underset{\Omega \subset D}{Min} |\Omega| \\
 & J \leq 3.5J_0 \\
 & P \geq 0.5P_0 \\
 & \text{subject to} \\
 & Kd = f_{st} + f_{th} \\
 & \Delta T = 170^\circ C
 \end{aligned} \tag{166}$$

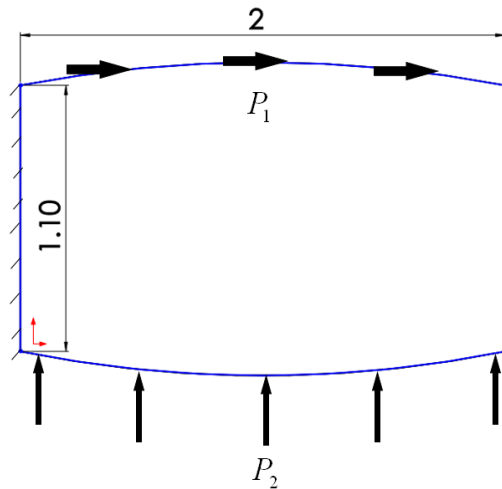


Figure 79: Rib wing-box portion with a thickness of 0.1 m, and applied FEA boundary conditions.

The resulting topologies are shown in Figure 80. The results are detailed in Table 26. While both the buckling-compliance constrained topology optimization (in Figure 80 (a)) and thermo-

elastic topology optimization (in Figure 80 (b)) are terminated due to buckling constraint, their optimized topologies have visibly bead-like features both vertically and horizontally.

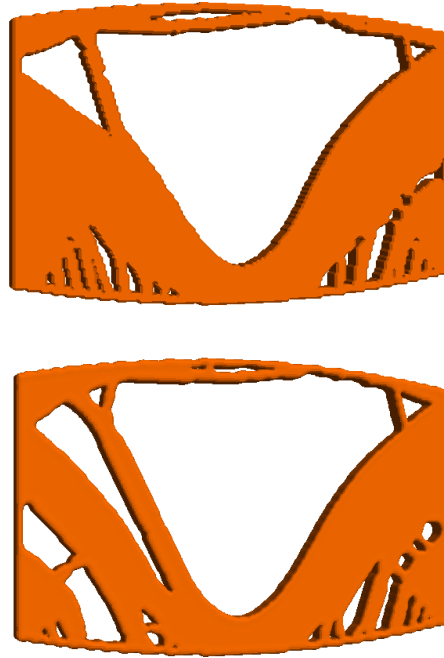


Figure 80: Optimal designs for the wing box portion: (a) With buckling constraint but no thermal load; (b) With buckling constraint and thermal load.

Table 27: Constraints and results for problem in Figure 80

Topology	Initial constraints	Final constraints	Volume & time
Figure 80(a)	$J \leq 3.5J_0$ $P \geq 0.5P_0$	$J = 2.19J_0$ $P = 0.5P_0$	$v = 0.53$ $T = 63\text{min}$
Figure 80(b)	$J \leq 3.5J_0$ $P \geq 0.5P_0$ $\Delta T = 170^\circ C$	$J = 2.32J_0$ $P = 0.5P_0$ $\Delta T = 170^\circ C$	$v = 0.51$ $T = 71\text{min}$

It can be seen the optimized designs (in Figure 78 and Figure 80) are non-trivial and quite different from the traditional design (in Figure 76). By employing the proposed topology

optimization method, the rib structure can be lightened by nearly 40% with a moderate compromise in stiffness and buckling resistance.

The main contribution of this chapter is a new method for buckling constrained thermo-elastic topology optimization algorithm. Two different formulations were presented and compared. Both formulations exploit the concept of topological sensitivity; thus material parameterization is not required. As the numerical experiments reveal, the impact of temperature variations on the final topologies can be significant for certain problems.

This chapter is limited to linear buckling analysis where the buckling is assumed to occur at bifurcation which assumes a reference stable configuration and an infinitesimally close buckled configuration are both possible at the same load [157]. Structure stiffness matrix is also assumed unchanged [157]. Although linear analysis is sufficient for simple thin plates and flat structures, non-linearity has to be considered in many situations where structures undergo significant pre-buckling rotations or have complex geometries. For buckling constrained topology optimization on such structures, non-linear analysis has to be considered.

9. CONCLUSION AND FUTURE WORK

9.1 Conclusion

The main contribution of this thesis is *an efficient formulation of large-scale multi-constrained thermo-elastic topological-sensitivity based level-set method for topology optimization.*

To establish this formulation, a series of novel algorithms were developed and numerous interesting results were found. They include:

- 1) Topological-sensitivity based level-set method was successfully extended from pure elasticity to thermo-elasticity. This method was proved efficient in solving theoretical and numerical challenges in thermal structural designs.
- 2) Augmented Lagrangian method was successfully implemented with the topological sensitivities of optimization objective and constraints. The augmented level-set method can therefore solve topology optimization problems with multiple constraints.
- 3) By combining augmented topological sensitivity fields of different simultaneously applied loads, the augmented level-set method was successful in handling topology optimization problems with multiple loads which often caused failures in density-based method.
- 4) By exploiting element-congruency, mesh voxelization and assembly-free deflated conjugate gradient method, the augmented level-set method was proved significantly efficient and robust in solving 3D large-scale topology optimization problems.
- 5) The thermo-elastic level-set method was successfully combined with augmented Lagrangian method. By the proposed methods, solving restrained thermal design problems with multiple constraints became available.

6) Various topological sensitivity fields were derived by discrete approximation method.

By using such sensitivity expressions, topology optimization can be extended to design scenarios where analytical sensitivity fields are infeasible.

This thesis bridged the gap for topology optimization between academic research and real world applications. For one thing, the studied cases were extended from 2D benchmark examples to 3D large-scale industry applications. For another, various constraints were taken into consideration during optimization, including mechanical properties (for example, compliance, stress, eigen-mode and buckling), algorithm implementations (soft and hard constraints) and manufacturing limitations (tool path constraints). The application on thermo-elastic buckling problem presented in Chapter 8 illustrated its potential in industry.

However, a number of open topics still require further investigations. A short description of each topic is given, as well as preliminary thoughts on accomplishing the work.

9.2 Future Work

9.2.1 Multi-level Topology Optimization

Micro-structural design can be viewed as a special application of topology optimization in lower dimension (for example, mesoscale). Such optimization process can create surprisingly unique macro-level (bulk scale) behaviors. A classic example is the negative Poisson ratio bolt design [158].

Based on the unique features of the micro-level topology optimization, a multi-level topology optimization may be proposed. In such method, the micro-level topology optimization is first carried out for obtaining desired materials properties, like Poisson ratio or shear modulus. Then, a macro-level topology optimization can be employed to optimize structural properties, like

compliance or stress. With desired properties at both micro and macro-levels, optimized structures would unsurprisingly own superior performance than traditional designs.

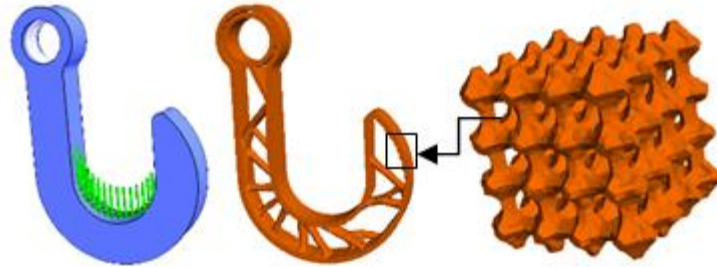


Figure 81: An optimal micro-structural design [159].

9.2.2 Nonlinear Topology Optimization

This research limited topology optimization within the scope of linearity. In other words, the proposed method assumed optimized structures were only subject to infinitesimally small displacements. There are some advantages in this linear assumption, including: (1) linear solutions are easy to compute; (2) the computational cost is low; (3) solutions can be superposed.

However, this linear assumption is not adequate when the following scenarios happen: (1) structures are subject to large deformations; (2) structures are made of nonlinear materials; (3) structure failures occur. Thus, in order to meet such challenges, the current method is necessary to extended to nonlinearity. A nonlinear finite element analysis example is given in Figure 82 (<https://i.ytimg.com/vi/5p4AkvwmtE/hqdefault.jpg>) where the displacements are significant.



Figure 82: An example of non-linear buckling analysis***9.2.3 Non-deterministic Topology Optimization***

While in this thesis topology optimization is utilized in an ‘ideal’ design condition where structural materials are assumed perfectly isotropic and loaded forces are determined, real design conditions can be far more complicated. Due to material processing limitations, material property is not deterministic in the sense that it may deviate from expected performance but satisfy some specific statistics distributions. On another hand, during application process, the loading conditions can be also stochastic. For example, [160] studied the impact of stochastic wind loads on design of windfarm turbines. Topology optimization on structures with non-deterministic properties remains an open research area.

9.2.4 Topology Optimization in Additive Manufacturing

Additive manufacturing (AM) is an evolutionary manufacturing process which builds an object by adding materials layer upon layer. Comparing with traditional subtractive manufacturing, AM has unlimited capacity of fabricating complex geometries and utilizing multiple types of heterogeneous materials.

Topology optimization can be served as an integrated automatous design tool for AM. With the capacity of fabricating infinitely complex geometries, AM can provide topology optimization significant opportunities for wider applications in product design. The marriage between topology optimization and AM provides end-users an opportunity to design and manufacture customer-oriented final products in a ‘top-down’ approach.

Research potentials for the application of topology optimization in AM are significant. In [161], topology optimization is used to minimize support structures while maximizing structural

mechanical properties. Figure 83⁸ is an example showing the ‘top-down’ design-manufacture process provided by topology optimization and AM.



Figure 83: An example of 3D printed structures designed by topology optimization

⁸ The figure is downloaded from <http://www.materialise.com>.

REFERENCE

- [1] J. Deaton and R. V. Grandhi, “Stiffening of Thermally Restrained Structures via Thermoelastic Topology Optimization,” presented at the 53rd AIAA/ ASME/ ASCE/ AHS/ ASC Structures, Structural Dynamics and Materials Conference, Honolulu, Hawaii, 2012.
- [2] G. I. N. Rozvany and N. Olhoff, “On the Solid Plate Paradox in Structural Optimization,” *J. Struct. Mech.*, vol. 10, no. 1, pp. 1–32, 1982.
- [3] M. P. Bendsøe, “Optimal shape design as a material distribution problem,” *Struct. Optim.*, vol. 1, no. 193–202, 1989.
- [4] M. Bendsøe and O. Sigmund, *Topology Optimization: Theory, Methods and Application*, 2nd ed. Springer, 2003.
- [5] M. Zhou, “Difficulties in truss topology optimization with stress and local buckling constraints,” *Structural Optimization*, vol. 11, no. 2, pp. 134–136, 1996.
- [6] S. Nishiwaki, “Topology Optimization of Compliant Mechanisms using the Homogenization Method,” *Int. J. Numer. Methods Eng.*, vol. 42, pp. 535–559, 1998.
- [7] O. Sigmund, “A 99 line topology optimization code written in Matlab,” *Struct. Multidiscip. Optim.*, vol. 21, no. 2, pp. 120–127, 2001.
- [8] D. J. Munk, G. A. Vio, and G. P. Steven, “Topology and shape optimization methods using evolutionary algorithms: a review,” *Struct. Multidiscip. Optim.*, pp. 1–19, May 2015.
- [9] Y. L. Mei, “A level set method for structural topology optimization and its applications,” *Adv. Eng. Softw.*, vol. 35, no. 7, pp. 415–441, 2004.
- [10] Q. Xia, T. Shi, S. Liu, and M. Y. Wang, “A level set solution to the stress-based structural shape and topology optimization,” *Comput. Struct.*, vol. 90–91, pp. 55–64, 2012.
- [11] X. Huang and Y. M. Xie, “A new look at ESO and BESO optimization methods,” *Struct. Multidiscip. Optim.*, vol. 35, no. 1, pp. 89–92, 2008.
- [12] S. Osher and J. A. Sethian, “Fronts Propagating with Curvature-dependent Speed: Algorithms Based on Hamilton-Jacobi Formulations,” *J Comput Phys*, vol. 79, no. 1, pp. 12–49, Nov. 1988.
- [13] S. Osher, “Level-set methods for optimization problems involving geometry and constraints: frequencies of a twodensity inhomogeneous drum,” *J. Comput. Phys.*, vol. 171, pp. 272–288, 2001.
- [14] N. P. van Dijk, K. Maute, M. Langelaar, and F. van Keulen, “Level-set methods for structural topology optimization: a review,” *Struct. Multidiscip. Optim.*, vol. 48, no. 3, pp. 437–472, 2013.
- [15] X. Guo, W. S. Zhang, Y. U. Wang, and P. Wei, “Stress-related topology optimization via level set approach,” *Comput Methods Appl Mech Eng*, vol. 200, pp. 3439–3452, 2011.
- [16] P. Duysinx, L. V. Miegroet, E. Lemaire, O. Brûls, and M. Bruyneel, “Topology and generalized shape optimization: Why stress constraints are so important?,” *Int J Simul Multidisci Optim*, vol. 2, pp. 253–258, 2008.
- [17] G. Rozvany, “Stress ratio and compliance based methods in topology optimization—a critical review,” *Struct. Multidiscip. Optim.*, vol. 21, no. 109–119, 2001.
- [18] H. Rodrigues and H. Fernandes, “A material based model for topology optimization of thermoelastic structures,” *Int. J. Numer. Methods Eng.*, vol. 38, pp. 1951–65, 1995.
- [19] D. Li and X. Zhang, “Topology Optimization of Thermo-Mechanical Continuum Structure,” presented at the 2010 IEEE/ASME International Conference on Advanced Intelligent Mechatronics, Canada, 2010.
- [20] X. Yang and Y. Li, “Topology optimization to minimize the dynamic compliance of a bi-material plate in a thermal environment,” *Struct. Multidiscip. Optim.*, vol. 47, no. 3, pp. 399–408, Aug. 2012.
- [21] X. Yang and Y. Li, “Structural topology optimization on dynamic compliance at resonance frequency in thermal environments,” *Struct. Multidiscip. Optim.*, vol. 49, no. 1, pp. 81–91, Jul. 2013.
- [22] A. H. Taheri, B. Hassani, and N. Z. Moghaddam, “Thermo-elastic optimization of material distribution of functionally graded structures by an isogeometrical approach,” *Int. J. Solids Struct.*, vol. 51, no. 2, pp. 416–429, Jan. 2014.
- [23] X. Liu, C. Wang, and Y. Zhou, “Topology optimization of thermoelastic structures using the guide-weight method,” *Sci. China Technol. Sci.*, vol. 57, no. 5, pp. 968–979, May 2014.
- [24] W. Zhang, J. Yang, Y. Xu, and T. Gao, “Topology optimization of thermoelastic structures: mean compliance minimization or elastic strain energy minimization,” *Struct. Multidiscip. Optim.*, vol. 49, no. 3, pp. 417–429, Sep. 2013.

- [25] M. Stolpe and K. Svanberg, "An alternative interpolation scheme for minimum compliance topology optimization," *Struct. Multidiscip. Optim.*, vol. 22, pp. 116–124, 2001.
- [26] T. Gao and W. Zhang, "Topology optimization involving thermo-elastic stress loads," *Struct. Multidiscip. Optim.*, vol. 42, pp. 725–738, 2010.
- [27] J. Deaton and R. V. Grandhi, "Topology Optimization of Thermal Structures with Stress Constraints," presented at the 54th AIAA/ASME/ASCE/ASC Structures, Structural Dynamics, and Materials Conference, Boston, MA, 2013.
- [28] Q. Li, G. P. Steven, Y. M. Xie, and O. M. Querin, "Evolutionary topology optimization for temperature reduction of heat conducting fields," *Int. J. Heat Mass Transf.*, vol. 47, no. 23, pp. 5071–5083, Nov. 2004.
- [29] Q. Xia and M. Y. Wang, "Topology Optimization of Thermoelastic Structures Using Level Set Method," presented at the EngOpt 2008 - International Conference on Engineering Optimization, Rio de Janeiro, Brazil, 2008.
- [30] N. Vermaak, G. Michailidis, G. Parry, R. Estevez, G. Allaire, and Y. Bréchet, "Material interface effects on the topology optimization of multi-phase structures using a level set method," *Struct. Multidiscip. Optim.*, pp. 1–22, Jun. 2014.
- [31] S. Deng, K. Suresh, and J. Joo, "Stress-Constrained Thermo-Elastic Topology Optimization: A Topological Sensitivity Approach," presented at the Proceedings of the ASME IDETC/CIE Conference, Buffalo, NY, USA, 2014.
- [32] E. Andreassen, A. Clausen, M. Schevenels, and O. Sigmund, "Efficient Topology Optimization in MATLAB Using 88 Lines of Code," *Struct. Multidiscip. Optim.*, vol. 43, pp. 1–16, 2011.
- [33] D. Lee, S. Shin, and S. Park, "Computational Morphogenesis Based Structural Design by Using Material Topology Optimization," *Mech. Based Des. Struct. Mach.*, vol. 35, pp. 39–58, 2008.
- [34] G. Chiandussi, I. Gaviglio, and I. Ibba, "Topology optimisation of an automotive component without final volume constraint specification," *Adv. Eng. Softw.*, vol. 35, pp. 609–617, 2004.
- [35] A. Ramani, "A pseudo-sensitivity based discrete variable approach to structural topology optimization with multiple materials," *Struct. Multidiscip. Optim.*, vol. 41, pp. 913–934, 2009.
- [36] A. Makrodimopoulos, A. Bhaskar, and A. J. Keane, "A compliance based design problem of structures under multiple load cases," *Struct. Multidiscip. Optim.*, vol. 42, pp. 739–742, 2010.
- [37] P. Motammarri, A. Ramani, and A. Kaushik, "Structural topology synthesis with dynamics and nonlinearities using equivalent linear systems," *Struct. Multidiscip. Optim.*, vol. 45, no. 4, pp. 545–558, 2012.
- [38] A. Ramani, "Multi-material topology optimization with strength constraints," *Struct. Multidiscip. Optim.*, vol. 43, pp. 597–615, 2011.
- [39] G. K. Ananthasuresh, S. Kota, and Y. Gianchandani, "A methodical approach to the design of compliant micromechanisms," in *Solid State Sensor and Actuator Workshop*, 1994, pp. 189–192.
- [40] N. Padhye, "Topology Optimization of Compliant Mechanism using Multi-Objective Particle Swarm Optimization," in *GECCO'08, July 12–16*, Atlanta, Georgia, USA., 2008.
- [41] R. Ansola, E. Vegueria, A. Maturana, and J. Canales, "3D compliant mechanisms synthesis by a finite element addition procedure," *Finite Elem. Anal. Des.*, vol. 46, pp. 760–769, 2010.
- [42] J. Lin, "A new multi-objective programming scheme for topology optimization of compliant mechanisms," *Struct. Multidiscip. Optim.*, vol. 30, pp. 241–255, 2010.
- [43] A. Saxena and G. K. Ananthasuresh, "On an optimal property of compliant topologies," *Struct. Multidiscip. Optim.*, vol. 19, pp. 36–49, 2000.
- [44] C. B. W. Pedersen, T. Buhl, and O. Sigmund, "Topology synthesis of large displacement compliant mechanisms," *Int J Numer Meth Engng*, vol. 50, pp. 2683–2705, 2001.
- [45] K. Suresh, A. Ramani, and A. Kaushik, "An Adaptive Weighting Strategy for Multi-Load Topology Optimization," in *ASME 2012 International Design Engineering Technical Conferences & Computers and Information in Engineering Conference*, Chicago, 2012.
- [46] K. Svanberg, "The method of moving asymptotes—a new method for structural optimization," *Int. J. Numer. Methods Eng.*, vol. 24, no. 2, pp. 359–373, Feb. 1987.
- [47] J. Sokolowski, "Optimality Conditions for Simultaneous Topology and Shape Optimization," *SIAM J. Control Optim.*, vol. 42, no. 4, pp. 1198–1221, 2003.
- [48] J. S. Arora, *Introduction to optimum design*. New York: Academic Press, 2004.
- [49] J. Nocedal and S. Wright, *Numerical Optimization*. Springer, 1999.
- [50] M. Kočvara, "Topology optimization with displacement constraints: a bilevel programming approach," *Struct. Optim.*, vol. 14, no. 4, pp. 256–263, Dec. 1997.

- [51] K. Mela, "Resolving issues with member buckling in truss topology optimization using a mixed variable approach," *Struct. Multidiscip. Optim.*, vol. 50, no. 6, pp. 1037–1049, Jul. 2014.
- [52] C. Ni, J. Yan, G. Cheng, and X. Guo, "Integrated size and topology optimization of skeletal structures with exact frequency constraints," *Struct. Multidiscip. Optim.*, vol. 50, no. 1, pp. 113–128, Jan. 2014.
- [53] M. P. Bendsøe, "Optimal shape design as a material distribution problem," *Struct. Optim.*, vol. 1, no. 193–202, 1989.
- [54] R. J. Yang and C. J. Chen, "Stress-Based Topology Optimization," *Struct. Optim.*, vol. 12, pp. 98–105, 1996.
- [55] G. I. N. Rozvany, "A critical review of established methods of structural topology optimization," *Struct. Multidiscip. Optim.*, vol. 37, no. 3, pp. 217–237, 2009.
- [56] V. K. Yalamanchili and A. V. Kumar, "Topology Optimization of Structures using a Global Stress Measure," in *Proceedings of the ASME 2012 International Design Engineering Technical Conferences & Computers and Information in Engineering Conference*, Chicago, IL, 2012.
- [57] M. Werme, "Using the sequential linear integer programming method as a post-processor for stress-constrained topology optimization problems," *Int. J. Numer. Methods Eng.*, vol. 76, no. 10, pp. 1544–1567, Dec. 2008.
- [58] M. Bruggi and P. Venini, "A mixed FEM approach to stress-constrained topology optimization," *Int. J. Numer. Methods Eng.*, vol. 73, no. 12, pp. 1693–1714, Mar. 2008.
- [59] M. Bruggi and P. Duysinx, "Topology optimization for minimum weight with compliance and stress constraints," *Struct. Multidiscip. Optim.*, vol. 46, pp. 369–384, 2012.
- [60] J. T. Pereira, E. A. Fancello, and C. S. Barcellos, "Topology optimization of continuum structures with material failure constraints," *Struct. Multidiscip. Optim.*, vol. 26, no. 1–2, pp. 50–66, Sep. 2003.
- [61] A. R. Gersborg and C. S. Andreasen, "An explicit parameterization for casting constraints in gradient driven topology optimization," *Struct. Multidiscip. Optim.*, vol. 44, no. 6, pp. 875–881, Mar. 2011.
- [62] K.-T. Zuo, "Manufacturing- and machining-based topology optimization," *Int. J. Adv. Manuf. Technol.*, vol. 27, no. 5–6, pp. 531–536, 2006.
- [63] N. Strömberg, "Topology optimization of structures with manufacturing and unilateral contact constraints by minimizing an adjustable compliance–volume product," *Struct. Multidiscip. Optim.*, vol. 42, no. 3, pp. 341–350, 2010.
- [64] J. H. Rong and J. H. Yi, "A structural topological optimization method for multi-displacement constraints and any initial topology configuration," *Acta Mech. Sin.*, vol. 26, no. 5, pp. 735–744, Aug. 2010.
- [65] E. Holmberg, B. Torstenfelt, and A. Klarbring, "Fatigue constrained topology optimization," *Struct. Multidiscip. Optim.*, vol. 50, no. 2, pp. 207–219, Feb. 2014.
- [66] P. G. Coelho and H. C. Rodrigues, "Hierarchical topology optimization addressing material design constraints and application to sandwich-type structures," *Struct. Multidiscip. Optim.*, vol. 52, no. 1, pp. 91–104, Jan. 2015.
- [67] J. Li, S. Chen, and H. Huang, "Topology optimization of continuum structure with dynamic constraints using mode identification," *J. Mech. Sci. Technol.*, vol. 29, no. 4, pp. 1407–1412, Apr. 2015.
- [68] C. Le, "Developments in topology and shape optimization," PhD thesis, University of Illinois at Urbana-Champaign, Urbana-Champaign, 2010.
- [69] H. Guan, Y.-J. Chen, Y.-C. Loo, Y.-M. Xie, and G. P. Steven, "Bridge topology optimisation with stress, displacement and frequency constraints," *Comput. Struct.*, vol. 81, no. 3, pp. 131–145, Feb. 2003.
- [70] W. Li, Q. Li, G. P. Steven, and Y. M. Xie, "An evolutionary shape optimization procedure for contact problems in mechanical designs," *Proc. Inst. Mech. Eng. Part C J. Mech. Eng. Sci.*, vol. 217, no. 4, pp. 435–446, Apr. 2003.
- [71] X. Huang and Y. M. Xie, "Evolutionary topology optimization of continuum structures with an additional displacement constraint," *Struct. Multidiscip. Optim.*, vol. 40, no. 1–6, pp. 409–416, Apr. 2009.
- [72] X. Huang, Z. H. Zuo, and Y. M. Xie, "Evolutionary topological optimization of vibrating continuum structures for natural frequencies," *Comput Struct*, vol. 88, no. 5–6, pp. 357–364, 2010.
- [73] T. Liu, S. Wang, B. Li, and L. Gao, "A level-set-based topology and shape optimization method for continuum structure under geometric constraints," *Struct. Multidiscip. Optim.*, vol. 50, no. 2, pp. 253–273, Mar. 2014.
- [74] K. Suresh and M. Takaloozadeh, "Stress-Constrained Topology Optimization: A Topological Level-Set Approach," *Struct. Multidiscip. Optim.*, vol. 48, no. 2, pp. 295–309, 2013.
- [75] G. Allaire, F. Jouve, and A. M. Toader, "Structural Optimization using Sensitivity Analysis and a Level-set Method," *J. Comput. Phys.*, vol. 194, no. 1, pp. 363–393, 2004.

- [76] S. Deng and K. Suresh, “Multi-constrained topology optimization via the topological sensitivity,” *Struct. Multidiscip. Optim.*, vol. 51, no. 5, pp. 987–1001, 2015.
- [77] M. Y. Wang and L. Li, “Shape equilibrium constraint: a strategy for stress-constrained structural topology optimization,” *Struct. Multidiscip. Optim.*, vol. 47, no. 3, pp. 335–352, Sep. 2012.
- [78] G. Allaire, F. Jouve, and G. Michailidis, “Casting constraints in structural optimization via a level-set method,” in *10th World Congress on Structural and Multidisciplinary Optimization*, Orlando, United States, 2013.
- [79] P. D. Dunning, B. K. Stanford, and H. A. Kim, “Coupled aerostructural topology optimization using a level set method for 3D aircraft wings,” *Struct. Multidiscip. Optim.*, vol. 51, no. 5, pp. 1113–1132, Nov. 2014.
- [80] J. D. Deaton and R. V. Grandhi, “Stress-based design of thermal structures via topology optimization,” *Struct. Multidiscip. Optim.*, pp. 1–18, Oct. 2015.
- [81] M. Zhou and G. I. N. Rozvany, “DCOC: An optimality criteria method for large systems Part I: theory,” *Struct. Optim.*, vol. 5, no. 1–2, pp. 12–25, Mar. 1992.
- [82] R. B. Haber, C. S. Jog, and M. P. Bendsøe, “A new approach to variable-topology shape design using a constraint on perimeter,” *Struct. Optim.*, vol. 11, no. 1–2, pp. 1–12, Feb. 1996.
- [83] J. Petersson and O. Sigmund, “Slope constrained topology optimization,” *Int. J. Numer. Methods Eng.*, vol. 41, no. 8, pp. 1417–1434, Apr. 1998.
- [84] L. Yin and W. Yang, “Optimality criteria method for topology optimization under multiple constraints,” *Comput. Struct.*, vol. 79, no. 20–21, pp. 1839–1850, Aug. 2001.
- [85] G. Allaire, F. Jouve, and A.-M. Toader, “Structural Optimization by the Level-Set Method,” in *Free Boundary Problems*, P. Colli, C. Verdi, and A. Visintin, Eds. Birkhäuser Basel, 2003, pp. 1–15.
- [86] M. Stolpe and T. Stidsen, “A hierarchical method for discrete structural topology design problems with local stress and displacement constraints,” *Int. J. Numer. Methods Eng.*, vol. 69, no. 5, pp. 1060–1084, Jan. 2007.
- [87] J. Paris, F. Navarrina, I. Colominas, and M. Casteleiro, “Topology optimization of continuum structures with local and global stress constraints,” *Struct. Multidiscip. Optim.*, vol. 39, no. 4, pp. 419–437, 2009.
- [88] S. Yamasaki, T. Nomura, A. Kawamoto, K. Sato, K. Izui, and S. Nishiwaki, “A level set based topology optimization method using the discretized signed distance function as the design variables,” *Struct. Multidiscip. Optim.*, vol. 41, no. 5, pp. 685–698, Nov. 2009.
- [89] S. Deng and K. Suresh, “Multi-constrained 3D topology optimization via augmented topological level-set,” *Comput. Struct.*, vol. 170, no. 1, pp. 1–12, 2016.
- [90] H. A. Eschenauer and N. Olhoff, “Topology optimization of continuum structures: A review,” *Appl. Mech. Rev.*, vol. 54, no. 4, pp. 331–389, 2001.
- [91] G. I. N. Rozvany, “A critical review of established methods of structural topology optimization,” *Struct. Multidiscip. Optim.*, vol. 37, no. 3, pp. 217–237, 2009.
- [92] K. Suresh, “A 199-line Matlab code for Pareto-optimal tracing in topology optimization,” *Struct. Multidiscip. Optim.*, vol. 42, no. 5, pp. 665–679, 2010.
- [93] S. Deng and K. Suresh, “Multi-constrained topology optimization via the topological sensitivity,” *Struct. Multidiscip. Optim.*, vol. Accepted, 2014.
- [94] H. A. Eschenauer, V. V. Kobelev, and A. Schumacher, “Bubble method for topology and shape optimization of structures,” *Struct. Optim.*, vol. 8, pp. 42–51, 1994.
- [95] J. Sokolowski and A. Zochowski, “On Topological Derivative in Shape Optimization,” *SIAM J. Control Optim.*, vol. 37, no. 4, pp. 1251–1272, 1999.
- [96] A. A. Novotny, R. A. Feijóo, C. Padra, and E. Taroco, “Topological Derivative for Linear Elastic Plate Bending Problems,” *Control Cybern.*, vol. 34, no. 1, pp. 339–361, 2005.
- [97] A. A. Novotny, “Topological-Shape Sensitivity Method: Theory and Applications,” *Solid Mech. Its Appl.*, vol. 137, pp. 469–478, 2006.
- [98] A. A. Novotny, R. A. Feijoo, and E. Taroco, “Topological Sensitivity Analysis for Three-dimensional Linear Elasticity Problem,” *Comput. Methods Appl. Mech. Eng.*, vol. 196, no. 41–44, pp. 4354–4364, 2007.
- [99] J. Céa, S. Garreau, P. Guillaume, and M. Masmoudi, “The shape and topological optimization connection,” *Comput. Methods Appl. Mech. Eng.*, vol. 188, no. 4, pp. 713–726, 2000.
- [100] A. A. Novotny and J. Sokolowski, *Topological Derivatives in Shape Optimization*. Berlin Heidelberg: Springer, 2012.
- [101] I. Turevsky, S. H. Gopalakrishnan, and K. Suresh, “An Efficient Numerical Method for Computing the Topological Sensitivity of Arbitrary Shaped Features in Plate Bending,” *Int. J. Numer. Methods Eng.*, vol. 79, pp. 1683–1702, 2009.

- [102] I. Turevsky and K. Suresh, “Generalization of Topological Sensitivity and its Application to Defeaturing,” in *ASME IDETC Conference*, Las Vegas, 2007.
- [103] S. H. Gopalakrishnan and K. Suresh, “Feature Sensitivity: A Generalization of Topological Sensitivity,” *Finite Elem. Anal. Des.*, vol. 44, no. 11, pp. 696–704, 2008.
- [104] K. K. Choi and N. H. Kim, *Structural Sensitivity Analysis and Optimization I: Linear Systems*. New York: Springer, 2005.
- [105] D. A. Tortorelli and W. Zixian, “A systematic approach to shape sensitivity analysis,” *Int. J. Solids Struct.*, vol. 30, no. 9, pp. 1181–1212, 1993.
- [106] R. A. Feijoo, A. A. Novotny, E. Taroco, and C. Padra, “The topological-shape sensitivity method in two-dimensional linear elasticity topology design,” in *Applications of Computational Mechanics in Structures and Fluids*, CIMNE, 2005.
- [107] I. Turevsky and K. Suresh, “Tracing the Envelope of the Objective-Space in Multi-Objective Topology Optimization,” presented at the ASME IDETC/CIE Conference, Washington, DC, 2011.
- [108] S. Amstutz and H. Andra, “A new algorithm for topology optimization using a level-set method,” *J. Comput. Phys.*, vol. 216, pp. 573–588, 2006.
- [109] K. Suresh, “A 199-line Matlab code for Pareto-optimal tracing in topology optimization,” *Struct. Multidiscip. Optim.*, vol. 42, no. 5, pp. 665–679, 2010.
- [110] J. A. Norato, M. P. Bendsoe, R. B. Haber, and D. A. Tortorelli, “A topological derivative method for topology optimization,” *Struct. Multidiscip. Optim.*, vol. 33, pp. 375–386, 2007.
- [111] K. Suresh, “Efficient Generation of Large-Scale Pareto-Optimal Topologies,” *Struct. Multidiscip. Optim.*, vol. 47, no. 1, pp. 49–61, 2013.
- [112] R. B. Hetnarski, J. Ignaczak, N. Noda, N. Sumi, and Y. Tanigawa, *Theory of Elasticity and Thermal Stresses: Explanations, Problems and Solutions*. Springer, 2013.
- [113] C. Le, J. A. Norato, T. E. Bruns, C. Ha, and D. A. Tortorelli, “Stress-based topology optimization for continua,” *Struct. Multidiscip. Optim.*, vol. 41, no. 4, pp. 605–620, 2010.
- [114] K. Suresh, “Hinge-Free Compliant Mechanism Design via the Topological Level-Set,” in *Proceedings of the ASME 2013 International Design Engineering Technical Conferences & Computers and Information in Engineering Conference*, Portland, OR, 2013, vol. Submitted.
- [115] K. Suresh, “Multi-Objective Topology Optimization on the GPU,” in *ASME IDETC/CIE Conference, 2011*, Washington, DC, 2011.
- [116] W. Long, X. Liang, Y. Huang, and Y. Chen, “A hybrid differential evolution augmented Lagrangian method for constrained numerical and engineering optimization,” *Comput.-Aided Des.*, vol. 45, pp. 1562–1574, 2013.
- [117] K. Suresh, “Efficient Generation of Large-Scale Pareto-Optimal Topologies,” *Struct. Multidiscip. Optim.*, vol. 47, no. 1, pp. 49–61, 2013.
- [118] Ng, “A computational paradigm for multiresolution topology optimization (MTOP).”
- [119] S. Schmidt, “A 2589 Line Topology Optimization Code Written for the Graphics Card,” Univeritat Trier; www.am.uni-erlangen.de, Technical report Preprint SPP1253-068, 2009.
- [120] R. J. Yang and C. J. Chen, “Stress-Based Topology Optimization,” *Struct. Optim.*, vol. 12, pp. 98–105, 1996.
- [121] Vrand, *Genesis*; <http://vrand.com/Genesis.html>. 2011.
- [122] P. Duysinx, L. V. Miegroet, E. Lemaire, O. Bruls, and M. Bruyneel, “Topology and generalized shape optimization: Why stress constraints are so important?,” *Int J Simul Multidisci Optim*, vol. 2, pp. 253–258, 2008.
- [123] X. Guo and G. D. Cheng, “Epsilon-continuation approach for truss topology optimization,” *Acta Mech. Sin.*, vol. 20, no. 5, pp. 526–533, 2004.
- [124] C. Le, “Developments in topology and shape optimization,” PhD thesis, University of Illinois at Urbana-Champaign, Urbana-Champaign, 2010.
- [125] J. Paris, F. Navarrina, I. Colominas, and M. Casteleiro, “Topology optimization of continuum structures with local and global stress constraints,” *Struct. Multidiscip. Optim.*, vol. 39, no. 4, pp. 419–437, 2009.
- [126] R. T. Marler, “Survey of multi-objective optimization methods for engineering,” *Struct. Multidiscip. Optim.*, vol. 26, pp. 369–395, 2004.
- [127] R. T. Marler, “The weighted sum method for multi-objective optimization: new insights,” *Struct. Multidiscip. Optim.*, vol. 41, no. 6, pp. 853–862, 2010.
- [128] A. Messac, “Ability of Objective Functions to Generate Points on Non-Convex Pareto Frontiers,” *AIAA J.*, vol. 38, no. 6, pp. 1084–1091, 2000.

- [129] P. Motamarri, A. Ramani, and A. Kaushik, "Structural topology synthesis with dynamics and nonlinearities using equivalent linear systems," *Struct. Multidiscip. Optim.*, DOI: . /s00158-011-0713-0 1007.
- [130] S. <http://www.simulia.com/products/atom.html>, *ATOM*.
- [131] P. Yadav and K. Suresh, "Large Scale Finite Element Analysis Via Assembly-Free Deflated Conjugate Gradient," *J Comput Inf Sci Eng*, vol. 14, no. 4, pp. 41008-1-9, 2014.
- [132] J. Hennessy and D. Patterson, *Computer Architecture, A Quantitative Approach*, 5th ed. Elsevier, 2011.
- [133] K. Suresh and P. Yadav, "Large-Scale Modal Analysis on Multi-Core Architectures," in *Proceedings of the ASME 2012 International Design Engineering Technical Conferences & Computers and Information in Engineering Conference*, Chicago, IL, 2012.
- [134] X. Bian, P. Yadav, and K. Suresh, "Assembly-Free Buckling Analysis for Topology Optimization," presented at the ASME-IDETC Conference, Boston, MA, 2015.
- [135] Y. Jiang, H. Kautz, and B. Selman, "Solving problems with hard and soft constraints using a stochastic algorithm for MAX-SAT," in *Proceedings of the 1st International Workshop on Artificial Intelligence and Operations Research*, Timberline, Oregon, 1995.
- [136] M. F. Ashby, "Multi-objective optimization in material design and selection," *Acta Mater.*, vol. 48, no. 1, pp. 359–369, 2000.
- [137] M. Zhou and et. al., "Progress in Topology Optimization with Manufacturing Constraints," in *9th AIAA/ISSMO Symposium on Multidisciplinary Analysis and Optimization*, Georgia, Atlanta, 2002.
- [138] P. Duysinx and O. Sigmund, "New developments in handling stress constraints in optimal material distribution," in *7th AIAA/USAF/NASA/ISSMO Symposium on Multidisciplinary Analysis and Optimization*, American Institute of Aeronautics and Astronautics, 2015.
- [139] L. A. Peterson and K. J. Londry, "Finite-Element Structural Analysis: A New Tool for Bicycle Frame Design. The Strain Energy Design Method," *Bike Tech, Bicycling Magazine's Newsletter for the Technical Enthusiast*, vol. 5, no. 2, 1986.
- [140] R. R. Bini and et. al., "Pedal force effectiveness in Cycling: a review of constraints and training effects," *J. Sci. Cycl.*, vol. 2, no. 1, 2013.
- [141] M. Bruyneel and P. Duysinx, "Note on topology optimization of continuum structures including self-weight," *Struct. Multidiscip. Optim.*, vol. 29, no. 4, pp. 245–256, Nov. 2004.
- [142] R. D. Cook, D. S. Malkus, M. E. Plesha, and R. Witt, *Concepts and Applications of Finite Element Analysis*, 4th ed. John Wiley & Sons, 2002.
- [143] W. Aichtziger, "Local stability of trusses in the context of topology optimization part I: exact modelling," *Structural Optimization*, vol. 17, no. 4, pp. 235–246, 1999.
- [144] X. Guo, G. Cheng, and K. Yamazaki, "A new approach for the solution of singular optima in truss topology optimization with stress and local buckling constraints," *Structural Optimization*, vol. 22, no. 5, pp. 364–373, 2001.
- [145] K. Mela, "Resolving issues with member buckling in truss topology optimization using a mixed variable approach," *Struct Multidisc Optim*, vol. 50, no. 6, pp. 1037–1049, 2014.
- [146] M. M. Neves, H. Rodrigues, and J. M. Guedes, "Generalized topology design of structures with a buckling load criterion," *Struct. Optim.*, vol. 10, no. 2, pp. 71–78, Oct. 1995.
- [147] M. Bendsoe and O. Sigmund, *Topology Optimization: Theory, Methods and Application*, 2nd ed. Springer, 2003.
- [148] M. Zhou, "Topology optimization for shell structures with linear buckling responses," presented at the WCCM VI, Beijing, China, 2004.
- [149] E. Lindgaard and J. Dahl, "On compliance and buckling objective functions in topology optimization of snap-through problems," *Struct Multidisc Optim*, vol. 47, no. 3, pp. 409–421, 2013.
- [150] X. Gao and H. Ma, "Topology optimization of continuum structures under buckling constraints," *Computers & Structures*, vol. 157, pp. 142–152, 2015.
- [151] J. H. Rong, Y. M. Xie, and X. Y. Yang, "An improved method for evolutionary structural optimisation against buckling," vol. 79, no. 3, pp. 253–263, 2001.
- [152] S. J. van den Boom, "Topology Optimisation Including Buckling Analysis," Delft University of Technology, Delft, 2014.
- [153] A. M. Mirzendehtdel and K. Suresh, "A Pareto-Optimal Approach to Multimaterial Topology Optimization," *J. Mech. Des.*, vol. 137, no. 10, 2015.
- [154] R. Sedaghati, and M. S. A. Elsayed, "Wing Rib Stress Analysis and Design Optimization." Concordia University, Jun-2006.

- [155] R. Quinn and R. Fields, *Comparison of measured and calculated temperatures for a Mach 8 hypersonic wing test structure*. Ames Research Center, Dryden Flight Research Facility: National Aeronautics and Space Administration, 1986.
- [156] R. A. Lusk, "Space Shuttle Structural Design Concepts and Fabrication Problems." Society of Automotive Engineers, 1970.
- [157] R. D. Cook, D. S. Malkus, M. E. Plesha, and R. Witt, *Concepts and Applications of Finite Element Analysis*, 4th ed. John Wiley & Sons, 2002.
- [158] J. B. Choi and R. S. Lakes, "Design of a fastener based on negative Poisson's ratio foam," *Cell. Polym.*, vol. 10, pp. 205–212, 1991.
- [159] K. Suresh, "Efficient Microstructural Design for Additive Manufacturing," in *Proceedings of the ASME 2014 International Design Engineering Technical Conferences & Computers and Information in Engineering Conference*, Buffalo, NY, USA, 2014, vol. Submitted.
- [160] J. Chun, J. Song, and G. Paulino, "Topology optimization of structures under constraints on first passage probability," in *12th International Conference on Application of Statistics and Probability in Civil Engineering*, Vancouver, Canada, 2015.
- [161] J. Vanek, J. A. G. Galicia, and B. Benes, "Clever Support: Efficient Support Structure Generation for Digital Fabrication," *Comput. Graph. Forum*, vol. 33, no. 5, pp. 117–125, Aug. 2014.